MICROCOPY RESOLUTION TEST CHART

NATIONAL BUREAU OF STANDARDS-1963-A

④

PIEZOELECTRIC AND ELECTROSTRICTIVE MATERIALS FOR TRANSDUCER APPLICATIONS

Period January 1 to December 31, 1987

DTIC FILE COPY

Annual Report

OFFICE OF NAVAL RESEARCH

Contract No. N00014-82-K0339

APPROVED FOR PUBLIC RELEASE--DISTRIBUTION UNLIMITED

L.E. Cross
R.E. Newnham
G.R. Barsch
J.V. Biggers

March 1988

Volume II

DTIC
ELECTE
S
MAY 0 9 1988
D
E

THE MATERIALS RESEARCH LABORATORY

THE PENNSYLVANIA STATE UNIVERSITY

UNIVERSITY PARK, PENNSYLVANIA

88 5 9 050

PREPRINTS OF SUBMITTED PAPERS

Electrostrictive Studies

LASER INTERFEROMETER FOR THE STUDY OF PIEZOELECTRIC AND ELECTROSTRICTIVE STRAINS

Q.M. Zhang, W.Y. Pan, and L.E. Cross

Materials Research Laboratory

The Pennsylvania State University

University Park, PA 16802

ABSTRACT

A modified Michelson interferometer is used to study the strain properties of piezoelectric and electrostrictive materials. For small displacement, a feedback loop is introduced to stabilize the system against the low frequency optical path-length drifting and the system is capable of resolving displacements of the order of 10^{-3} Å. For the strain induced by domain switching a dual-channel signal detection scheme is used which automatically reads out the displacement of the sample. The effect on the measurement of the sample bonding to a substrate and other related problems are discussed.

I.   INTRODUCTION

The study of the piezoelectric and electrostrictive properties of ferroelectric and other materials involves the detection of the strain induced by the external driving forces. The displacement related to this kind strain varies from the order of 10 Å to more than 1 μm. Various methods have been used to measure these strains precisely. Among them, optical methods show great promise because they do not require calibration in the length scale, do not have mechanical contact and also can be used to probe the displacement profile of the sample surface at various locations and under different conditions.[1-5] The basic principle of the laser interferometer is that, for a monochromatic light of wave length λ interfering with a reference beam the interference light intensity at a detection point is

$$I = I_p + I_r + 2 I_p I_r \cos(4\pi\Delta d/\lambda) \qquad (1)$$

where I_p and I_r are the light intensity for the probing beam, where the sample is placed, and the reference beam respectively, Δd is the optical path-length difference between the two beams. A relative change Δd between the two beams results in a change in the interference light intensity which can be detected by different methods depending on the magnitude of the displacement change Δd. For the convenience, eq. (1) can be rewritten as:

$$I = 1/2(I_{max} + I_{min}) + 1/2(I_{max} - I_{min}) \cos(4\pi\Delta d/\lambda) \qquad (2)$$

where I_{max} and I_{min} are the maximum and minimum interference light intensities, which can be measured from the interference intensity curve conveniently.

The interferometer   which is discussed below makes use of two different signal detection schemes. In measuring displacement smaller than 300 Å, a dc feedback loop is used to

stabilized the system against thermal and mechanical optical path-length fluctuation and it is able to resolve very small displacement of the order 10^{-3} Å by using an ac signal detection method. For the large displacement measurement, a dual channel signal detection scheme is used which is able to automatically and precisely determine the turning point of the motion of the detected surface and trace out the displacement. The error associated with the measurement of the displacement of several μm is on the order of 10 Å, which is a negligibly small of the total displacement measured.

II.   DETECTION OF SMALL DISPLACEMENT

The schematic drawing of the interferometer as well as the electronic system for detecting small displacements is shown in Fig. 1. In this simple Michelson interferometer, the incident laser beam (λ = 6328 Å) is split into half-power beams by a cube beamsplitter. After bouncing back from the sample surface and the reference mirror, the probing beam and the reference beam are recombined by the same beamsplitter and form an interference pattern at the detection point which is described by eq. (1). In the real experiment situation, due to the finite size of the laser beam, if the optical path-length difference Δd is not small enough, the interference pattern will show a distribution in the light intensity at the detection plane such as that shown in Fig. 2. If the photo-detector aperture is larger than the central fringe diameter, the sensitivity of the system can be greatly reduced. Since this central fringe diameter is inversely proportional to Δd, effort has been made in the system set-up process to reduced this Δd so that in the detection screen, the view spot shows uniform light intensity distribution, indicating that the central fringe diameter is much larger than the aperture of the photo-detector. In order to further improve the sensitivity, a condenser lens is inserted in front of the photo-detector to further expand the diameter of the central fringe. Under these conditions, the light intensity seen by the detector is that described by eq. (1).

For small displacement measurement, it is desirable to set the interference between the two beams at a point about $(2n + 1)\lambda/8$ ($\pi/2$ point) where the light intensity change will be maximized for the same displacement change in Δd. Near this point, we can write Δd as

$$\Delta d = d_{ac} + (2n + 1)\lambda/8 \qquad (3)$$

and eq. (1) can be reduced to

$$I = I_p + I_r \pm 2 I_p I_r \, \text{Sin} \, 4\pi d_{ac}/\lambda = I_p + I_r \pm 2 I_p I_r \, 4\pi \, d_{ac}/\lambda \qquad (4)$$

In eq. (4), the sign of "+" or "-" depends on whether n is an even or odd number. The approximation of $\text{Sin} x = x$ is valid for small x and in our case, the error associated is less than 1% if $/d_{ac}/$ is less than 130 Å. Eq. (4) indicates that the light intensity change is linearly proportional to the change d for small displacement. This makes it possible to use ac method to determine the strain response of the sample to the external driving force.

The stabilization of the interferometer at the $\pi/2$ point is achieved by introducing a feedback loop in the reference arm as shown in Fig. 1. As a matter of fact, the configuration used here can set the system at any reference point by adjusting the voltage level at the differential amplifier reference input. This feedback loop respondes only to low frequency signals (< 10 HZ). It does not affect the measurement at higher frequencies. In the same manner, it will not reduce the high frequency noise, instead, this extra loop may add more noise at high frequency. However, due to the fact that the system can stay at the $\pi/2$ point for any length of time, d_{ac} can be determined by a lock-in amplifier which has high noise rejection ability and the signal can be averaged over any time length desired. This is the key to improve the sensitivity of the system for the detection of small displacements.

For a sinusoidal displacement, $d_{ac} = d_0 \cos \omega t$, the optical signal is converted by the photo-diode to a voltage change and then pre-amplified. This signal is detected by an Ithaco lock-in

amplifier (model 393) as V_{out} which is a rms value of the detected signal corresponding to the displacement $d_0/\sqrt{2}$. From eq. (4), it can be shown that

$$d_0 = (\lambda/\sqrt{2}\,\pi)\,(V_{out}/V_{p-p}) \tag{5}$$

Where V_{p-p} is the peak to peak value of the interference signal, which corresponds to the change in the interference signal $(I_{max} - I_{min})$.

III. PIEZOELECTRIC AND ELECTROSTRICTIVE MEASUREMENT

Piezoelectric and electrostrictive coefficients were measured for X-cut quartz, hard PZT, soft PZT, and PMN samples. In these measurements, the sample was polished on one face to optical quality in order to perfectly reflect the incident laser beam. Since it was difficult to polish the surfaces of some ceramic samples to optical flatness, two alternative methods were used. First, silver paint was put on the sample surface and dried at 600°. The silver paint film was polished to a mirror surface which also serves as the electrode. In the second method, a small mirror was attached to the sample for a reflection surface. However, this latter method is not suitable for the measurements at high frequency. In the experimental process, it was found that the quality of the reflection surface of the sample is very important for accuracy. A poor reflection surface can cause distortion of the interference pattern and introduce severe errors in the determination of small displacements using eq. (5).

Sample bonding is another important factor which can affect the strain measurement of the sample to a great extent. In our measurement, the sample size may vary from the order of mm in linear dimension to 1 cm. The sample was electroded by gold sputtering. The back face of the sample was attached to the optical sample holder using silver epoxy. The sample holder is able to move in X-Y-Z directions and rotate the sample about the vertical and horizontal axes. This is

necessary for proper adjustment of the system. Another sample bonding method was proposed in literature.[2] This method is not suitable for the high frequency measurements and may introduce extra complications into the system. In using the bonding material to attach the sample to the holder, it is obvious that the bonding agent will have a clamping effect on the sample (introducing stress in the sample). It has been shown that for the same driving voltage, the strain in the clamped sample can be reduced to 60% of that measured in unclamped samples.[3] The effects of the bonding are discussed below.

In order to determine the piezoelectric or electrostrictive coefficients of a sample by this interferometer detection scheme, we have assumed that the strain induced by the driving voltage causes only the front face of the sample to move (the surface facing the beam) and the motion of the back face is negligible. This assumption may not be valid if the bonding agent is not rigid enough to hold the sample or if the sample is being driven at a very high frequency. An ideal bonding material should have an infinite elastic constant in the sample motion direction (z direction in Fig. 3) and zero elastic constant in the lateral direction. A simple model can be used to analyze the z direction motion of the sample as shown in Fig. 3. To avoid complications, a self-consistent method is employed to treat the problem. In Fig. 3, the bonding agent acts as a spring with an elastic constant k ($k = cA/l$, where c is the elastic constant of the bonding agent at unit area and length, A the area and l the thickness   ). If we assume that the back-face of the sample is perfectly clamped, the motion of the mass center of the sample will be half of the motion of the front face. For a displacement with a frequency f and an amplitude z_0 of the front face, the force needed to support the sample would be equal to ($2\pi^2 m z_0 f^2$). For a typical sample, m is of the order of 1 gram, and the silver epoxy (ACME 3021) has c (elastic constant) of the order of 10^9 newton/m^2, which is about two order of magnitude smaller than that of the sample.[6] The contact area of the silver epoxy in our experiment is of the order of 1 mm^2 and the thickness is of the order of 0.1 mm. The ratio between the back face motion (due to the deformation of the silver epoxy to produce a force to support the sample) and the front face motion z/z_0, therefore, will be

proportional to $f^2 \times 10^{-9}$. Hence, the error introduced by the back face motion of the sample can be smaller than 1% if the operating frequency of the system is lower than 20 K HZ.

The clamping effect in the lateral direction is negligible due to the fact that the bonding material used is about two orders softer than the sample. Since the σ (Poisson ratio) is in the region $0 < \sigma < 1/2$, the influence of this lateral clamp on the longitudinal motion of the sample is very small as long as the system is far away from a resonance frequency and the sample strain in the lateral direction is small (<0.2%).

The measurements on X-cut quartz, hard PZT and soft PZT support the points discussed above. At frequencies below 2 K HZ, the d_{11} value for quartz is 2.26 x 10^{-12} within 1% error. The frequency scan for the quartz sample is shown in Fig. 4. The same result can be seen for hard PZT which is shown in the same figure. Mechanical resonance occurs at frequencies above 5 K HZ. This kind of resonance was also observed in the measurement by another group.[7] From the model in Fig. 3, the mechanical resonance due to bonding for the system would occur at frequency near or above 50 K HZ. We do not fully understand why this resonance occurs at such a low frequency. It may be due to the thin electrode layer between the silver epoxy and the sample or the sample holding system which has a large mechanical mass. For very high frequency strain measurements, any mechanical method of bonding the sample is obviously inadequate. Further effort will be made to separate the motion for the sample as a whole body and the relative motion (the strain) between the front and back faces of the sample.

In Fig. 4, we also show the voltage scan of the hard PZT sample at a driving frequency of 900 HZ. It can be seen that the strain response of the sample to the external driving voltage is still linear for a field as weak as 5mV/cm which will be discussed in a separate paper. The resolution of our system at this frequency is on the order of 10^{-3} Å. Such kind of resoltion can only be achieved when the experiment is done under a quiet environment and the signal is averaged in the

lock-in over a relatively long time period. It is clear that the resolution of the displacement should be frequency dependent since the noise spectrum is a function of frequency. At very high frequencies, the only limit to the resolution of the system will be that from electronic noise. At frequencies below 100 HZ, any outside mechanical disturbance can make the measurement difficult and the resolution of the system is not better than 5×10^{-3} Å.

Electrostrictive coefficients were also measured for a PMN ceramic sample. The electrostrictive coefficient is defined as

$$S = ME^2 \qquad (6)$$

where E is the field strength. In this measurement, a voltage V is applied across a sample with thickness L, and $E = V/L$. Strain amplitude $S_0 = d_0/L$, where d_0 is the displacement measured by the lock-in amplifier at 2f mode (the driving voltage is used as the reference signal which is at frequency f). For a driving voltage $V = V_0 \cos \omega t$, $V^2 = (V_0^2/2)(1 - \cos 2\omega t)$. Eq. (6) can be written as

$$S = (MV_0^2/2L^2)(1 - \cos 2\omega t) \qquad (7)$$

Using eq. (5) to find d_0,

$$M = 2d_0 L/V_0^2 \qquad (8)$$

For a PMN ceramic sample, M_{11} is measured at a frequency of 250 HZ and is found to be $1.03 \times 10^{-16} m^2/V^2$. The same PMN sample was measured by the strain gauge method.[8] Q_{11} obtained is 1.9×10^{-2}, therefore $M = (\varepsilon \varepsilon_0)^2 \times Q = 1.02 \times 10^{-16} m^2/V^2$ ($\varepsilon = 8300$ is used). This is in good agreement with our value.

IV. DUAL CHANNEL DETECTION AND THE DETERMINATION OF THE STRAIN DUE TO DOMAIN SWITCHING IN FERROELECTRICS

In the measurement of strain induced by domain switching the maximum strain at saturation field may vary from less than 10^{-3} to more than 5×10^{-3}. For the sample used in this measurement the thickness ranges from 0.15 mm to 1 mm. The mechanical displacement, therefore, is on the order of μm or larger which correspond to several wavelength of the laser light ($\lambda = 6328$ Å). It is clear that the ac measurement scheme described above is not suitable here. The determination of the displacement must involve recording the interference pattern with time. However, in these measurements the displacement will have two opposite directions. The reversal of the displacement direction will cause a corresponding reversal of the interference pattern (shown in Fig. 5) which may coincide with the maximum or minimum point of the interference pattern. This makes the data treatment difficult and confusing. A single channel signal detection is not adequate and it is impossible to read out the strain automatically. A dual channel detection scheme which will be described below can overcome this difficulty and our experimental results show that this technique is much more sensitive than conventional techniques such as the linear variable differential transformer (LVDT) and the strain gauge.

A schematical drawing for this part of the set-up is shown in Fig. 6. In order to have dual channel detection, the polarized nature of the laser beam is used. A polarized beam splitter reflects the light with the polarization in the horizontal plane and transmits the light vertically polarized. The polarizations of the probing beam and the reference beam are perpendicular to each other. In both the probing arm and the reference arm, a quarter-wave plate is inserted which rotates the polarization direction in both arms by 90° before the lights come back to the polarized beam splitter. A neutral beam splitter divides the combined beam again into two detection channels. In one of the detection path, a phase plate is used to adjust the phase of the light in one polarization

direction by λ/4 with respect to the other polarization direction. The final interference signals detected by the two detectors, therefore, have a 90° phase difference as shown in Fig. 5(d). It is clear that in an X-Y plot, the combined signal from these two detectors will be a circle and the angular position of the signal represents the displacement due to the strain. The two directions of the rotation of the circle correspond to the forward and backward motions of the detected surface of the sample. The statements above can be summarized as

$$\tan\theta(t) = V_y(t)/V_x(t) \tag{9}$$

and the displacement versus time d(t) is

$$d(t) = (\lambda/4\pi)\,\theta(t) \tag{10}$$

where V_y and V_x are the signals from the two photo-detectors and t is time. A computer program can be made to simultaneously read out the displacement versus time from eqs. (9) and (10). There is no need to determine the inflection point of the displacement. The rotation direction of $\theta(t)$ automatically indicates the displacement directions once it is been calibrated.

The experiment was done on PLZT 8/65/35 ceramic samples supplied by Shanghai Institute of Ceramics (China). These samples were hot-pressed to transparency and the average grain size is 23 µm. The sample preparation is the same as that for the small displacement measurement. In the measurement the fringe signals from the main detection channel and the quadrature channel as a function of time were simultaneously recorded by a digital oscilloscope (Nicolet model 204A). The triangle driving voltage was also recorded. These data are shown in Fig. 7. In the experimental process we used a condenser lens to focus the light on the sample surface as shown in Fig. 6. This lens is essential for a proper measurement. Since the movement of the sample surface is not always strictly perpendicular to the incident beam, this may cause a change in I_p and

also the relative phase of the return beam. This will result in an error in the data reading. In the case that the sample reflection surface is in the focal plane of the condenser lens, the reflected beam is approximately from the focal point of that lens. The deviation of the return beam from the incident beam, after passing the condenser lens, is greatly reduced due to the fact that all the light originated from one point of the focal plane will propagate parallel to the corresponding optical axis of that lens. In our case, it is clear that this optical axis is on the line of the incident laser beam. This insures that I_p is approximately constant during the measurement.

The final strain hysteresis loop for the PLZT sample is plotted in Fig. 8. Initial switching is not observed because the signals were recorded after a few switching cycles. We repeated the experiment at frequencies below 10 HZ for the sample with different bonding conditions, that is, with different contact area and thickness of the silver epoxy. For the case that the silver epoxy totally covers the back face of the sample (maximum clamp in the measurement) and the case that the bonded area is on the order of 1/10 of the total area of the sample, no obvious difference in the strain hysteresis loop and the magnitude of the strain was observed which agrees with the discussion above regarding the clamping effect in our measurements.

Several variables, such as thermal and mechanical drift of the optical path length, may affect the absolute accuracy of the measurement.[3] We believe, in our experiment, that the main error is introduced by the limited resolution of the data recording system, the digital oscilloscope. For time resolution 1 ms under 1 HZ driving field (1/1000 a cycle resolution), the uncertainty of the displacement for PLZT sample is about 30 A. Compared with the total displacement (--1 μm) for the sample, this error is actually negligible.

In order to further improve the bonding condition to reduce possible clamping effect for extra large strain measurement and to eliminate the sample reflection face tilting due to mechanical imbalance of the bonding surface, a vacuum sample holder was designed and used in some of the

experiments. It is shown schematically in Fig. 9, the front face of the holder is polished and an array of small holes with the diameter of 1 mm or less are drilled through the front plate. Several such plates were made with different number of holes for different sample sizes. The back face of the sample is weakly bonded to the holder with a very thin layer of vacuum grease, which serves to keep vacuum in the holder. A mechanical rotary pump is used to produce the vacuum to hold the sample. Therefore, the sample holding force is atmospheric pressure. This arrangement makes the sample under test almost free from clamping and due to the fact that the whole back face of the sample is held tightly against the holder, the possibility of the sample reflecting face tilting is almost eliminated. The experimental results on several PZT family samples show this is indeed the case.

V. ACKNOWLEDGEMENTS

REFERENCES

1.   D. Vilkomerson, Appl. Phys. Lett. 29, 183 (1976).

2.   D.L. Allenswoth, Rev. Sci. Instrum. 51, 1330 (1980).

3.   Th. Kwaaital, Rev. Sci. Instrum. 45, 339 (1974).

4.   V.E. Bottom, J. Appl. Phys. 41, 3941 (1970).

5.   T.R. Gururaja, W.A. Schulze, L.E. Cross, R.E. Newnham, B.A. Auld, and J. Wang, IEEE, 32, 481 (1985).

6.   Physical Properties of Crystal (Oxford, 1967) J.F. Nye.

7.   K. Uchino, S. Nisshida, and S. Nomura, Jap. J. Appl. Phys. 21, 596 (1982).

8.   W.Y. Pan and L.E. Cross, preprint.

FIGURE CAPTIONS

Figure 1. Schematic drawing of the ac interferometer. The lock-in can be operated at either 1f or 2f mode to measure the piezoelectric or electrostrictive coefficients.

Figure 2. Interference pattern in the detection plane for a finite beam size of the laser and a large Δd. I is the light intensity and L is the distance from the center of the spot.

Figure 3. A model system to analyze the motion of the sample in the z direction.

Figure 4. (a) Frequency scan of d_{11} for X-cut quartz. F is the operation frequency.

(b) Frequency scan of d_{33} for hard PZT.

(c) Voltage scan for hard PZT at 900 HZ driving frequency. d_o is the amplitude of the displacement and V is the amplitude of the driving voltage.

Figure 5. (a) The interference light intensity versus the displacement (from eq. (1)). This is the signal detected by the photo-detector.

(b) The change of the displacement direction causes an inflection in the interference signal. Here, the inflection coincides with the maximum point of the interference pattern. The detector can not determine the turning point.

(c) The displacement inflection at position other than I_{max} and I_{min}. The inflection can be seen clearly.
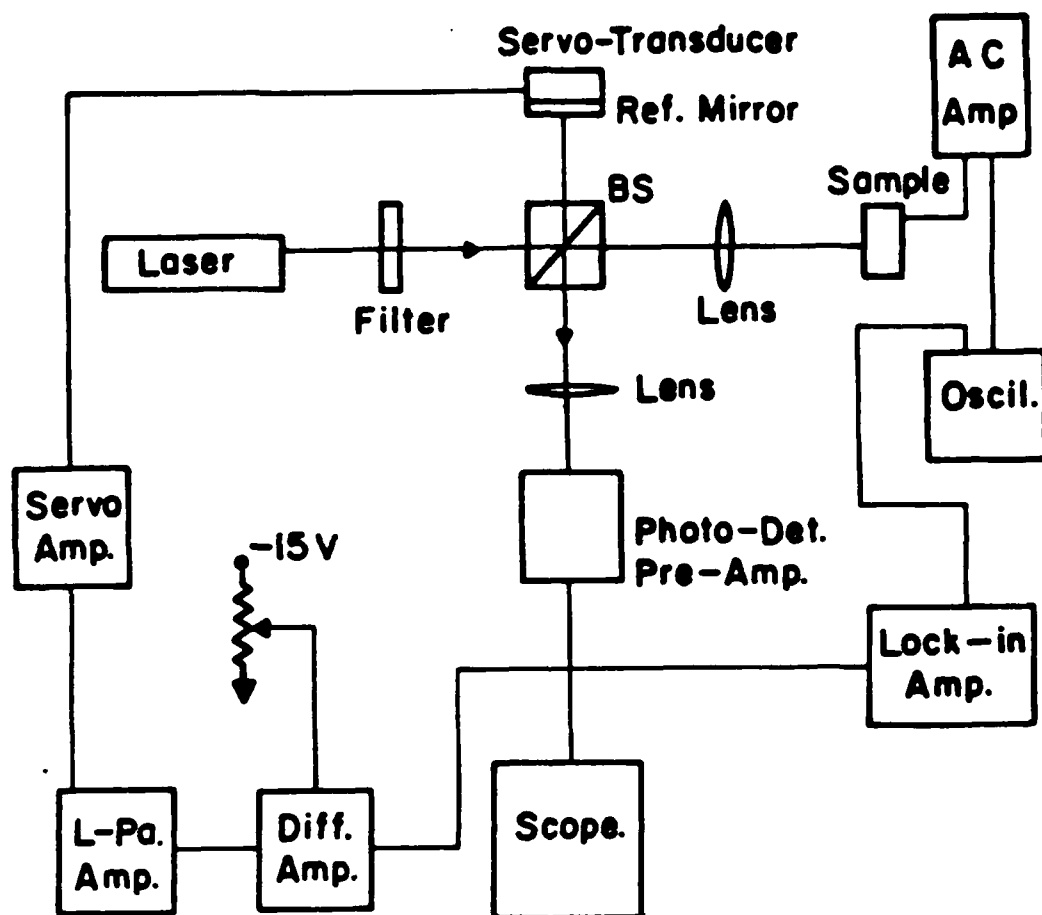
(d) The signals from the main detection channel and the quadrature channel. They are $\lambda/4$ apart.
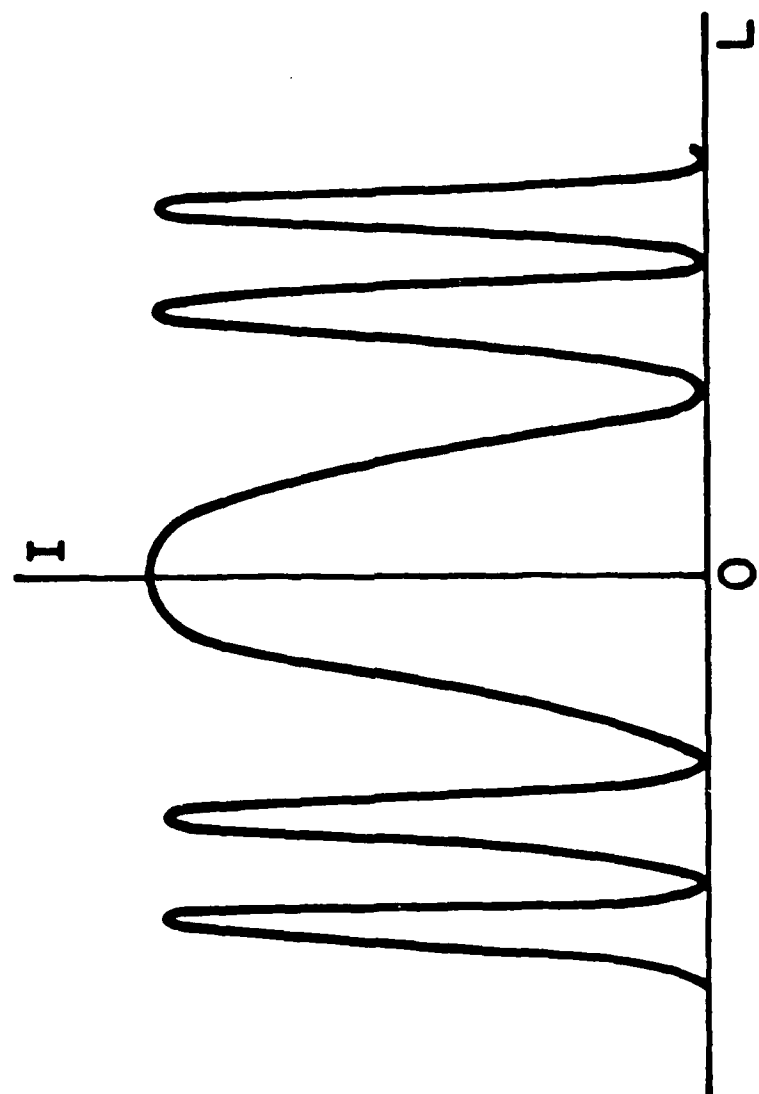
Figure 6.   Schematic drawing of the dual-channel detection interferometer. F is the filter, PS is the phase plate, W.G. is the waveform generator, PBS is the polarized beam splitter, $\lambda/4$ is the quarter-wave plate, P the polarizer.
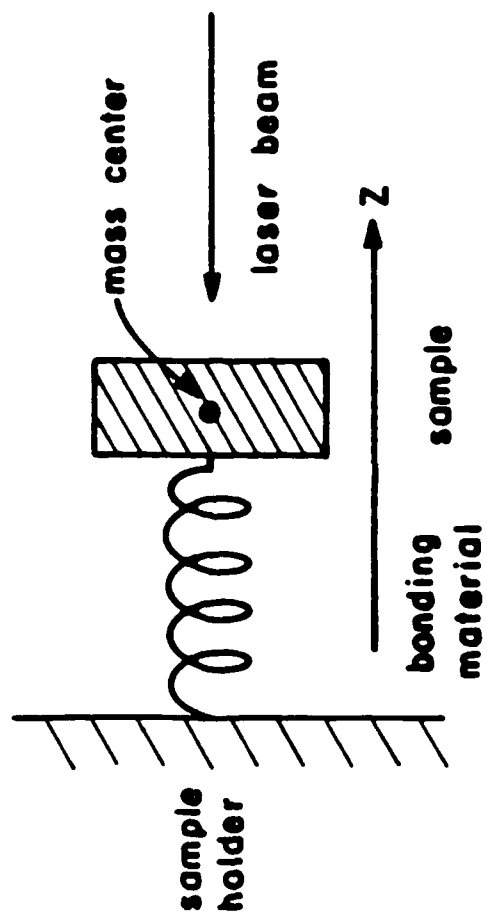
Figure 7.   Recorded signals for PLZT 8/65/35 samples. (a) is the signal from the main channel and (b) is from the quadrature channel. The driving triangle voltage is also recorded and shown as (c). All the signals are recorded versus time.
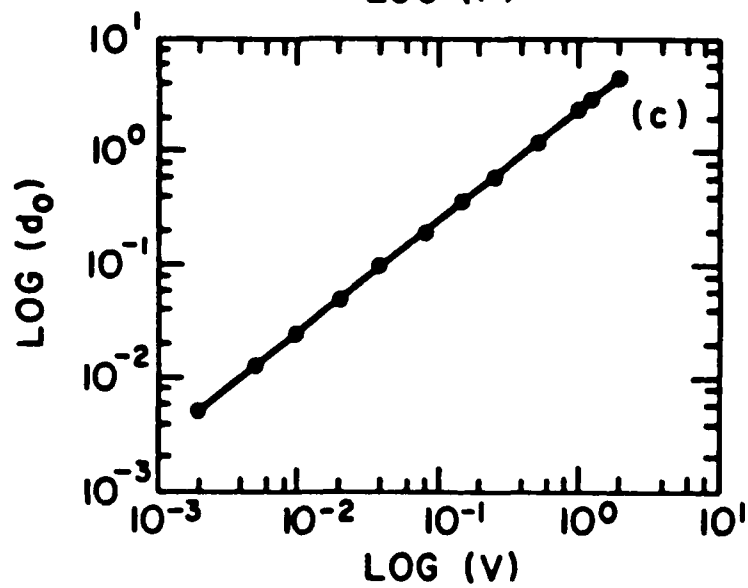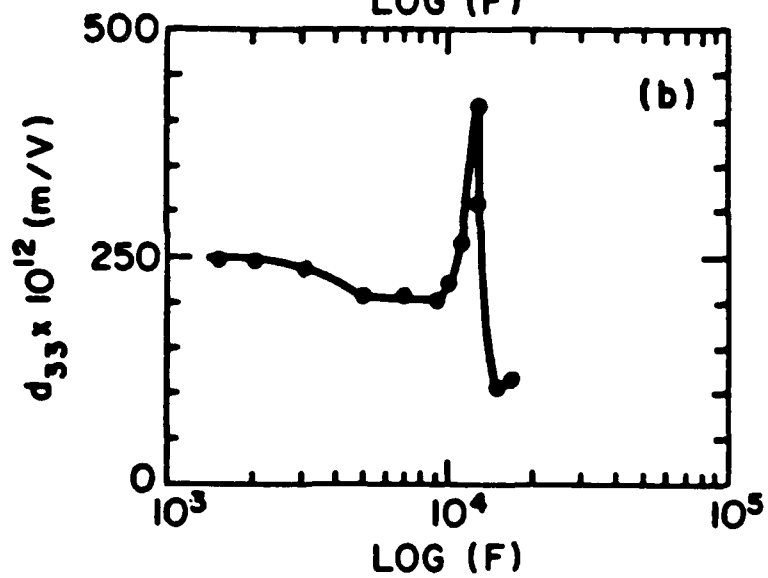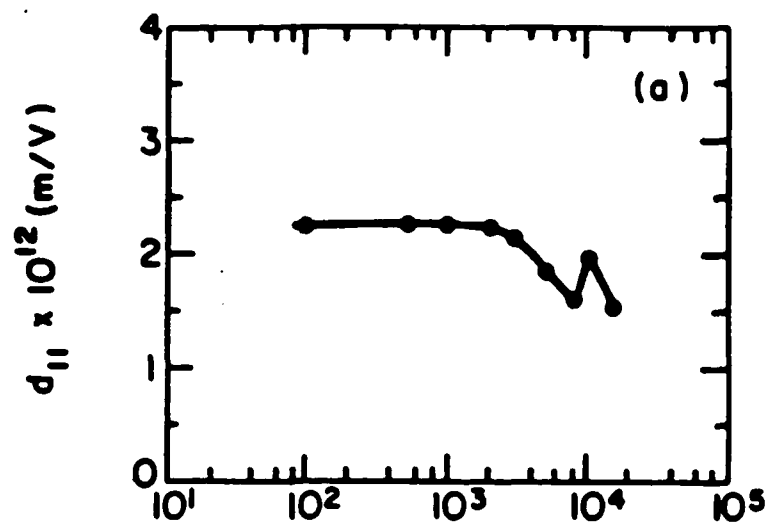
Figure 8.   Strain hysteresis loop for PLZT 8/65/35.

Figure 9.   Vacuum sample holder for the strain measurement. The holder base is attached to an optical stage which can move along x, y, z axis and rotate above x, z axis.
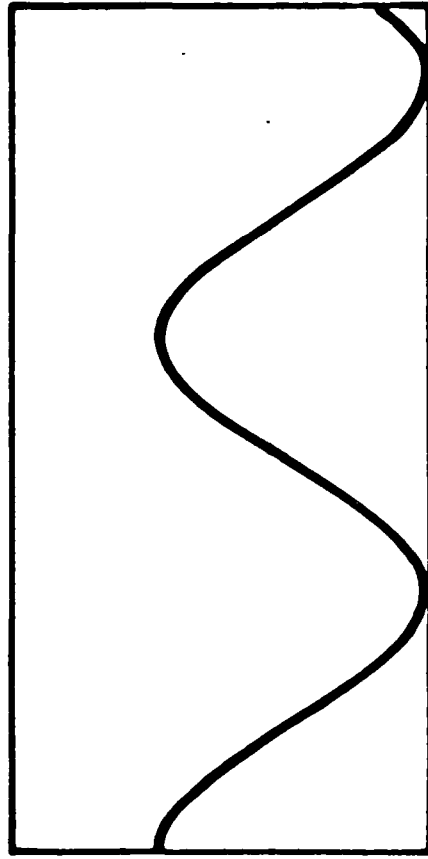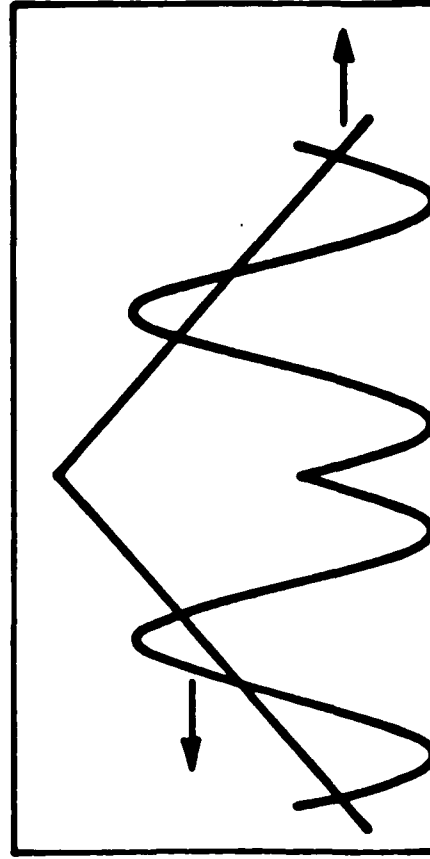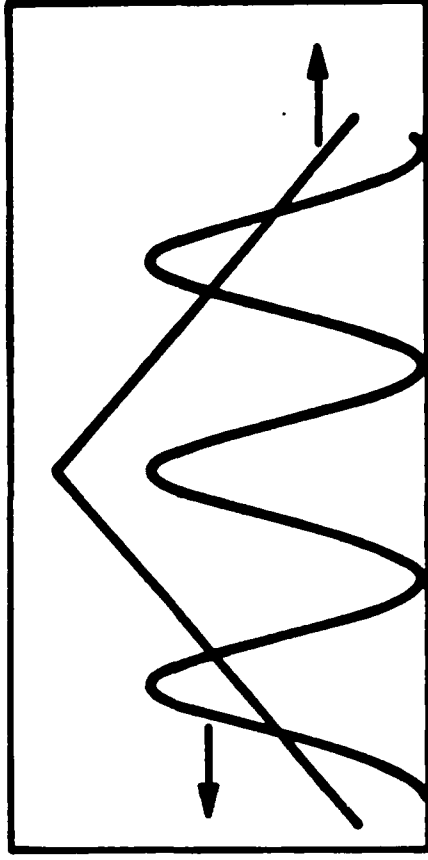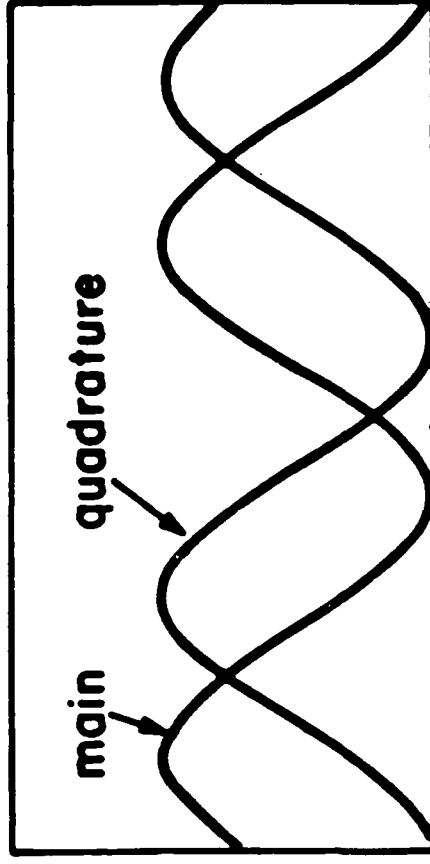
mass center

laser beam

Z

sample

bonding
material

sample
holder

3

Voltage

Time

(a)

(b)

(c)

sample is placed here

screw

top plate (brass)

rubber O-ring

1/4" pumping line

base (brass)

valve

plastic tube
to vacuum pump
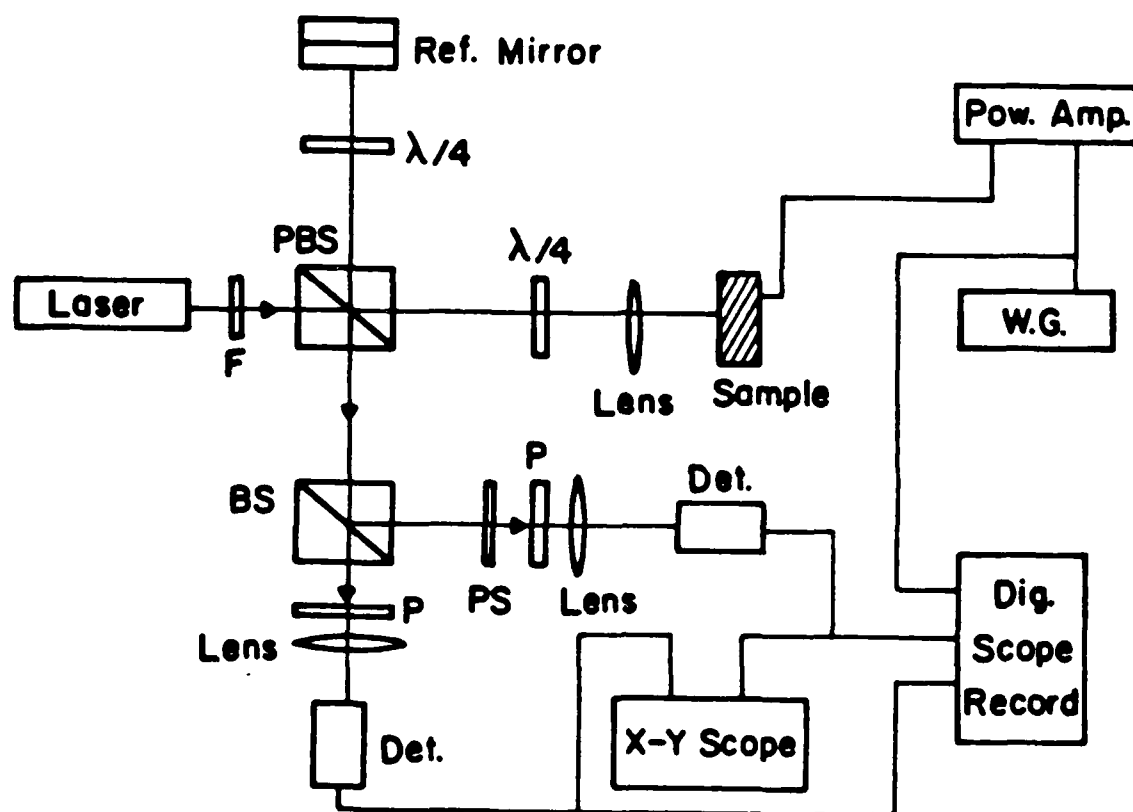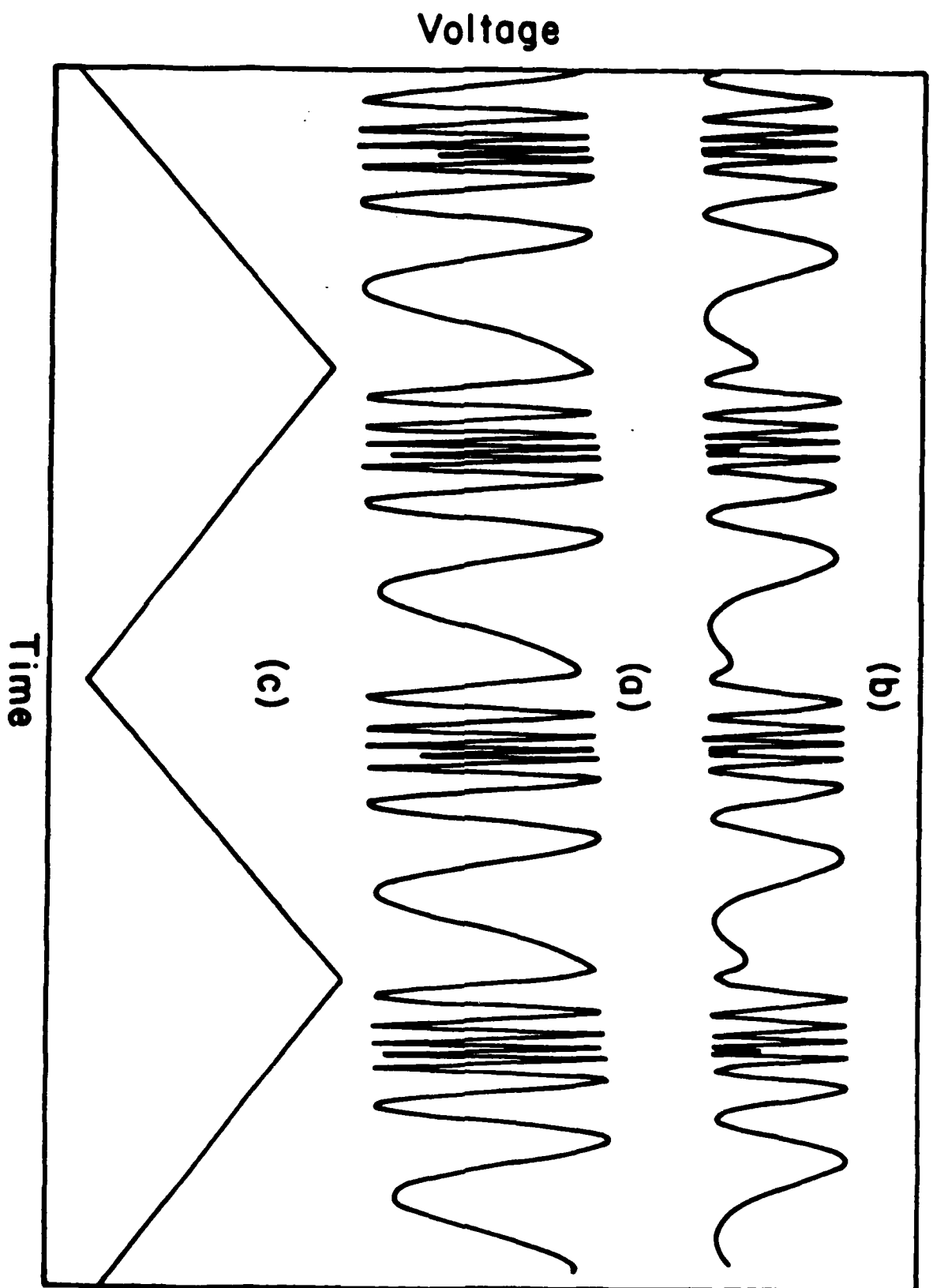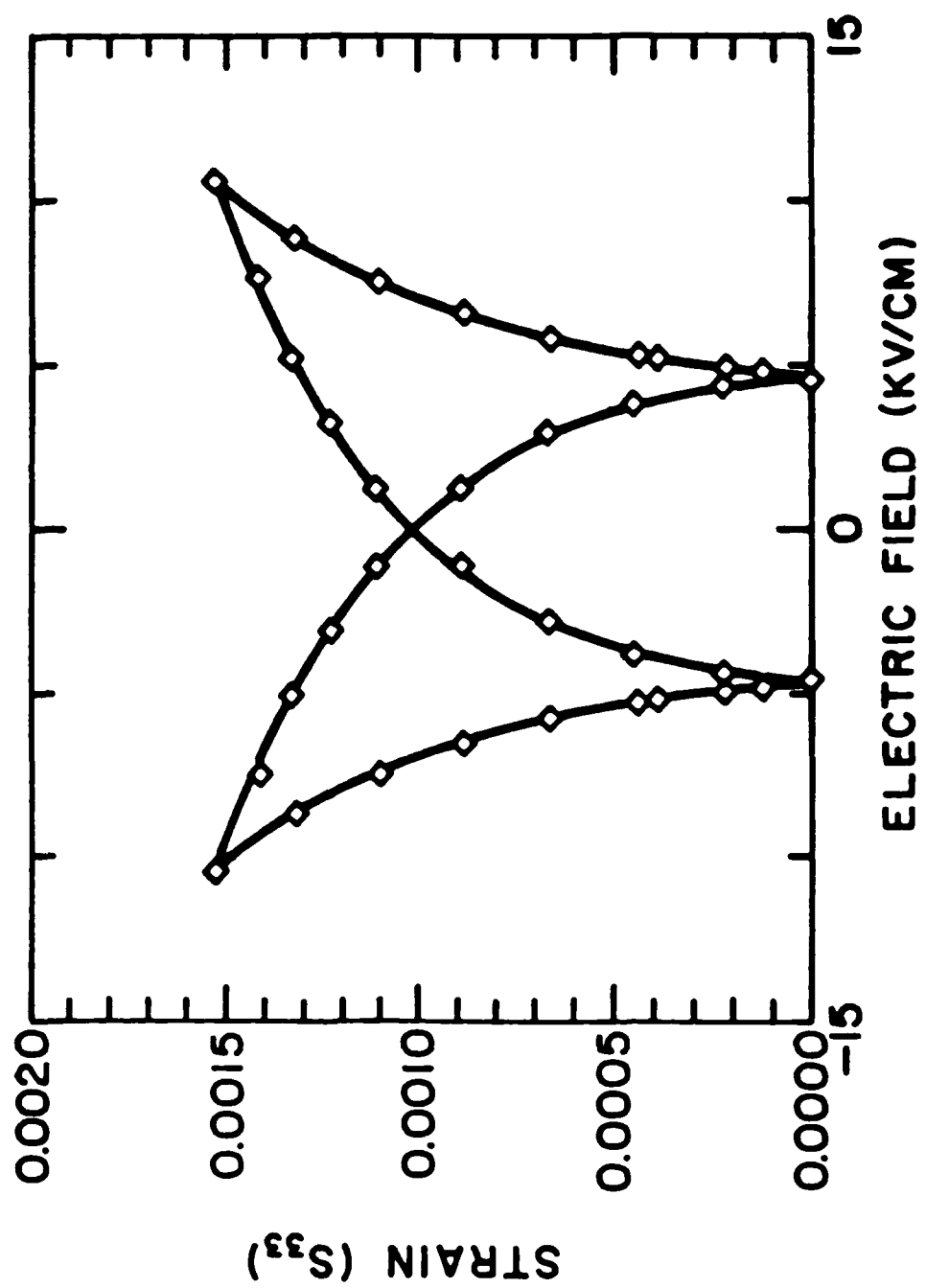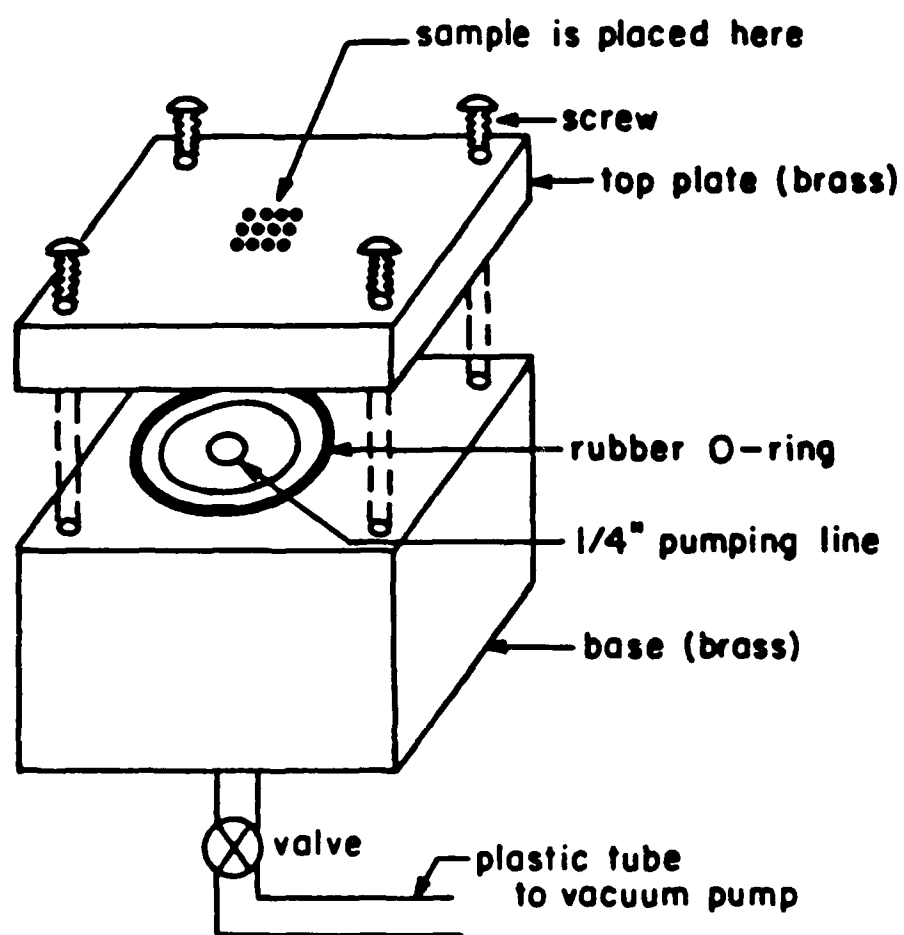
ISOTHERMAL AGING OF THE COMPLEX DIELECTRIC PERMITTIVITY IN MnO DOPED LEAD MAGNESIUM NIOBATE: LEAD TITANATE RELAXOR FERROELECTRIC CERAMICS

W.Y. Pan, Q.Y. Jiang, and L.E. Cross
Materials Research Laboratory
The Pennsylvania State University
University Park, PA 16802

ABSTRACT

Isothermal aging of the complex permittivity was investigated in MnO doped lead magnesium niobate: lead titanate (0.9 PMN: 0.1 PT) relaxor ferroelectric ceramics. Unlike most normal ferroelectrics, both real and imaginary parts of the permittivity deviate strongly from the logarithmic aging law, both curves tending to saturate at longer times. The effect is most pronounced in the imaginary part of the permittivity which approaches a nearly constant value quite quickly whilst the real part continues to age. The results can be explained using a model for the relaxor in which there is a distribution of micro-polar regions of varying size which contribute to the relaxation component of the polarizability. During aging it is postulated that defect dipoles induced by the aliovalent MnO doping reorient so as to stabilize the polar vector in the micro-polar regions. Larger regions stabilize first, removing the longer relaxation time processes and leading to a distribution richer in shorter relaxation times. That the K^1 vs. K^{11} plot taken over very long times shows no evidence of intersecting the K^1 axis at a large K^1 value suggests that the micro-polar regions still contribute a major part of the polarizability even after very long aging times. This datum is consistent with evidence from microwave and Raman spectroscopy that conventional soft modes are not major contributors to the dielectric response of relaxor ferroelectric.

Introduction

In normal ferroelectric ceramics, at temperatures below the ferroelectric Curie point, homogeneity of composition gives rise to a structure of polar macrodomains. For many such dielectrics the weak field dielectric permittivity is not strongly dispersive and under isothermal conditions the real part of the permittivity decays linearly with the logarithm of time, the so-called logarithmic aging law.

For lead zirconate: titanate ceramics, Arlt has shown that there is a strong domain wall contribution to the permittivity, and that it is this dispersive component which carries the aging phenomenon. Plotting real (K^1) versus imaginary (K^{11}) components as a function of time exhibits a

series of straight lines for different frequencies which extrapolate for ∞ time to a constant value on the K^1 axis. It is suggested that this value is the average of the intrinsic single domain permittivities (1).

In relaxor ferroelectrics, the situation is rather different. Compositional heterogeneity on a very fine scale   gives rise, on lowering temperature, to a sub-structure of polar micro-regions (2). Earlier studies of aging in $PbMg_{1/3}Nb_{2/3}O_3$: $PbTiO_3$ with a manganese oxide dopant (3) showed that for frequencies in the relaxation range the aging is <u>not</u> a linear function of the logarithm of time.

This paper attempts a more thorough study of the aging process in this relaxor and postulates a model to account for the behavior.

Experimental Procedure

The ceramic samples of the 0.9 PMN: 0.1 PT composition used in this study were prepared using mixed oxides in the manner described earlier by Swartz and Shrout (4,5). In this processing MgO and Nb_2O_5 are first reacted in a pre-calcine to form the columbite structure $MgNb_2O_6$ which is then reacted with PbO to for the $Pb_3MgNb_2O_9$ composition. For doping, the MnO was introduced using a dilute solution of $Mn(NO_3)_2$ added to the calcine. The final sintered samples were all above 97% theoretical density and were shown by X-ray diffraction to be free from contamination with the pyrochlore phase.

Dielectric constant values measured on freshly de-aged samples showed little variation with different MnO concentrations in the range up to 0.1% (by weight) used in this study.

Aging was accomplished in an isothermal chamber maintained at constant temperature by circulating water from a temperature controlled bath. For temperatures above 22° C fluctuations in the aging chamber were less than 0.1^O C over the 1,000 minute aging cycle. Below 22° C control was by mixing heated and cooled water and was better than 0.2^O C. Dielectric properties were measured using a Hewlett Packard LCR meter (Model 427A) under full computer control. Before measurement all samples were de-aged above 150° C and field levels used during the study were maintained at 10 v/cm on all samples.

Results and Discussion

Figure 1 and Figure 2 show data for the isothermal aging of a 0.9 PMN: 0.1 PT ceramic with a .1 (wt) % doping of MnO measured at 1, 10, and 100 KHz and a constant 37° C temperature. Clearly

series of straight lines for different frequencies which extrapolate for ∞ time to a constant value on the K^1 axis. It is suggested that this value is the average of the intrinsic single domain permittivities (1).

In relaxor ferroelectrics, the situation is rather different. Compositional heterogeneity on a very fine scale gives rise, on lowering temperature, to a sub-structure of polar micro-regions (2). Earlier studies of aging in $PbMg_{1/3}Nb_{2/3}O_3$: $PbTiO_3$ with a manganese oxide dopant (3) showed that for frequencies in the relaxation range the aging is not a linear function of the logarithm of time.

This paper attempts a more thorough study of the aging process in this relaxor and postulates a model to account for the behavior.

Experimental Procedure

The ceramic samples of the 0.9 PMN: 0.1 PT composition used in this study were prepared using mixed oxides in the manner described earlier by Swartz and Shrout (4,5). In this processing MgO and Nb_2O_5 are first reacted in a pre-calcine to form the columbite structure $MgNb_2O_6$ which is then reacted with PbO to for the $Pb_3MgNb_2O_9$ composition. For doping, the MnO was introduced using a dilute solution of $Mn(NO_3)_2$ added to the calcine. The final sintered samples were all above 97% theoretical density and were shown by X-ray diffraction to be free from contamination with the pyrochlore phase.

Dielectric constant values measured on freshly de-aged samples showed little variation with different MnO concentrations in the range up to 0.1% (by weight) used in this study.

Aging was accomplished in an isothermal chamber maintained at constant temperature by circulating water from a temperature controlled bath. For temperatures above 22° C fluctuations in the aging chamber were less than 0.1° C over the 1,000 minute aging cycle. Below 22° C control was by mixing heated and cooled water and was better than 0.2° C. Dielectric properties were measured using a Hewlett Packard LCR meter (Model 427A) under full computer control. Before measurement all samples were de-aged above 150° C and field levels used during the study were maintained at 10 v/cm on all samples.

Results and Discussion

Figure 1 and Figure 2 show data for the isothermal aging of a 0.9 PMN: 0.1 PT ceramic with a .1 (wt) % doping of MnO measured at 1, 10, and 100 KHz and a constant 37° C temperature. Clearly

neither K^1 nor K^{11} are linear functions of the logarithm of time and this is typical for all MnO doped samples. An alternative presentation of the same data is given in Figure 3, where K^1 vs. K^{11} for the three frequencies again taken at 37° C are plotted. At the lower 1 KHz frequency it is evident that the sample loses K^1 rapidly with only a small change in K^{11} and that for all frequencies if there is an intersection of the K^1 axis on extrapolation beyond the present time scale, it must occur at much lower K^1 values. Plots of the relative changes $\Delta K^1/K^1$ vs $\Delta K^{11}/K^{11}$ (Figure 4) again confirm the non-linearity for all three frequencies.

That the aging process is defect controlled is confirmed by the data in Figure 5 which examines the time dependence of K^1 as a function of MnO concentration. Clearly, the undoped samples show no aging and qualitatively the aging rate increases with increasing MnO concentration. From isothermal aging studies at different temperature (Figure 6) the behavior is similar to that for room temperature but with slightly faster aging rates at the lower temperatures. In Figure 7 the data are replotted so as to emphasize the relative changes $\Delta K^1/K_o^1$ vs $\Delta K^{11}/K_o^{11}$ bringing the curves to a common origin and underscoring the decrease of the change in loss for a given change in permittivity as the temperature increases.

To explain the observed behavior, we speculate that the aging mechanism is the same as that in conventional ferroelectric dielectrics and is due to the slow reorientation of defect dipoles under the effective field of the polar domains stabilizing the existing domain configuration. We believe that the obvious differences in the behavior of the relaxor ferroelectrics are due to their unusual sub-structure of polar micro-regions in which the polar vectors are being constantly reoriented by thermal fluctuations.

The proposed explanation is then as follows: in the temperature range above the dielectric maximum T_c the PMN: PT is made up of small polar micro-regions in a non-polar but very high K matrix phase. Because the regions are very small (~ 200 A° diameter) their P_s vectors are unstable against thermal motion and are constantly switching between alternative orientation states. It is modulation of these orientations by the weak external measuring field which contributes a major part of the dielectric permittivity.

The polar sub-domain structure is engendered by the local compositional heterogeneity (local Mg: Nb ratio), but because of this local heterogeneity translational symmetry is lost and the local (micro-region) symmetry is lower than the global prototype crystal symmetry. Under this circumstance the various orientations for P_s in the micro-region will now be of slightly differing energies. Now, although the polar vector in the micro-region will still suffer step wise reorientation by thermal vibrations, because of the inequivalence in energy states it will tend to spend longer times in the lowest energy minimum, thus imparting a weak time averaged polarization to the micro-region.

In the doped ceramic, this time average polarization will act to reorient the Mn induced defect dipoles so as to slowly stabilize this lowest energy state. As the energy of this state is lowered, the ability of the weak measuring field to modulate the orientation is lost and thus the dispersive component of the polarizability ages out.

Exploring now the effects on the frequency spectrum of permittivity, on the model of flipping micro-polar regions, the energy barrier over which P_s must be carried for reorientation (H) must be proportional to the volume of the micro-region. Since the flipping frequency υ is given by

$$\upsilon = \upsilon_0 \, e^{-H/kT}$$

where υ_0 is a lattice vibration frequency,

    K is the Boltzmann constant,

    H is the local energy barrier.

    The larger micro-regions will be slower switching but will also have the larger local dipole moment since this local moment μ is simply given by $v\,P_s$ where v is the polar volume.

    In normal dipolar dielectrics, the energetics are such that

$$\mu E \ll kT \ll H.$$

    Under these circumstances, the fractional ordering imposed by the E field is trivial and the polarizability a linear function of E up to very high fields.

    For the ferroelectric relaxor the local moment μ is much larger and for the larger micro-regions

μE may approach kT at modest E fields. Evidence for this energy balance may be adduced from the strong non-linearity of the polarization, particularly for temperatures close to T_c.

In the doped ceramic, the larger slower switching regions will spend longer times in the preferred orientation position and thus will begin to reorient the dipolar defect structure. The orienting defects will generate an effective dipolar field E_d further stabilizing P_s, as the preferred well deepens

the μE_d term will slowly override kT rendering the longer relaxation times inoperative. Thus we expect on aging that the distribution of relaxation times will change so as to favor the shorter times.

This scenario is depicted schematically in Figure 8. As the distribution function changes due to the aging process, we expect the trace for a single frequency to follow a path such as that delineated in Figure 8, i.e., a continuous change of K^l which at longer times shows little or no change in K^{ll}.

At present the explanation proposed above is largely speculation, however the pattern is consistent with more recent studies on aging under DC bias, which permit an assessment of E_d the effective defect field (6) and there is now clear evidence of polar micro-regions in pure PMN which are stabilized at nitrogen temperature and observed in transmission electron microscopy (7).

References

1. H. Dederiehs, G. Arlt, Ferroelectrics, Vol. 68, pp. 281-292 (1986).

2. P. Asadipour, U. Kumar, S.J. Jang, A.S. Bhalla, and L.E. Cross, Japanese Journal of Applied Physics, Vol. 24, Supplement 24-2, pp. 742-743 (1985).

3. W.Y. Pan, E. Furman, G.O. Dayton, and L.E. Cross, J. of Mat. Sci. Let., pp. 647-649 (1986).

4. S.L. Swartz and T.R. Shrout, Mat. Res. Bull., 17, pp. 1245-1250 (1982).

5. S.L. Swartz, T.R. Shrout, W.A. Schulze, and L.E. Cross, J. Amer. Cer. Soc., 67, pp. 311-315 (1984).

6. W.Y. Pan, Q.Y. Jiang, and L.E. Cross, submitted to J. of Amer. Cer. Soc.

7. Clive Alan Randall, Ph.D. Thesis, March 7, 1987, Dept. of Physics, University of Essex, United Kingdom.
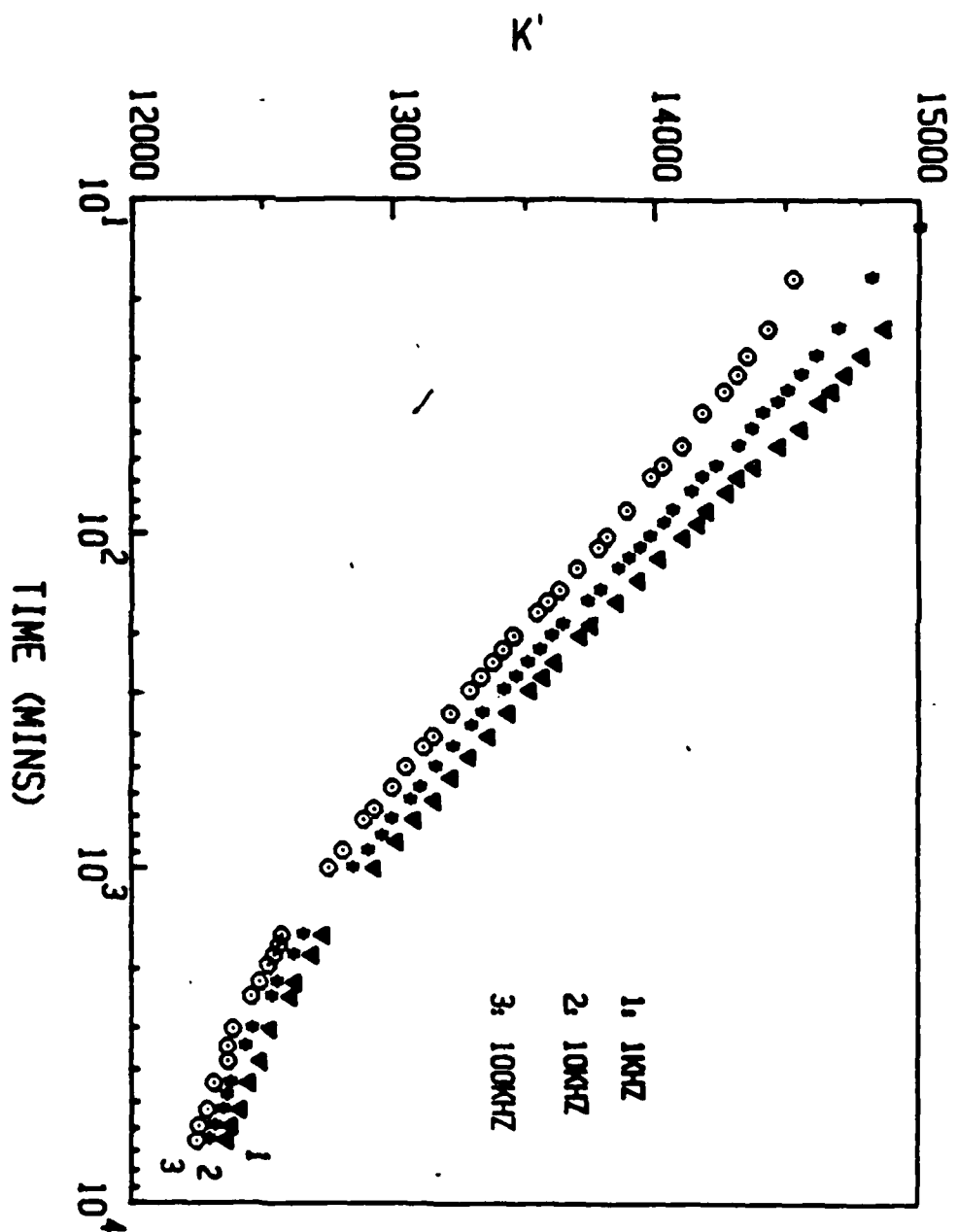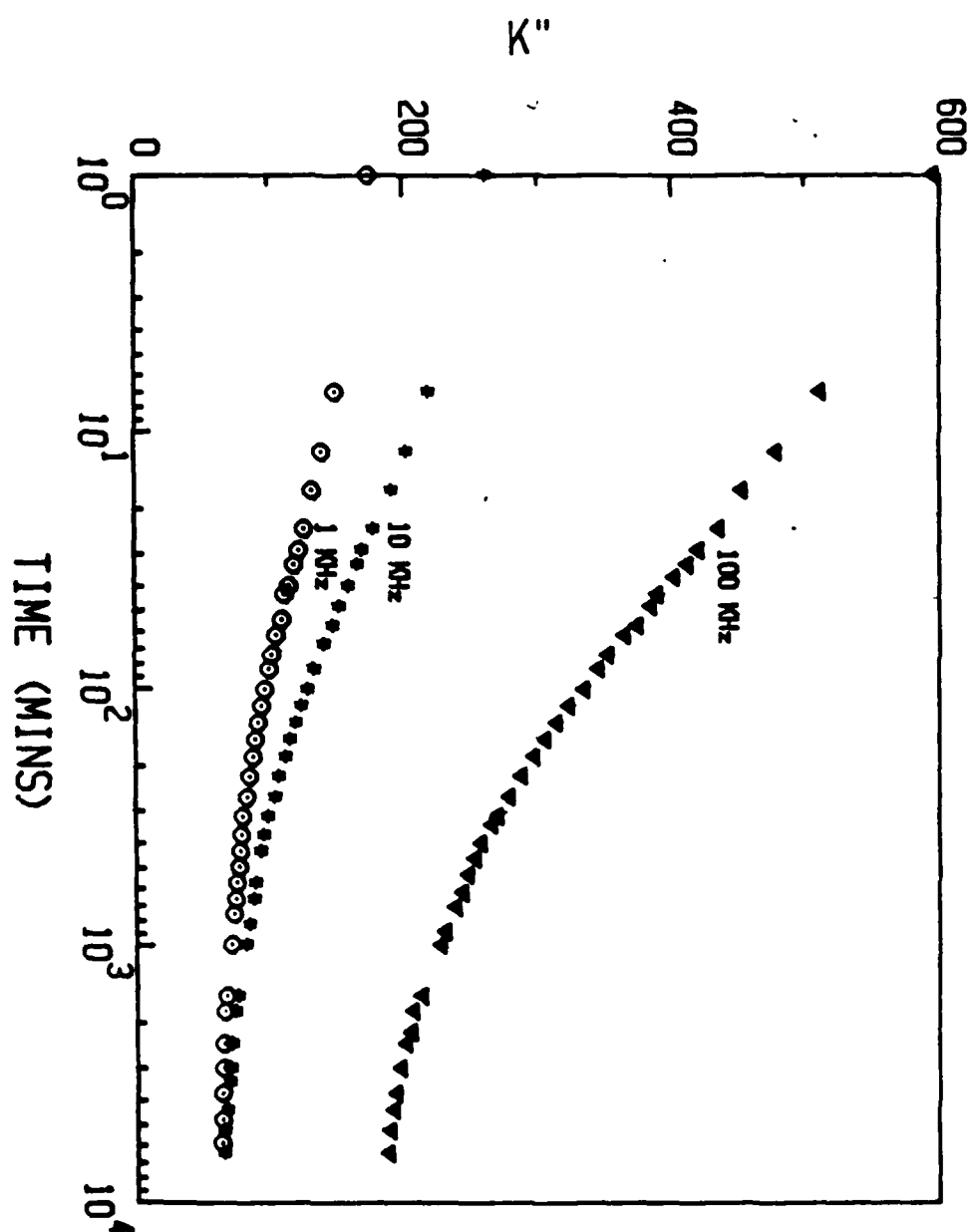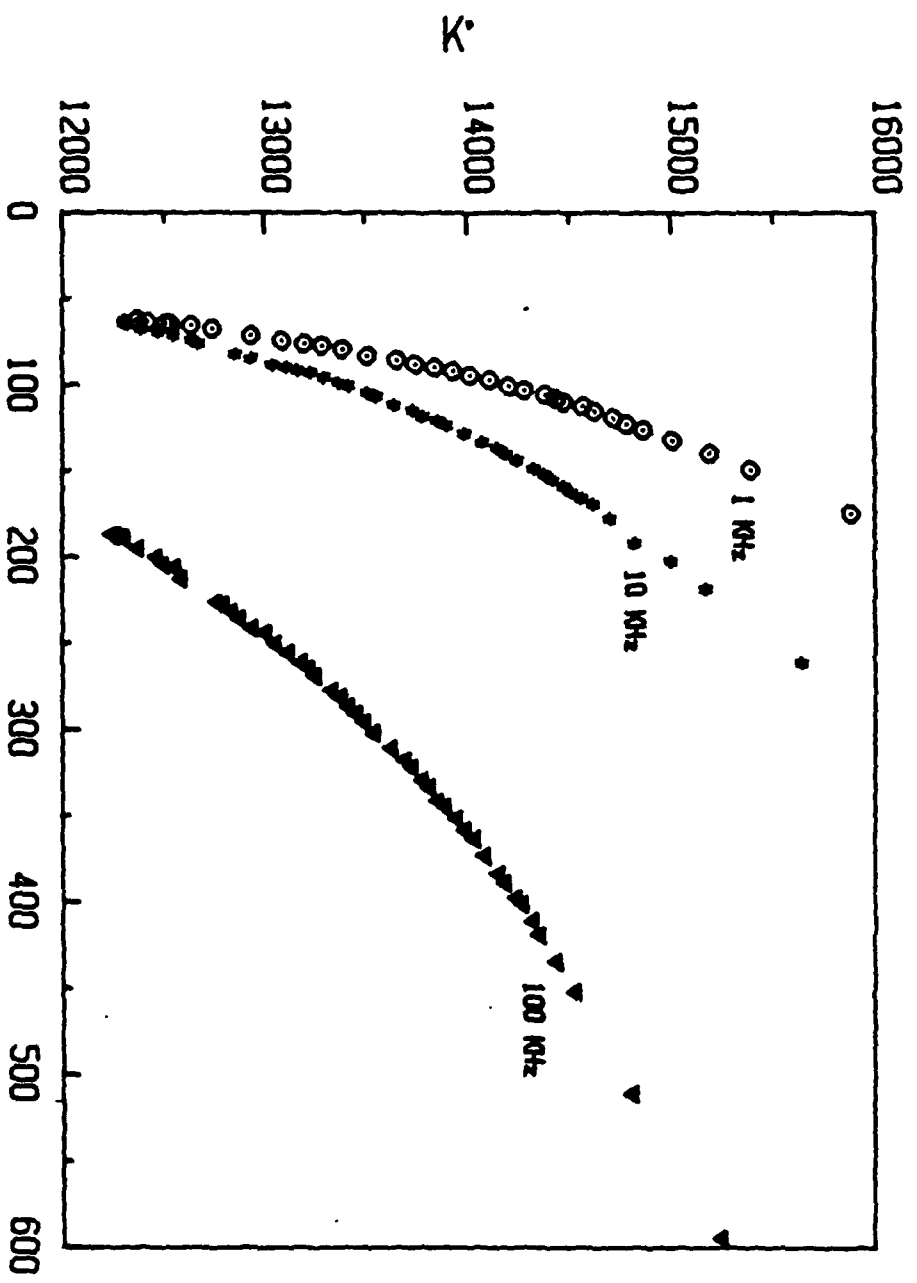
List of Figures

Figure 1.

K'

TIME (MINS)

1: 1KHZ
2: 10KHZ
3: 100KHZ

K"

TIME (MINS)

Figure 2.

Figure 3.

Fig. 4

Fig. 5

TIME (MINS)
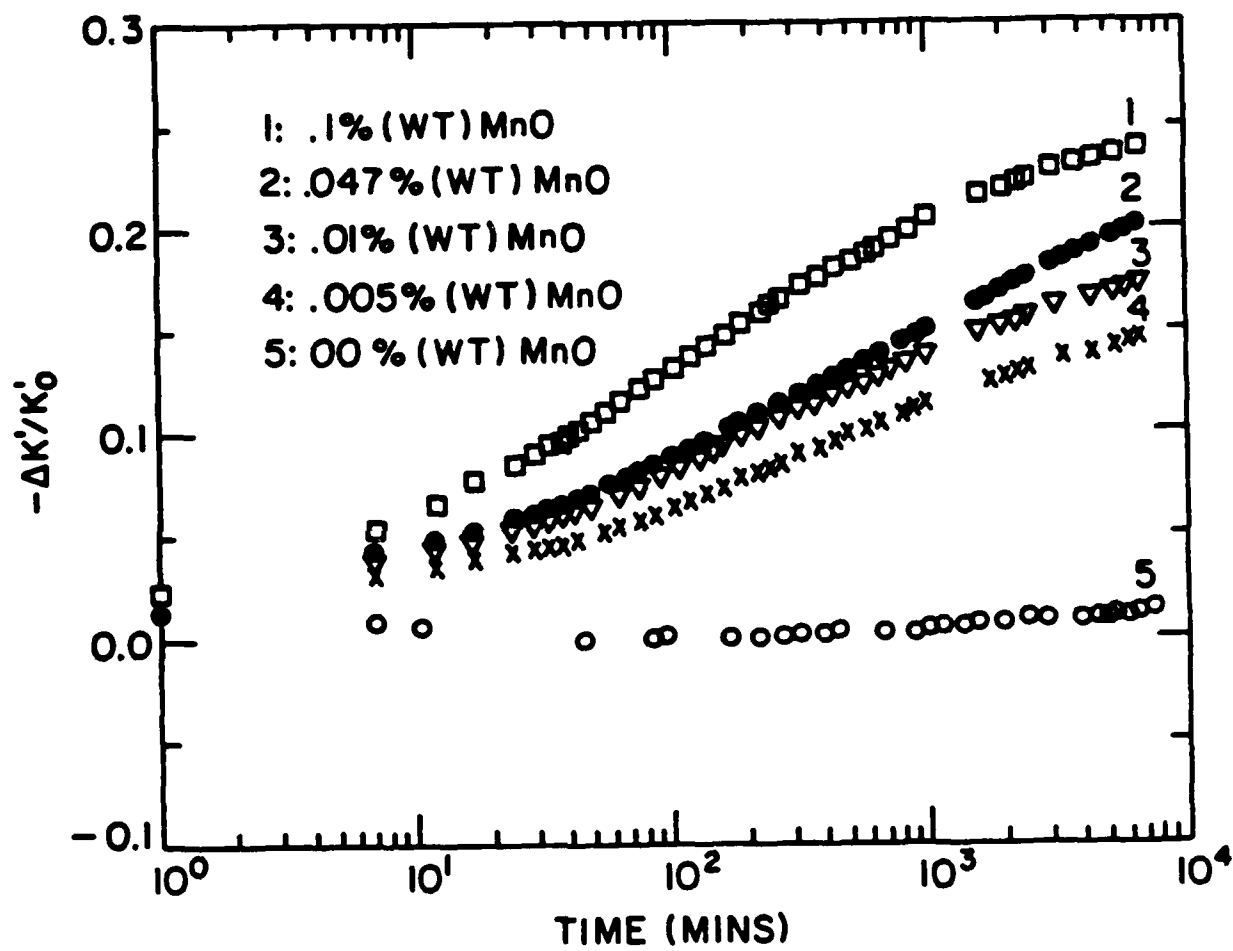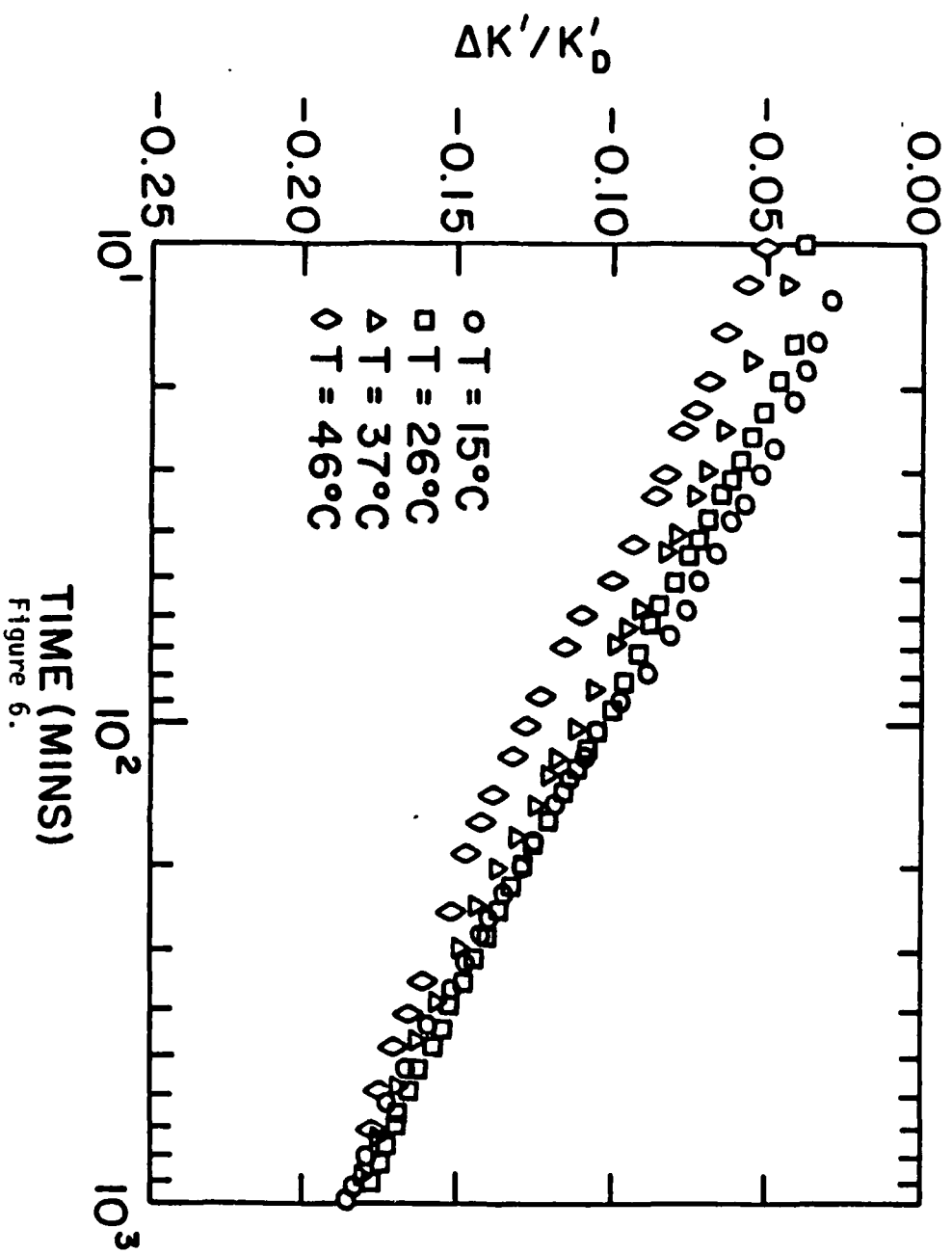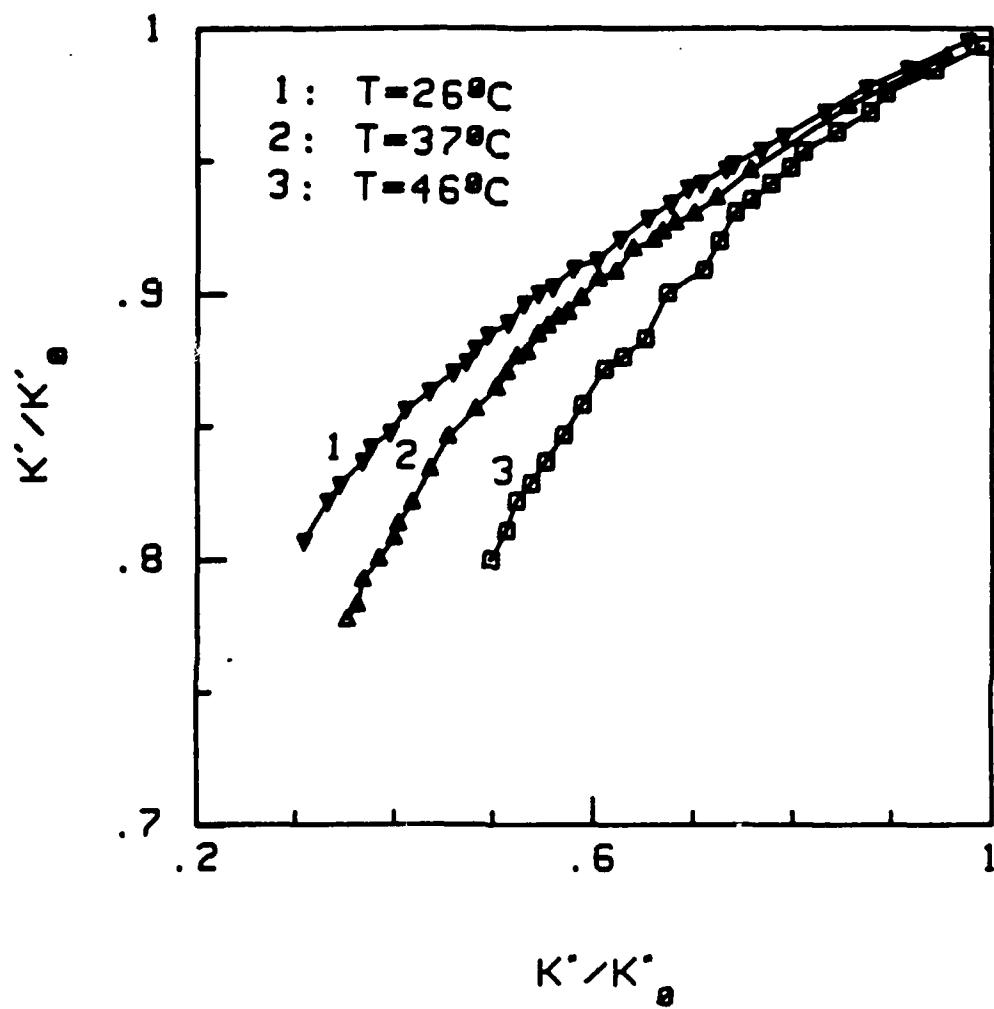
Figure 6.

Fig. 7
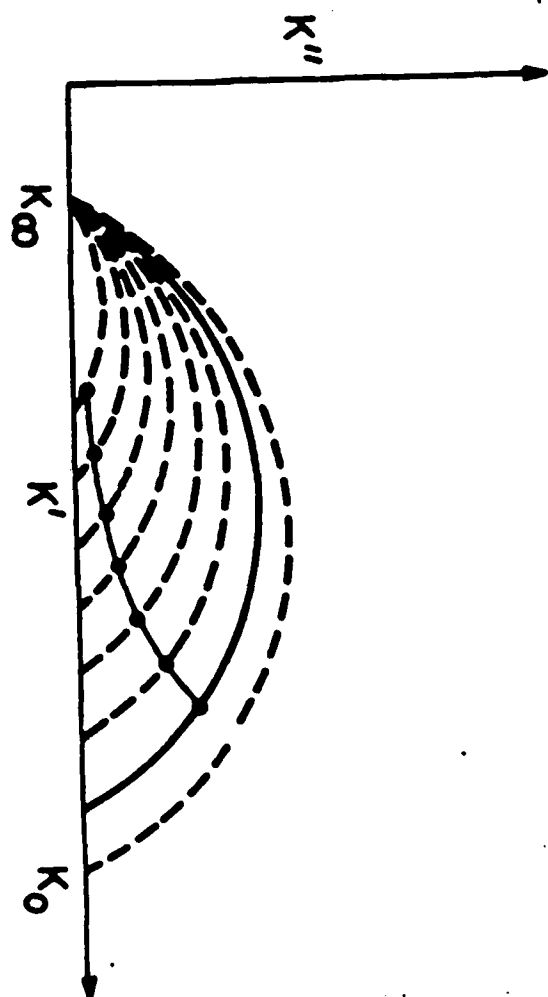
Fig. 8

Phenomenology and Properties of Conventional Ceramic Piezoelectrics

THERMODYNAMIC THEORY OF THE LEAD ZIRCONATE-TITANATE
SOLID SOLUTION SYSTEM, PART I: PHENOMENOLOGY

M. J. Haun[†], E. Furman[††], S. J. Jang, and L. E. Cross

Materials Research Laboratory
The Pennsylvania State University
University Park, PA 16802

Compositions within the lead zirconate-titanate (PZT) solid solution system have been extensively used in polycrystalline ceramic form in a wide range of piezoelectric transducer applications. However, the growth of good quality PZT single crystals for compositions across the entire phase diagram has not been accomplished. Due to the lack of single-crystal data, an understanding of the properties of polycrystalline PZT has been limited. If the single domain (intrinsic) properties of PZT could be determined, then the extrinsic contributions (e.g. domain wall and defect motions) to the polycrystalline properties could be separated from the intrinsic contributions. The purpose of this research has been to develop a thermodynamic phenomenological theory to model the phase transitions and single-domain properties of the PZT system.

This paper is the first of a series of five papers describing the thermodynamic theory of PZT that has been developed for the entire solid solution system. In this paper the previous work that led to the present theory will first be reviewed, followed by the presentation of the energy function for PZT, and the solutions and property relations that can be derived from this energy function.

[†]Now at Du Pont Experimental Station, Electronics Dept., Bldg. 334, Wilmington, DE, 19898.

[††]Now at Allied-Signal Inc., Morristown, NJ, 07960

I. INTRODUCTION

The lead zirconate-titanate (PZT) phase diagram[1] is shown in Figure 1. A cubic paraelectric phase (P_C) occurs at high temperatures and has the perovskite crystal structure ABO_3. On the lead titanate ($PbTiO_3$) side of the phase diagram, a ferroelectric tetragonal phase (F_T) exists with a spontaneous polarization along the pseudocubic [001] direction. A morphotropic boundary separates the tetragonal phase from a ferroelectric high-temperature rhombohedral phase ($F_{R(HT)}$).

Another ferroelectric to ferroelectric phase transition occurs between the high-temperature rhombohedral phase and a low-temperature rhombohedral phase ($F_{R(LT)}$). Both of these rhombohedral phases have a spontaneous polarization that occurs along the [111] direction. The low-temperature rhombohedral phase has a tilting or rotation of the oxygen octahedra about the [111] axis, which does not occur in the high-temperature phase.

On the lead zirconate side of the phase diagram antiferroelectric tetragonal (A_T) and orthorhombic (A_O) phases are present. These antiferroelectric phases are composed of two sublattices with equal and opposite polarization, resulting in zero net polarization.

More recent data[2] have shown that the A_T phase does not occur in pure lead zirconate, but will occur with small dopants or impurities such as strontium. These data have also shown that the high-temperature rhombohedral phase extends over to lead zirconate. The theory described in this paper will be developed to model the phase diagram according to these recent data.

PZT compositions have important technological applications as piezoelectric transducers, pyroelectric detectors, electro-optic devices, and explosively induced charge storage devices. The main application of PZT has been as piezoelectric transducers with compositions near the tetragonal-rhombohedral morphotropic boundary. These applications include phonograph pickups, buzzers, relays, accelerometers, igniters, micropositioners, hydrophones, sonar, wave filters, earphones, delay line welders, cutters, and high voltage sources.[1] Recently piezoelectric motors have even been made.[3,4]

Lead titanate has become important for possible application in hydrophones and medical ultrasonic imaging, because of the large electromechanical anisotropy that can be obtained in lead titanate polycrystalline ceramics[5]. The theory developed in this paper has been used to explain this large anisotropy, which occurs in lead titanate in polycrystalline form, but not in single-crystal form[6].

PZT compositions with the high to low temperature rhombohedral phase transition have been used as pyroelectric detectors[7]. When cooling through this transition, the polarization increases suddenly due to a contribution from the tilting of the oxygen octahedra in the low-temperature phase. This results in a large pyroelectric coefficient. The dielectric constant is relatively low, and only has a very slight change when going through this transition. A large pyroelectric coefficient p (= dP_S/dT) and small dielectric constant K result in a large pyroelectric figure of merit (= $p/K^{1/2}$).

PZT is also an important material for electrooptic applications, when doped with lanthanum to form PLZT. According to Haertling and Land[8], PLZT has advantages in electrooptic applications because of "1) high transparency essentially independent of grain size, 2) ease of fabrication, and 3) electrically variable optical retardation, including electrooptic memory and linear or quadratic modulation capabilities".

Explosively induced charge storage devices have also been fabricated from PZT compositions utilizing the ferroelectric to antiferroelectric transition. In these applications a stress is applied to a poled ceramic sample with the ferroelectric structure, causing it to transform to the antiferroelectric state and to suddenly release the stored charge.

The applications described above show that PZT is an important material. These applications use PZT in polycrystalline ceramic form. The growth of good quality PZT single crystals for compositions across the entire phase diagram has not been accomplished.[9] Due to the lack of single-crystal data, an understanding of the properties of ceramic PZT has been limited. If the single-domain properties of PZT could be determined, then these intrinsic contributions to the ceramic properties could be separated from the extrinsic

contributions (e.g. domain wall and defect motions). The purpose of this research has been to develop a thermodynamic phenomenological theory to predict the phase transitions and single-domain properties of the PZT system. This theory could then be used to further the understanding of the properties of polycrystalline materials.

This paper is the first of a series of five papers covering the details of the thermodynamic theory of PZT that has been developed for the entire solid solution system. In this paper the previous work that led to the present theory will first be reviewed, followed by the presentation of the energy function for PZT, and the solutions and property relations that can be derived from this energy function. In the next three papers[10-12] the coefficients of the energy function will be determined from experimental data. Finally in the last paper of the series[13] theoretical calculations of the PZT single-domain properties will be presented, along with a discussion of the applications of the theory.

II. DEVELOPMENT OF A THERMODYNAMIC THEORY OF PZT

The Landau-Ginsburg-Devonshire type phenomenological theory was used to explain the transitions and properties at the tetragonal-rhombohedral morphotropic phase boundary in the PZT system.[14-21] However, due to the lack of single-crystal data the coefficients of the energy function could not be adequately determined.

Over the past several years at the Materials Research Laboratory of the Pennsylvania State University, the coefficients of an energy function for the PZT system have been determined using indirect methods. The development of this theory occurred in a series of steps, where different parts of the phase diagram were modeled separately. This development will be described below.

Amin[22] developed a modified Devonshire form of the elastic Gibbs free energy function for the simple proper ferroelectric phases of the PZT system. The spontaneous strain in the ferroelectric phases was determined using high-temperature x-ray diffraction,

and used to calculate the spontaneous polarization through the electrostrictive constants. These data were used to determine the higher order dielectric stiffness coefficients (α_{11} and α_{111}). The morphotropic boundary between the tetragonal and rhombohedral phases was then used to determine the remaining higher-order dielectric stiffness coefficients (α_{12}, α_{112}, and α_{123}), and allowed for the first time the calculation of the dielectric, piezoelectric, elastic, and thermal properties of the ferroelectric single-domain states. This theory was developed for the region of the PZT system from lead titanate over to the morphotropic boundary between the tetragonal and rhombohedral phases, and could be extrapolated into the high-temperature rhombohedral phase field.

In this initial theory the Curie constant was assumed to be independent of composition. Amin et al.[23] later found from a combination of calorimetric and phenomenological data that the Curie constant was dependent on composition with a peak forming near the morphotropic boundary. The theory was then modified to account for the compositional dependence of the Curie constant.[24] This resulted in better agreement between the theoretical and experimental dielectric data near the morphotropic boundary.

To account for the tilting of the oxygen octahedra in the low-temperature rhombohedral phase Halemane et al.[25] expanded the energy function in a one-dimensional power series of the polarization (P) and tilt angle (θ) assuming isothermal and zero stress conditions. The possible phase transition sequences and solutions to the energy function were then investigated. This theory was applied to the $Pb(Zr_{0.9}Ti_{0.1})O_3$ composition, first by assuming 2nd order phase transitions,[25] and later by assuming 1st order transitions[26,27].

The energy function was then expanded in a three-dimensional power series of P and θ and used to describe all of the ferroelectric phases of the PZT system assuming 1st order phase transitions.[28] The coefficients of the energy function were determined from the phase boundary and equilibrium conditions combined with experimental data, resulting in smooth continuous functions across the phase diagram. The experimental and theoretical

phase diagrams were shown to agree very well. Using this theory the spontaneous polarization and tilt angle were calculated as a function of composition and temperature.

A tricritical point, where a phase transition changes from first to second order, was found to occur between the cubic and rhombohedral phases at the PZT 94/6 composition (94% PZ and 6% PT).[29-31] From lead zirconate to the tricritical point the cubic-rhombohedral transition was shown to be first order, and then to change to second order from the tricritical point over to at least the PZT 88/12 composition.[30] Lead titanate has a first order transition from cubic to tetragonal, and thus a second tricritical point should occur between the PZT 88/12 and lead titanate compositions, where the transition would change back to first order.

To provide additional data to determine the coefficients of the energy function and to locate the second tricritical point, pure homogeneous sol-gel derived PZT powders were prepared for several compositions in the rhombohedral phase field.[32] The lattice parameters of these compositions were determined from high-temperature x-ray diffraction, and used to calculate the spontaneous strain.[33] By using these data to determine the higher-order dielectric stiffness coefficients of the energy function, the second order transition region was found to extend over to near or possibly at the morphotropic boundary.[34] Additional details of the tricritical behavior in PZT will be described in the second paper in this series.[10]

Using the x-ray data described above a phenomenological theory was developed to account for the 2nd order transition region of the PZT system.[34] In this theory additional terms were added to the energy function to account for the rotostrictive coupling between the stress and the square of the tilt angle (analogous to the electrostrictive coupling). A rotostrictive constant was determined from experimental spontaneous strain, polarization, and tilt angle data using a relation derived from the energy function for the low-temperature rhombohedral phase. The rotostrictive contribution to the spontaneous strain was found to be opposite in sign to the electrostrictive contribution.

A more complete phenomenological theory of lead titanate was recently developed independently of the PZT theory using the available single crystal data.[35] The theoretically predicted spontaneous polarization and strains, and dielectric and piezoelectric properties are in good agreement with the experimental data. The results of this theory were used to show that the large electromechanical anisotropy found in lead titanate ceramics, but not present in the single crystal properties, is simply due to the intrinsic averaging of the electrostrictive constants.[6,36]

A phenomenological theory for lead zirconate was also developed independently of the PZT theory using the available single-crystal data.[37] This theory was used to calculate the phase stability, antiferroelectric spontaneous strain, and ferroelectric polarization and strain. The polycrystalline ceramic dielectric constant was calculated from the single-crystal constants in this theory, and found to be in good agreement with microwave dielectric data. This lead zirconate theory was also extended into the the PZT system to account for the antiferroelectric region of the phase diagram.

As described above phenomenological theory has been developed for different sections of the PZT phase diagram. The purpose of this series of papers is to present the recent work that has been completed to combine these separate theories into a complete theory of PZT, where a single energy function and set of coefficients can be used to calculate the phase stability and properties of the entire PZT system. In the next section this energy function will be presented.

III. FREE ENERGY FUNCTION FOR PZT

In developing a phenomenological theory for the PZT system the order parameters that cause the phase transitions must be accounted for. The tetragonal and high-temperature rhombohedral phases undergo proper ferroelectric transitions from the paraelectric cubic state, where the spontaneous polarization is the order parameter causing the phase transition.

An improper ferroelectric phase transition occurs between the high and low temperature rhombohedral phases, where the spontaneous tilting of the oxygen octahedra causes the phase transition and contributes to the spontaneous polarization. An antiferroelectric type polarization develops when transforming from the ferroelectric to antiferroelectric phases and is therefore the order parameter for the antiferroelectric state.

Thus to account for all of the phase transitions in the PZT system the energy function should include the ferroelectric and antiferroelectric measures of the polarization, and the tilting of the oxygen octahedra as order parameters. A two-sublattice model[38] was used to derive the ferroelectric and antiferroelectric measures of the polarization. To account for the tilting of the oxygen octahedra an additional term was added to the elastic Gibbs free energy as described in References 25-28.

The following energy function for the PZT system was then derived from the symmetry of the paraelectric phase (m3m) assuming isothermal conditions, using reduced notation, and expanding the energy function in powers of the ferroelectric (P_i) and antiferroelectric (p_i) polarizations, oxygen octahedral tilt angle (θ_i), and including couplings between these order parameters and between the stress (X_m) and the order parameters:

$$
\begin{aligned}
\Delta G = {}& \alpha_1 [P_1^2 + P_2^2 + P_3^2] + \alpha_{11} [P_1^4 + P_2^4 + P_3^4] \\
&+ \alpha_{12} [P_1^2 P_2^2 + P_2^2 P_3^2 + P_3^2 P_1^2] + \alpha_{111}[P_1^6 + P_2^6 + P_3^6] \\
&+ \alpha_{112} [P_1^4 (P_2^2 + P_3^2) + P_2^4 (P_1^2 + P_3^2) + P_3^4 (P_1^2 + P_2^2)] \\
&+ \alpha_{123} P_1^2 P_2^2 P_3^2 + \sigma_1 [p_1^2 + p_2^2 + p_3^2] + \sigma_{11} [p_1^4 + p_2^4 + p_3^4] \\
&+ \sigma_{12} [p_1^2 p_2^2 + p_2^2 p_3^2 + p_3^2 p_1^2] + \sigma_{111} [p_1^6 + p_2^6 + p_3^6] \\
&+ \sigma_{112} [p_1^4 (p_2^2 + p_3^2) + p_2^4 (p_1^2 + p_3^2) + p_3^4 (p_1^2 + p_2^2)] \\
&+ \sigma_{123} p_1^2 p_2^2 p_3^2 + \mu_{11} [P_1^2 p_1^2 + P_2^2 p_2^2 + P_3^2 p_3^2] \\
&+ \mu_{12} [P_1^2 (p_2^2 + p_3^2) + P_2^2 (p_1^2 + p_3^2) + P_3^2 (p_1^2 + p_2^2)] \\
&+ \mu_{44} [P_1 P_2 p_1 p_2 + P_2 P_3 p_2 p_3 + P_3 P_1 p_3 p_1] + \beta_1 [\theta_1^2 + \theta_2^2 + \theta_3^2] \\
&+ \beta_{11} [\theta_1^4 + \theta_2^4 + \theta_3^4] + \gamma_{11} [P_1^2 \theta_1^2 + P_2^2 \theta_2^2 + P_3^2 \theta_3^2]
\end{aligned}
$$

$$+ \gamma_{12} [P_1^2 (\theta_1^2 + \theta_2^2) + P_2^2 (\theta_1^2 + \theta_3^2) + P_3^2 (\theta_1^2 + \theta_2^2)]$$

$$+ \gamma_{44} [P_1 P_2 \theta_1 \theta_2 + P_2 P_3 \theta_2 \theta_3 + P_3 P_1 \theta_3 \theta_1]$$

$$- 1/2\, S_{11}[X_1^2 + X_2^2 + X_3^2] - S_{12} [X_1 X_2 + X_2 X_3 + X_3 X_1]$$

$$- 1/2\, S_{44} [X_4^2 + X_6^2 + X_6^2] - Q_{11} [X_1 P_1^2 + X_2 P_2^2 + X_3 P_3^2]$$

$$- Q_{12} [X_1 (P_2^2 + P_3^2) + X_2 (P_1^2 + P_3^2) + X_3 (P_1^2 + P_2^2)]$$

$$- Q_{44} [X_4 P_2 P_3 + X_5 P_1 P_3 + X_6 P_1 P_2] - Z_{11} [X_1 p_1^2 + X_2 p_2^2 + X_3 p_3^2]$$

$$- Z_{12} [X_1 (p_2^2 + p_3^2) + X_2 (p_1^2 + p_3^2) + X_3 (p_1^2 + p_2^2)]$$

$$- Z_{44} [X_4 p_2 p_3 + X_5 p_1 p_3 + X_6 p_1 p_2] - R_{11} [X_1 \theta_1^2 + X_2 \theta_2^2 + X_3 \theta_3^2]$$

$$- R_{12} [X_1 (\theta_2^2 + \theta_3^2) + X_2 (\theta_1^2 + \theta_3^2) + X_3 (\theta_1^2 + \theta_2^2)]$$

$$- R_{44} [X_4 \theta_2 \theta_3 + X_5 \theta_1 \theta_3 + X_6 \theta_1 \theta_2] \tag{1}$$

The coefficients of this energy function are defined in Table I. The energy function includes all possible ferroelectric and antiferroelectric polarization terms up to the sixth order, tilt angle terms up to the first fourth order term, and only the first order coupling terms.

IV. SOLUTIONS TO THE ENERGY FUNCTION

The following solutions to the energy function (Equation 1) are of interest in the PZT system:

Paraelectric Cubic (P_C)
$$P_1 = P_2 = P_3 = 0, \qquad p_1 = p_2 = p_3 = 0, \qquad \theta_1 = \theta_2 = \theta_3 = 0 \tag{2}$$

Ferroelectric Tetragonal (F_T)
$$P_1 = P_2 = 0, \quad P_3^2 \neq 0, \qquad p_1 = p_2 = p_3 = 0, \qquad \theta_1 = \theta_2 = \theta_3 = 0 \tag{3}$$

Ferroelectric Orthorhombic (F_O)
$$P_1 = 0, \quad P_2^2 = P_3^2 \neq 0, \qquad p_1 = p_2 = p_3 = 0, \qquad \theta_1 = \theta_2 = \theta_3 = 0 \tag{4}$$

Ferroelectric High-temperature Rhombohedral ($F_{R(HT)}$)

$$P_1^2 = P_2^2 = P_3^2 \neq 0, \qquad p_1 = p_2 = p_3 = 0, \qquad \theta_1 = \theta_2 = \theta_3 = 0 \qquad (5)$$

Ferroelectric Low-temperature Rhombohedral ($F_{R(LT)}$)

$$P_1^2 = P_2^2 = P_3^2 \neq 0, \qquad p_1 = p_2 = p_3 = 0, \qquad \theta_1^2 \neq \theta_2^2 \neq \theta_3^2 \neq 0 \qquad (6)$$

Antiferroelectric Orthorhombic (A_O)

$$P_1 = P_2 = P_3 = 0, \qquad p_1 = 0, \; p_2^2 = p_3^2 \neq 0, \qquad \theta_1 = \theta_2 = \theta_3 = 0 \qquad (7)$$

All of these solutions, except for the ferroelectric orthorhombic solution, are stable in the PZT system. The ferroelectric orthorhombic solution was also included here, because the coefficients necessary to calculate the energy of this phase can be determined. An independent check of the coefficients can then be made by checking if this phase is metastable across the PZT system, as it should be experimentally.

Applying these solutions to Equation (1) under zero stress conditions results in the following relations for the energies of each solution:

P_C $$\Delta G = 0 \qquad (8)$$

F_T $$\Delta G = \alpha_1 P_3^2 + \alpha_{11} P_3^4 + \alpha_{111} P_3^6 \qquad (9)$$

F_O $$\Delta G = 2\,\alpha_1 P_3^2 + (2\,\alpha_{11} + \alpha_{12})\,P_3^4 + 2\,(\alpha_{111} + \alpha_{112})\,P_3^6 \qquad (10)$$

$F_{R(HT)}$ $$\Delta G = 3\,\alpha_1 P_3^2 + 3\,(\alpha_{11} + \alpha_{12})\,P_3^4 + (3\,\alpha_{111} + 6\,\alpha_{112} + \alpha_{123})\,P_3^6 \qquad (11)$$

$F_{R(LT)}$ $$\Delta G = 3\,\alpha_1 P_3^2 + 3\,(\alpha_{11} + \alpha_{12})\,P_3^4 + (3\,\alpha_{111} + 6\,\alpha_{112} + \alpha_{123})\,P_3^6$$
$$+ 3\,\beta_1 \theta_3^2 + 3\,\beta_{11} \theta_3^4 + 3\,(\gamma_{11} + 2\,\gamma_{12} + \gamma_{44})P_3^2 \theta_3^2 \qquad (12)$$

A_O $$\Delta G = 2\,\sigma_1 p_3^2 + (2\,\sigma_{11} + \sigma_{12})\,p_3^4 + 2\,(\sigma_{111} + \sigma_{112})\,p_3^6 \qquad (13)$$

The spontaneous ferroelectric and antiferroelectric polarizations (P_3 and p_3) and tilt angle (θ_3) in the above equations can be found from the first partial derivative stability

conditions ($\partial \Delta G/\partial P_3$, $\partial \Delta G/\partial p_3$, and $\partial \Delta G/\partial \theta_3$) as shown below:

$$F_T \qquad \partial \Delta G/\partial P_3 = 0 = 3 \, \alpha_{111} P_3^4 + 2 \, \alpha_{11} P_3^2 + \alpha_1 \qquad (14)$$

$$F_O \qquad \partial \Delta G/\partial P_3 = 0 = 3 \, (\alpha_{111} + \alpha_{112}) \, P_3^4 + (2 \, \alpha_{11} + \alpha_{12}) \, P_3^2 + \alpha_1 \qquad (15)$$

$$F_{R(HT)} \quad \partial \Delta G/\partial P_3 = 0 = (3 \, \alpha_{111} + 6 \, \alpha_{112} + \alpha_{123}) \, P_3^4$$
$$+ \, 2 \, (\alpha_{11} + \alpha_{12}) \, P_3^2 + \alpha_1 \qquad (16)$$

$$F_{R(LT)} \quad \partial \Delta G/\partial P_3 = 0 = (3 \, \alpha_{111} + 6 \, \alpha_{112} + \alpha_{123}) \, P_3^4$$
$$+ \, 2 \, (\alpha_{11} + \alpha_{12}) \, P_3^2 + \alpha_1 + \gamma_{11} \theta_3^2 \qquad (17)$$
$$\partial \Delta G/\partial \theta_3 = 0 = \beta_1 + 2 \, \beta_{11} \theta_3^2 + \gamma_{11} P_3^2 \qquad (18)$$

$$A_O \qquad \partial \Delta G/\partial p_3 = 0 = 3 \, (\sigma_{111} + \sigma_{112}) \, p_3^4 + (2 \, \sigma_{11} + \sigma_{12}) \, p_3^2 + \sigma_1 \qquad (19)$$

The polarizations and tilt angle can be calculated by solving these quadratic equations. Equations (9) - (19) relate the energies of each solution to the coefficients of the energy function. Thus by determining these coefficients, the energies of each phase can be calculated.

V. SPONTANEOUS ELASTIC STRAINS

The spontaneous elastic strains x_i ($= \partial \Delta G/\partial X_i$) under zero stress conditions can be derived from Equation (1) as follows:

$$P_C \qquad x_1 = x_2 = x_3 = x_4 = x_5 = x_6 = 0 \qquad (20)$$

$$F_T \qquad x_1 = x_2 = Q_{12} P_3^2, \quad x_3 = Q_{11} P_3^2, \qquad x_4 = x_5 = x_6 = 0 \qquad (21)$$

$$F_O \qquad x_1 = 2 \, Q_{12} \, P_3^2, \quad x_2 = x_3 = (Q_{11} + Q_{12}) \, P_3^2,$$
$$x_4 = Q_{44} \, P_3^2, \quad x_5 = x_6 = 0 \qquad (22)$$

$$F_{R(HT)} \quad x_1 = x_2 = x_3 = (Q_{11} + 2 \, Q_{12}) \, P_3^2, \qquad x_4 = x_5 = x_6 = Q_{44} \, P_3^2 \qquad (23)$$

$$F_{R(LT)} \quad x_1 = x_2 = x_3 = (Q_{11} + 2 Q_{12}) P_3{}^2 + (R_{11} + 2 R_{12}) \theta_3{}^2,$$
$$x_4 = x_5 = x_6 = Q_{44} P_3{}^2 + R_{44} \theta_3{}^2 \tag{24}$$

$$A_O \quad x_1 = 2 Z_{12} p_3{}^2, \quad x_2 = x_3 = (Z_{11} + Z_{12}) p_3{}^2,$$
$$x_4 = Z_{44} p_3{}^2, \quad x_5 = x_6 = 0 \tag{25}$$

In the next three papers of this series[10-12] these spontaneous strain relations will be shown to be very important in determining the coefficients of the energy function. Spontaneous strain data will be determined from x-ray diffraction of PZT powders, and used with the electrostrictive constants to calculate the spontaneous polarization, which is needed to determine coefficients of the energy function.

VI. DIELECTRIC PROPERTIES

Relations for the relative dielectric stiffnesses χ_{ij} ($= \partial^2 \Delta G / \partial P_i \partial P_j$) were derived from Equation (1) for the six solutions:

$$P_C \quad \chi_{11} = \chi_{22} = \chi_{33} = 2 \varepsilon_0 \alpha_1, \quad\quad \chi_{12} = \chi_{23} = \chi_{31} = 0 \tag{26}$$

$$F_T \quad \chi_{11} = \chi_{22} = 2 \varepsilon_0 [\alpha_1 + \alpha_{11} P_3{}^2 + \alpha_{111} P_3{}^4],$$
$$\chi_{33} = 2 \varepsilon_0 [\alpha_1 + 6 \alpha_{11} P_3{}^2 + 15 \alpha_{111} P_3{}^4], \quad \chi_{12} = \chi_{23} = \chi_{31} = 0 \tag{27}$$

$$F_O \quad \chi_{11} = 2 \varepsilon_0 [\alpha_1 + 2 \alpha_{12} P_3{}^2 + (2 \alpha_{112} + \alpha_{123}) P_3{}^4],$$
$$\chi_{22} = \chi_{33} = 2 \varepsilon_0 [\alpha_1 + (6 \alpha_{11} + \alpha_{12}) P_3{}^2 + (15 \alpha_{111} + 7 \alpha_{112}) P_3{}^4],$$
$$\chi_{12} = \chi_{31} = 0, \quad\quad \chi_{23} = 4 \varepsilon_0 [\alpha_{12} P_3{}^2 + 4 \alpha_{112} P_3{}^4] \tag{28}$$

$$F_{R(HT)} \quad \chi_{11} = \chi_{22} = \chi_{33} = 2 \varepsilon_0 [\alpha_1 + (6 \alpha_{11} + 2 \alpha_{12}) P_3{}^2$$
$$+ (15 \alpha_{111} + 14 \alpha_{112} + \alpha_{123}) P_3{}^4],$$
$$\chi_{12} = \chi_{23} = \chi_{31} = 4 \varepsilon_0 [\alpha_{12} P_3{}^2 + (4 \alpha_{112} + \alpha_{123}) P_3{}^4] \tag{29}$$

$$F_{R(LT)} \quad \chi_{11} = \chi_{22} = \chi_{33} = 2 \varepsilon_0 [\alpha_1 + (6 \alpha_{11} + 2 \alpha_{12}) P_3{}^2$$
$$+ (15 \alpha_{111} + 14 \alpha_{112} + \alpha_{123}) P_3{}^4 + (\gamma_{11} + 2 \gamma_{12}) \theta_3{}^2],$$
$$\chi_{12} = \chi_{23} = \chi_{31} = 4 \varepsilon_0 [\alpha_{12} P_3{}^2 + (4 \alpha_{112} + \alpha_{123}) P_3{}^4 + \gamma_{44} \theta_3{}^2] \tag{30}$$

$$A_O \qquad \chi_{11} = 2\,\varepsilon_0\,[\alpha_1 + 2\,\mu_{12}\,P_3{}^2], \quad \chi_{22} = \chi_{33} = 2\,\varepsilon_0\,[\alpha_1 + (\mu_{11} + \mu_{12})\,P_3{}^2],$$
$$\chi_{12} = \chi_{31} = 0, \qquad \chi_{23} = \varepsilon_0\,\mu_{44}\,P_3{}^2 \tag{31}$$

The multiplication by the permittivity of free space ε_0 in these equations was required to convert from absolute to relative dielectric stiffnesses. Equations (26) - (31) can be used to calculate the relative dielectric stiffnesses for each phase based on the original cubic axes.

In the orthorhombic state the polarization can be along any of the $<110>$ directions of the original cubic axes. The polarization of the rhombohedral state can be along any of the $<111>$ directions. By rotating these axes so that for both states the new x_3 axis is along the polar directions, diagonalized matrices will result. The new dielectric stiffness coefficients (indicated by a prime) can be related to the old coefficients [defined by equations (28) - (31)] with the following relations:

$$F_O\ and\ A_O \qquad \chi_{11}{}' = \chi_{11}, \qquad \chi_{22}{}' = \chi_{33} - \chi_{23}$$
$$\chi_{33}{}' = \chi_{33} + \chi_{23}, \qquad \chi_{12}{}' = \chi_{23}{}' = \chi_{31}{}' = 0 \tag{32}$$

$$F_{R(HT)}\ and\ F_{R(LT)} \qquad \chi_{11}{}' = \chi_{22}{}' = \chi_{11} - \chi_{12}, \qquad \chi_{33}{}' = \chi_{11} + 2\,\chi_{12}$$
$$\chi_{12}{}' = \chi_{23}{}' = \chi_{31}{}' = 0 \tag{33}$$

These equations can be used to calculate the dielectric stiffnesses of the orthorhombic and rhombohedral phases parallel and perpendicular to the polar axes.

The dielectric susceptibility coefficients (η_{ij}) can be determined from the reciprocal of the dielectric stiffness matrices (χ_{ij}) using the following relation[39]:

$$\eta_{ij} = A_{ji}/\Delta, \tag{34}$$

where A_{ji} and Δ are the cofactor and determinant of the χ_{ij} matrix. Using this relation results in the following relations for the dielectric susceptibility coefficients (η_{ij}):

$$P_C \qquad \eta_{11} = \eta_{22} = \eta_{33} = 1/\chi_{11}, \qquad \eta_{12} = \eta_{23} = \eta_{31} = 0 \tag{35}$$

$$F_T \qquad \eta_{11} = \eta_{22} = 1/\chi_{11}, \qquad \eta_{33} = 1/\chi_{33} \tag{36}$$

$F_O \text{ and } A_O$ $\eta_{11} = 1/\chi_{11},$ $\eta_{22} = \eta_{33} = \chi_{33}/(\chi_{33}^2 - \chi_{23}^2),$

$\eta_{12} = \eta_{31} = 0,$ $\eta_{23} = -\chi_{23}/(\chi_{33}^2 - \chi_{23}^2)$ (37)

$\eta_{11}' = 1/\chi_{11}',$ $\eta_{22}' = 1/\chi_{22}',$ $\eta_{33}' = 1/\chi_{33}'$

$\eta_{12}' = \eta_{23}' = \eta_{31}' = 0$ (38)

$F_{R(HT)} \text{ and } F_{R(LT)}$

$\eta_{11} = \eta_{22} = \eta_{33} = (\chi_{11}^2 - \chi_{12}^2)/(\chi_{11}^3 - 3\chi_{11}\chi_{12}^2 + 2\chi_{12}^3)$

$\eta_{12} = \eta_{23} = \eta_{31} = (\chi_{12}^2 - \chi_{11}\chi_{12})/(\chi_{11}^3 - 3\chi_{11}\chi_{12}^2 + 2\chi_{12}^3)$ (39)

$\eta_{11}' = \eta_{22}' = 1/\chi_{11}',$ $\eta_{33}' = 1/\chi_{33}'$

$\eta_{12}' = \eta_{23}' = \eta_{31}' = 0$ (40)

These equations can be used to calculate the dielectric susceptibilities of each phase from the coefficients of the energy function.

VII. PIEZOELECTRIC PROPERTIES

Relations for the piezoelectric b_{ij} coefficients $(= \partial^2\Delta G/\partial P_i\partial X_j)$ were derived from Equation (1) for the tetragonal and rhombohedral states as shown below:

F_T $b_{33} = 2Q_{11}P_3,$ $b_{31} = b_{32} = 2Q_{12}P_3,$

$b_{15} = b_{24} = Q_{44}P_3,$ $b_{11} = b_{12} = b_{13} = b_{14} = b_{16} = 0,$

$b_{21} = b_{22} = b_{23} = b_{25} = b_{26} = b_{34} = b_{35} = b_{36} = 0$ (41)

$F_{R(HT)} \text{ and } F_{R(LT)}$

$b_{11} = b_{22} = b_{33} = 2Q_{11}P_3,$ $b_{14} = b_{25} = b_{36} = 0$

$b_{12} = b_{13} = b_{21} = b_{23} = b_{31} = b_{32} = 2Q_{12}P_3,$

$b_{15} = b_{16} = b_{24} = b_{26} = b_{34} = b_{35} = Q_{44}P_3,$ (42)

Since a coupling term of the type $X_iP_i\theta_i$ was not included in Equation (1), the b_{ij} relations [Equation (42)] for the high and low temperature rhombohedral phases are of the same form. However, the spontaneous polarizations P_3 are defined by different relations for

the high and low temperature rhombohedral phases, and thus different values would result for these coefficients.

The piezoelectric d_{ij} coefficients are defined by[40]:

$$d_{ij} = b_{kj} \, \eta_{ik} \tag{43}$$

Using this relation for the tetragonal and rhombohedral states results in the following relations:

F_T $d_{33} = 2\,\varepsilon_0\,\eta_{33}\,Q_{11}P_3,$ $d_{31} = d_{32} = 2\,\varepsilon_0\,\eta_{33}\,Q_{12}\,P_3,$

       $d_{15} = d_{24} = \varepsilon_0\,\eta_{11}\,Q_{44}\,P_3,$ $d_{11} = d_{12} = d_{13} = d_{14} = d_{16} = 0,$

$$d_{21} = d_{22} = d_{23} = d_{25} = d_{26} = d_{34} = d_{35} = d_{36} = 0 \tag{44}$$

$F_{R(HT)}$ and $F_{R(LT)}$

       $d_{11} = d_{22} = d_{33} = 2\,\varepsilon_0\,(\eta_{11}\,Q_{11} + 2\,\eta_{12}\,Q_{12})\,P_3,$

       $d_{12} = d_{13} = d_{21} = d_{23} = d_{31} = d_{32} = 2\,\varepsilon_0\,[\eta_{11}\,Q_{12} + \eta_{12}\,(Q_{11} + Q_{12})]\,P_3,$

       $d_{14} = d_{25} = d_{36} = 2\,\varepsilon_0\,\eta_{12}\,Q_{44}\,P_3,$

$$d_{15} = d_{16} = d_{24} = d_{26} = d_{34} = d_{35} = \varepsilon_0\,(\eta_{11} + \eta_{12})\,Q_{44}\,P_3, \tag{45}$$

The multiplication by the permittivity of free space ε_0 in these equations was required to convert the dielectric susceptibilities from relative to absolute. Equations (41), (42), (44), and (45) can be used to calculate the piezoelectric b_{ij} and d_{ij} coefficients of the tetragonal and rhombohedral phases from the coefficients of the energy function.

VIII. SUMMARY

The applications of compositions of the PZT solid solution system as piezoelectric transducers, pyroelectric detectors, electro-optic devices, and explosively induced charge storage devices were described in the introduction to demonstrate the technological importance of PZT. These applications use PZT in polycrystalline ceramic form, and thus the properties of these ceramics are well established in the literature. However, the

mechanisms contributing to these outstanding polycrystalline properties of PZT are not well understood, because of the complexity of the interactions within the polycrystalline material.

A first step in the analysis of a ferroelectric polycrystalline material is to separate the intrinsic and extrinsic contributions to the properties. The intrinsic contributions result from the averaging of the single-domain single-crystal properties, while the extrinsic contributions arise from the interactions at grain or phase boundaries and from the domain wall or thermal defect motions. Unfortunately, due to the difficulty of growing good quality single crystals of PZT, very little single-crystal data is available. Thus the goal of this project was to develop a thermodynamic phenomenological theory to calculate the single-domain properties of PZT. This theory could then be used to separate the intrinsic and extrinsic contributions to the polycrystalline properties. In addition there are several other applications of this theory, which will be in the last paper of this series.[13]

A two-sublattice theory, where each sublattice has a separate polarization, was used to account for the ferroelectric and antiferroelectric phases of the PZT system. An additional order parameter was also included to account for the tilting of the oxygen octahedra in the low-temperature rhombohedral phase. The resulting energy function can be used to model the phase transitions and single-domain properties of the PZT system. Solutions to this energy function were used to derive relations for the energies; spontaneous polarizations, strains, and tilt angles; and dielectric and piezoelectric properties corresponding to the different phases in the PZT system.

The coefficients needed to calculate the energies and properties of the solutions will be determined in the next three papers in this series.[10-12] Theoretical calculations and comparisons with experimental data will then be presented in the final paper of this series.[13] Additional details of this theory, including tables of all the experimental data collected, can be found in Reference 41.

REFERENCES

[1] B. Jaffe, W. J. Cook, and H. Jaffe, *Piezoelectric Ceramics* (Academic Press, London, 1971).

[2] R. W. Whatmore and A. M. Glazer, J. Phys. C: Solid State Phys. 12, 1505 (1979).

[3] A. Kumada, Jpn. J. Appl. Phys., 24 (Suppl. 24-2), 739 (1985).

[4] K. Uchino, Bull. Amer. Ceram. Soc., 65, 647 (1986).

[5] H. Takeuchi, S. Jyomura, C. Nakaya, Jpn. J. Appl. Phys., 24 (Suppl. 24-2), 36 (1985).

[6] M. J. Haun, E. Furman, S. J. Jang, and L. E. Cross, Trans. IEEE Ultrasonics, Ferroelectrics and Frequency Control Soc., (to be published).

[7] R. Clarke, A. M. Glazer, F. W. Ainger, D. Appleby, N. J. Poole, and S. G. Porter, Ferroelectrics, 11, 359 (1976).

[8] G. H. Haertling, and C. E. Land, J. Amer. Ceram. Soc., 54, 1 (1971).

[9] R. Clarke, and R. W. Whatmore, J. of Crystal Growth, 33, 29 (1976).

[10] M. J. Haun, E. Furman, H. A. McKinstry, and L. E. Cross, "Thermodynamic Theory of the Lead Zirconate-Titanate Solid Solution System, Part II: Tricritical Behavior," J. Appl. Phys. (submitted).

[11] M. J. Haun, Z. Q. Zhuang, E. Furman, S. J. Jang, and L. E. Cross, "Thermodynamic Theory of the Lead Zirconate-Titanate Solid Solution System, Part III: Curie Constant and Sixth-Order Polarization Interaction Dielectric Stiffness Coefficients," J. Appl. Phys. (submitted).

[12] M. J. Haun, E. Furman, T. R. Halemane, and L. E. Cross, "Thermodynamic Theory of the Lead Zirconate-Titanate Solid Solution System, Part IV: Tilting of the Oxygen Octahedra," J. Appl. Phys. (submitted).

[13] M. J. Haun, E. Furman, S. J. Jang, and L. E. Cross, "Thermodynamic Theory of the Lead Zirconate-Titanate Solid Solution System, Part V: Theoretical Calculations," J. Appl. Phys. (submitted).

[14]V. A. Isupov, Fizika Tverdogo Tela, 12, 1380 (1970) [Soviet Physics - Solid State, 12, 1084 (1970)].

[15]K. Carl and K. H. Hardtl, Phys. Stat. Sol. (a), 8, 87 (1971).

[16]V. A. Isupov, Fizika Tverdogo Tela, 18, 92 (1976) [Soviet Physics - Solid State, 18, 529 (1976)].

[17]V. A. Isupov, Ferroelectrics, 12, 141 (1976).

[18]V. A. Isupov, Fizika Tverdogo Tela, 19, 1347 (1977) [Soviet Physics - Solid State, 19, 783 (1977).

[19]W. Wersing, *Proceedings 4th Int. Meeting Electro- and Magnetoceramics* (1981) pp. 162-182.

[20]W. Wersing, Ferroelectrics, 37, 611 (1981).

[21]W. Wersing, Ferroelectrics, 54, 207 (1984).

[22]A. Amin, *Phenomenological and Structural Studies of Lead Zirconate - Titanate Piezoceramics*, Ph.D. Thesis in Solid State Science, The Pennsylvania State University (1979).

[23]A. Amin, A., L. E. Cross, and R. E. Newnham, Ferroelectrics, 37, 647 (1981).

[24]A. Amin, M. J. Haun, B. Badger, H. A. McKinstry, and L. E. Cross, Ferroelectrics, 65, 107 (1985).

[25]T. R. Halemane, M. J. Haun, L. E. Cross, and R. E. Newnham, Ferroelectrics, 62 149 (1985).

[26]T. R. Halemane, M. J. Haun, L. E. Cross, and R. E. Newnham, Jpn. J. App. Phys., 24 (Suppl. 24-2), 212 (1985).

[27]T. R. Halemane, M. J. Haun, L. E. Cross, and R. E. Newnham, Ferroelectrics 70, 153 (1986).

[28]M. J. Haun, T. R. Halemane, R. E. Newnham, and L. E. Cross, Jpn. J. App. Phys., 24 (Suppl. 24-2), 209 (1985).

[29]R. Clarke and A. M. Glazer, Ferroelectrics, 14, 695 (1976).

[30] R. W. Whatmore, R. W., R. Clarke, and A. M. Glazer, J. Phys. C: Solid State Phys., 11, 3089 (1978).

[31] K. Roleder and J. Handerek, Phase Transitions, 2, 285 (1982).

[32] Z. Q. Zhuang, M. J. Haun, S. J. Jang, and L. E. Cross, *Proceedings of the 6th IEEE International Symposium on the Applications of Ferroelectrics*, Lehigh, PA, edited by Van Wood (IEEE, New York, 1986) pp. 394-397.

[33] M. J. Haun, Y. H. Lee, H. A. McKinstry, and L. E. Cross, *Advances in X-ray Analysis, Vol. 30*, edited by C. S. Barrett, J. V. Gilfrich, R. Jenkins, D. E. Leyden, J. C. Russ, and P. K. Predecki (Plenum Press, New York, 1987) pp. 473-481.

[34] M. J. Haun, Z. Q. Zhuang, S. J. Jang, H. A. McKinstry, and L. E. Cross, *Proceedings of the 6th IEEE International Symposium on the Applications of Ferroelectrics*, Lehigh, PA, edited by Van Wood (IEEE, New York, 1986) pp. 398-401.

[35] M. J. Haun, E. Furman, S. J. Jang, H. A. McKinstry, and L. E. Cross, J. Appl. Phys., 62, 333 (1987).

[36] J. N. Kim, M. J. Haun, S. J. Jang, L. E. Cross, and X. R. Xue, Trans. IEEE Ultrasonics, Ferroelectrics and Frequency Control Soc. (to be published).

[37] M. J. Haun, T. J. Harvin, M. T. Lanagan, Z. Q. Zhuang, S. J. Jang, and L. E. Cross, J. Appl. Phys. (to be submitted).

[38] L. E. Cross, Phil. Mag., 1, 76 (1956).

[39] J. F. Nye, *Physical Properties of Crystals*, (University Press, Oxford, 1957), p. 156.

[40] A. F. Devonshire, Phil. Mag., 42, 1065 (1951).

[41] M. J. Haun, *Thermodynamic Theory of the Lead Zirconate-titanate Solid Solution System*, Ph.D. thesis in Solid State Science, The Pennsylvania State University (1988).

LIST OF FIGURES AND TABLES

Table I. Coefficients of the PZT Energy Function.

|	
$\alpha_i, \alpha_{ij}, \alpha_{ijk}$	ferroelectric dielectric stiffnesses at constant stress
$\sigma_i, \sigma_{ij}, \sigma_{ijk}$	antiferroelectric dielectric stiffnesses at constant stress
μ_{ij}	coupling between the ferroelectric and antiferroelectric polarizations
β_i, β_{ij}	octahedral torsion coefficients
γ_{ij}	coupling between the ferroelectric polarization and tilt angle
s_{ij}	elastic compliances at constant polarization
Q_{ij}	electrostrictive coupling between the ferroelectric polarization and stress
Z_{ij}	electrostrictive coupling between the antiferroelectric polarization and stress
R_{ij}	rotostrictive coupling between the tilt angle and stress
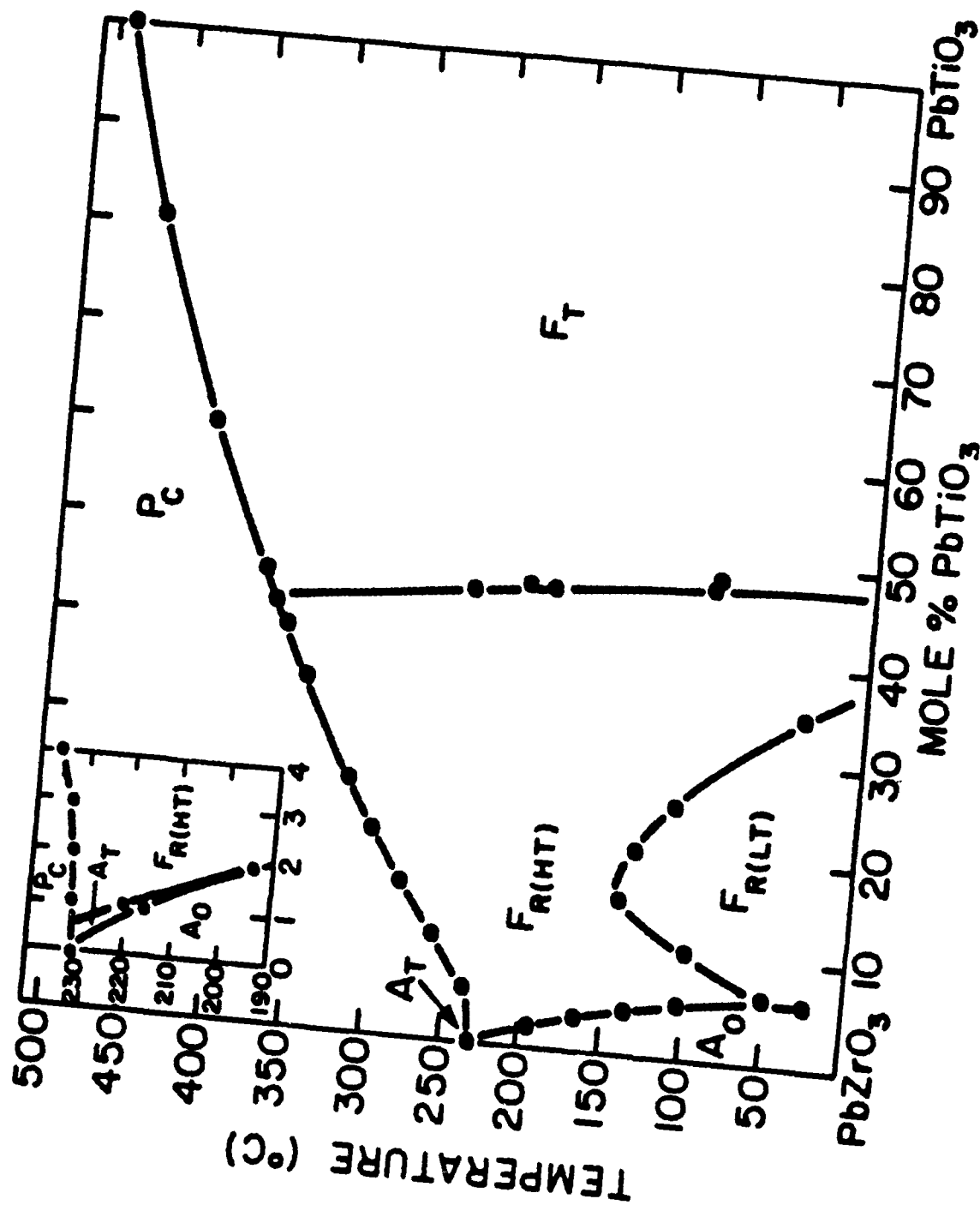
Fig. 1

THERMODYNAMIC THEORY OF THE LEAD ZIRCONATE-TITANATE
SOLID SOLUTION SYSTEM. PART II: TRICRITICAL BEHAVIOR

M. J. Haun[†], E. Furman[††], H. A. McKinstry, and L. E. Cross

Materials Research Laboratory
The Pennsylvania State University
University Park, PA 16802

Two tricritical points, where a phase transition changes from first to second order, were found to occur in the lead zirconate-titanate (PZT) solid solution system. High-temperature x-ray diffraction data on sol-gel derived PZT powders were used to calculate the cell parameters and spontaneous strain in the ferroelectric phases. These data were used with addition data from the literature to determine values of the higher-order dielectric stiffness coefficients, which were then used to locate the tricritical points. The values of the coefficients are also needed in the development of a thermodynamic theory of the PZT system.

[†]Now at Du Pont Experimental Station, Electronics Dept., Bldg. 334, Wilmington, DE, 19898.

[††]Now at Allied-Signal Inc., Morristown, NJ, 07960 5.1

I. INTRODUCTION

Tricritical behavior, where a phase transition changes from first to second order, has been shown to occur in the lead zirconate-titanate (PZT) solid solution system.[1-4] The end members lead titanate (PbTiO$_3$) and lead zirconate (PbZrO$_3$) both have large first-order phase transitions from a paraelectric cubic phase at high temperatures to ferroelectric tetragonal and rhombohedral phases, respectively, at lower temperatures. By forming a solid solution between these first-order end members a second-order transition region develops in the middle of the phase diagram.[4]

The degree of first order behavior has been shown to decrease from lead zirconate to the PZT 94/6 (94% PZ and 6% PT) composition, where a tricritical point occurs and the transition changes to second order.[1,2] With increasing titanium content the second order transition region was found to extend from the tricritical point over to the PZT 88/12 composition.[2] Since lead titanate has a first order transition, a second tricritical point should occur between the PZT 88/12 and lead titanate compositions.

To provide additional data to locate the second tricritical point, pure homogeneous sol-gel derived powders were prepared for several PZT compositions.[5] The lattice parameters of these compositions were determined from high-temperature x-ray diffraction, and used to calculate the spontaneous strain.[6] By using these data to determine the higher order dielectric stiffness coefficients, the second-order transition region was found to extend over to the morphotropic boundary between the tetragonal and rhombohedral phases.[4]

In this paper additional data will be presented to show that the second tricritical point occurs in the tetragonal phase field. The compositional dependence of the higher-order dielectric stiffness coefficients will be determined from high-temperature x-ray diffraction data, and used to locate the tricritical points. Values of the dielectric stiffness coefficients are also needed in the development a thermodynamic theory to model the phase transitions and single-domain properties of the entire PZT system.[7-10]

In the next section experimental high-temperature x-ray diffraction data will be presented. This data will be used to calculate the spontaneous polarization for tetragonal and rhombohedral compositions in Sections III and IV, respectively. This polarization data will then be used to determine the higher-order dielectric stiffness coefficients, and to establish the location of the tricritical points. In Section V the morphotropic boundary will be used to complete the evaluation of these coefficients, followed by a summary of this paper in Section VI.

II. HIGH-TEMPERATURE X-RAY DIFFRACTION

High-temperature x-ray diffraction was used to determine the cell parameters of sol-gel derived lead titanate and PZT powders. The lead titanate data was previously presented in Reference 11, and used to develop a thermodynamic theory of lead titanate. X-ray data on PZT 90/10, 80/20, 70/30 and 60/40 were previously presented in Reference 6. In this section high-temperature x-ray diffraction data on sol-gel derived powder of PZT 32/68 will be presented. The sol-gel procedure used to prepare this powder was described in Reference 5. The x-ray diffractometer setup and data analysis procedure that were used were described in References 6 and 11.

The splitting of the 002/200 and 123/312/321 peaks for the PZT 32/68 composition are shown in Figure 1. These x-ray data were used to calculate the cell constants using the Cohen least-squares refinement method[12] as shown in Figure 2. The data in these figures indicate that the transition from cubic to tetragonal in the PZT 32/68 composition is either second order, or only slightly first order. This is more obvious when plotting the cell volume ($= a_T^2 c_T$) versus temperature as shown in Figure 3. A continuous change in the volume would indicate that the transition is second order. For comparison the large discontinuity in the volume at the first order transition in lead titanate is shown in Figure 3. Additional data will be presented later in this paper to show that the cubic to tetragonal

transition in PZT 32/68 is probably second order.

The spontaneous strains x_1 and x_3 can be calculated from the tetragonal cell constants a_T and c_T using the following relations:

$$x_1 = \frac{a_T - a_C'}{a_C'} \qquad\qquad x_3 = \frac{c_T - a_C'}{a_C'} \qquad\qquad (1)$$

a_C' is the cubic cell length ex-apolated into the tetragonal region.

Different procedures have been used to calculate the spontaneous strains, depending on the procedure used to determine a_C'. Haun et al.[11] extrapolated the cubic cell constant into the tetragonal region by assuming that the electrostrictive ratio Q_{11}/Q_{12} is independent of temperature, which is a fairly good assumption in PZT.[13] This ratio can be determined from the ratio of the spontaneous strains x_1 and x_3 from Equation (21) in Reference 7:

$$\frac{x_3}{x_1} = \frac{Q_{11}}{Q_{12}} \qquad\qquad (2)$$

If the Q_{11}/Q_{12} ratio is known, then a_C' can be determined by combining Equations (1) and (2):

$$a_C' = \frac{c_T - (Q_{11}/Q_{12}) a_T}{1 - Q_{11}/Q_{12}} \qquad\qquad (3)$$

By determining the Q_{11}/Q_{12} ratio, a_C' can be calculated and used with the cell constants to calculate the spontaneous strains. Haun et al.[11] used a procedure of extrapolating the cubic cell constant a_C data to below the transition to calculate the Q_{11}/Q_{12} ratio for $PbTiO_3$. Due to the second order transition behavior of the PZT 32/68 composition, this procedure was not posssible. However, the electrostrictive constants of PZT have been recently approximated from a combination of single-crystal and polycrystalline data.[13] A value of - 3.166 for the Q_{11}/Q_{12} ratio was determined for the PZT 32/68 composition.[13] This value was used in Equation (3) to calculate a_C' as shown by the data plotted in

Figure 2.

The spontaneous strains x_1 and x_3 were then calculated for the PZT 32/68 composition from the data in Figure 2 using Equation 1. The results are shown in Figure 4, along with the lead titanate strain data from Reference 11. The numerical values of this data are listed in Reference 14. These strain data will be used in the next section with the electrostrictive constants to calculate the spontaneous polarization, which will then be used to determine the higher-order dielectric stiffness coefficients.

III. TETRAGONAL COMPOSITIONS

All of the dielectric stiffness coefficients in the PZT energy function [Equation (1) in Reference 7] were assumed to be independent of temperature, except the dielectric stiffness constant α_1 which was given a linear temperature dependence based on the Curie-Weiss law:

$$\alpha_1 = \frac{T - T_0}{2\,\varepsilon_0\,C} \qquad (4)$$

C is the Curie constant, ε_0 is the permittivity of free space, and T_0 is the Curie-Weiss temperature. By finding values of T_0 and C, α_1 can be calculated as a function of temperature.

The simplest and usual method of finding values of T_0 and C is to fit the inverse of the dielectric constant in the paraelectric state using the Curie-Weiss law. Unfortunately, very little dielectric data on PZT in the high temperature cubic state exists, due to the lack of good quality single crystals. Measurements on polycrystalline ceramic samples typically give similar values of T_0 and C as from single crystals, but these measurements are difficult in pure PZT due to the large electrical conductivity at high temperatures. In addition, considerable discrepancies exist in the measurements that have been made. For these reasons indirect methods were used to determine T_0 and C. T_0 will be determined by fitting spontaneous strain data as described later in this section. C will be found from

low-temperature dielectric data the third paper of this series.[8]

The Curie constant acts as a scaling constant in the dielectric properties and energies of the phases. The dielectric stiffness coefficients are inversely proportional to the Curie constant, as shown by Equation (1) for α_1. However, the spontaneous polarization, strain, and tilt angle are all independent of the Curie constant. Since the Curie constant was not known at this point, new constants were formed by multiplying the dielectric stiffness coefficients by the Curie constant. These new constants can be determined from the spontaneous polarization data independent of the Curie constant. Equation (4) then becomes:

$$\alpha_1 C = \frac{T - T_0}{2\,\varepsilon_0} \tag{5}$$

Now if T_0 can be determined, then the new constant $\alpha_1 C$ can be calculated.

The spontaneous polarization of the tetragonal state can be related to the dielectric stiffness coefficients by solving the quadratic relation formed from the first partial derivative stability condition [Equation (14) in Reference 7]:

$$P_3^2 = \frac{-\alpha_{11} \pm [\alpha_{11}^2 - 3\,\alpha_1\alpha_{111}]^{1/2}}{3\,\alpha_{111}} \tag{6}$$

Only the + solution to the quadratic equation is considered here, because the + solution corresponds to a free energy minimum, while the - solution corresponds to a maximum of the free energy.

Multiplying the numerator and denominator of Equation (6) by the Curie constant results in the following relation which relates P_3 to the new $\alpha_1 C$, $\alpha_{11} C$, and $\alpha_{111} C$ constants:

$$P_3^2 = \frac{-\alpha_{11}C + [(\alpha_{11}C)^2 - 3\,\alpha_1 C\,\alpha_{111}C]^{1/2}}{3\,\alpha_{111}C} \tag{7}$$

If the cubic-tetragonal transition is second order then $T_0 = T_C$, and the following relation results from Equations (5) and (7):

$$P_3{}^2 = a \{1 - [1 - b(T - T_C)]^{1/2}\},$$

where $a = -\alpha_{11}C/(3\alpha_{111}C)$, and $b = 3\alpha_{111}C/[2\varepsilon_0(\alpha_{11}C)^2]$ \qquad (8)

The a and b relations can also be rearranged in terms of the $\alpha_{11}C$ and $\alpha_{111}C$ constants:

$$\alpha_{11}C = -1/(2\varepsilon_0 C a b) \qquad\qquad \alpha_{111}C = 1/(6\varepsilon_0 C a^2 b) \qquad (9)$$

Since $\alpha_{11}C$ and $\alpha_{111}C$ are assumed to be independent of temperature, a and b will also be independent of temperature. Equation (8) shows that for a second order transition the spontaneous polarization P_3 goes to zero at the transition temperature T_C.

The spontaneous strains x_1 and x_3 of the tetragonal state are related to P_3 through the electrostrictive coefficients [see Equation (21) in Reference 7]. By substituting Equation (8) into Equation (21) from Reference 7 the following relations result:

$$x_1 = a Q_{12} \{1 - [1 - b(T - T_C)]^{1/2}\} \qquad (10)$$
$$x_3 = a Q_{11} \{1 - [1 - b(T - T_C)]^{1/2}\} \qquad (11)$$

These equations can be used to fit the tetragonal strain data, if the cubic-tetragonal transition is second order.

If the cubic-tetragonal transition is first order, then $T_0 \neq T_C$, and the spontaneous polarization changes discontinuously at the transition. At T_C two relations must be satisfied:

$$0 = \alpha_{1C} + \alpha_{11} P_{3C}{}^2 + \alpha_{111} P_{3C}{}^4 \text{ , and} \qquad (12)$$
$$0 = \alpha_{1C} + 2\alpha_{11} P_{3C}{}^2 + 3\alpha_{111} P_{3C}{}^4 \text{ ,} \qquad (13)$$

where α_{1C} and P_{3C} are α_1 and P_3 at T_C. Equation (12) was derived from the requirement that the ΔG's of the cubic and tetragonal phases [Equations (8) and (9) in Reference 7] must

be equal at T_C. Equation (13) is the first partial derivative stability condition [Equation (14) in Reference 7] at T_C, which must be satisfied so that the stable state corresponds to the minima of the energy function.

From Equation (4) α_1 at T_C is:

$$\alpha_{1C} = \frac{T_C - T_0}{2 \, \varepsilon_0 \, C} \tag{14}$$

Substituting this equation into Equations (12) and (13), and solving for the temperature independent coefficients α_{11} and α_{111} results in:

$$\alpha_{11} = \frac{-(T_C - T_0)}{\varepsilon_0 \, C \, P_{3C}^2} \, , \qquad \alpha_{111} = \frac{T_C - T_0}{2 \, \varepsilon_0 \, C \, P_{3C}^4} \tag{15}$$

By multiplying these relations by the Curie constant C, equations result for the new constants $\alpha_{11}C$ and $\alpha_{111}C$:

$$\alpha_{11}C = \frac{-(T_C - T_0)}{\varepsilon_0 \, P_{3C}^2} \, , \qquad \alpha_{111}C = \frac{T_C - T_0}{2 \, \varepsilon_0 \, P_{3C}^4} \tag{16}$$

Substituting Equations (16) and (5) into Equation (7), or substituting Equations (15) and (4) into Equation (6), results in the following relation:

$$P_3^2 = \psi \, P_{3C}^2 \, , \qquad \text{where} \quad \psi = \frac{2}{3} \left\{ 1 + \left[1 - \frac{3 \, (T - T_0)}{4 \, (T_C - T_0)} \right]^{1/2} \right\} \tag{17}$$

This equation can be used to calculate the spontaneous polarization P_3 from P_{3C}, T_0, and $T_C - T_0$, when the paraelectric - ferroelectric transition is first order. Comparing this equation with the second order P_3 relation [Equation (8)] shows that a change in sign occurred after the first term. This is because for a first-order transition α_{11} is negative.

Similar relations can be derived for the spontaneous strains x_1 and x_3 by substituting Equation (17) into Equation (20) from Reference 7:

$$x_1 = \psi\, x_{1C}, \qquad \text{where} \quad x_{1C} = Q_{12}\, P_{3C}^2 \qquad\qquad (18)$$

$$x_3 = \psi\, x_{3C}, \qquad \text{where} \quad x_{3C} = Q_{11}\, P_{3C}^2 \qquad\qquad (19)$$

The above equations were used to fit the experimental tetragonal spontaneous strain data that was determined from high-temperature x-ray diffraction data. In each equation there are three independent unknown constants [x_{1C}, T_0, and $T_C - T_0$ in Equation (18); and x_{3C}, T_0, and $T_C - T_0$ in Equation (19)]. With three unknown constants many combinations of the values of these constants will give similar fits of the experimental data. For this reason a value of T_C was first determined from the experimental phase diagram, which reduced the number of unknown constants to two. With only two unknown constants, the combination of values that gave the best least squares fit of the data could be easily found.

Amin et al.[15] fit T_C of the experimental phase diagram with the following polynomial equation:

$$T_C = (211.8 + 486.0\,x - 280.0\,x^2 + 74.42\,x^3)\,°C, \qquad\qquad (20)$$

where x is the mole fraction $PbTiO_3$ in PZT. This equation will be used to calculate T_C versus composition for the evaluation of the dielectric stiffness constants in this section, but a new equation [Equation (42)] will be given in Section IV, which will be used to calculate T_C in References 8-10.

Haun et al.[11] used a computer program to determine values of x_{1C}, x_{3C}, and T_0 that gave the best least-squares fit of the lead titanate strain data (shown in Figure 4) using Equations (18) and (19) with T_C equal to 492.2°C [calculated from Equation (20)]. The electrostrictive constants of lead titanate were determined using Gavrilyachenko et als.[16] room temperature spontaneous polarization value of 0.75 C/m^2, and used with the strain data to calculate the spontaneous polarization, as shown in Figure 5. The values of all of the

constants used in these calculations are listed in Table I.

The same procedure was used to fit the PZT 32/68 spontaneous strain data from Figure 4. However, for this composition the least-squares error continually became smaller as the T_C - T_0 difference was reduced, indicating that the transition was actually second order. Therefore, Equations (10) and (11) were used to fit this data. Values of the constants aQ_{11}, aQ_{12}, and b were then found that gave the best fit of the strain data. The spontaneous polarization was calculated by combining the strain data with the electrostrictive constants from Reference 13. The experimental polarization data and theoretical fit of the data are shown in Figure 5. The values of the constants used in these calculations are listed in Table I.

IV. RHOMBOHEDRAL COMPOSITIONS

The spontaneous polarization of the high-temperature rhombohedral state can be solved from the quadratic first partial derivative stability condition [Equation (16) in Reference 7]:

$$P_3{}^2 = \frac{-\zeta + [\zeta^2 - 9\,\alpha_1\,\xi]^{1/2}}{3\,\xi}, \tag{21}$$

where $\quad \zeta = 3\,(\alpha_{11} + \alpha_{12}),\qquad$ and $\quad \xi = 3\,\alpha_{111} + 6\,\alpha_{112} + \alpha_{123} \qquad$ (22)

As in the tetragonal case the numerator and denominator of this equation were multiplied by the Curie constant C to relate P_3 to the new constants:

$$P_3{}^2 = \frac{-\zeta C + [(\zeta C)^2 - 9\,\alpha_1 C\,\xi C]^{1/2}}{3\,\xi C}, \tag{23}$$

where $\quad \zeta C = 3\,(\alpha_{11}C + \alpha_{12}C\,),\quad$ and $\quad \xi C = 3\,\alpha_{111}C + 6\,\alpha_{112}C + \alpha_{123}C \qquad$ (24)

If the cubic-rhombohedral transition is second order then $T_0 = T_C$, and the following relation results from Equations (5) and (23):

$$P_3{}^2 = a \{1 - [1 - b(T - T_C)]^{1/2}\},$$

where $a = -\zeta C /(3 \xi C)$, and $b = 9 \xi C /[2 \varepsilon_0 (\zeta C)^2]$ (25)

The a and b relations can also be rearranged in terms of ζC and ξC:

$$\zeta C = - 3/(2 \varepsilon_0 C a b) \qquad \xi C = 1/(2 \varepsilon_0 C a^2 b) \qquad (26)$$

A similar relation can be found for the spontaneous strain x_4 by substituting Equation (23) into Equation (24):

$$x_4 = a Q_{44} \{1 - [1 - b(T - T_C)]^{1/2}\} \qquad (27)$$

As in the tetragonal case at T_C, if the cubic-rhombohedral transition is first order, then a different procedure must be used to evaluate the coefficients. At T_C the energies of the cubic and rhombohedral phases must be equal [Equations (8) and (10) in Reference 7], and the first partial derivative stability condition [Equation (16) in Reference 7] must be satisfied:

$$0 = 3 \alpha_{1C} + \zeta P_{3C}{}^2 + \xi P_{3C}{}^4 \text{, and} \qquad (28)$$
$$0 = \alpha_{1C} + 2/3 \zeta P_{3C}{}^2 + \xi P_{3C}{}^4 \text{,} \qquad (29)$$

where α_{1C} and P_{3C} are α_1 and P_3 at T_C.

Substituting Equation (14) into Equations (28) and (29) and solving for the temperature independent coefficients ζ and ξ results in:

$$\zeta = \frac{- 3 (T_C - T_0)}{\varepsilon_0 C P_{3C}{}^2} \text{,} \qquad \xi = \frac{3 (T_C - T_0)}{2 \varepsilon_0 C P_{3C}{}^4} \qquad (30)$$

By multiplying these relations by the Curie constant C, equations result for the new constants ζC and ξC:

$$\zeta C = \frac{-3\,(T_C - T_0)}{\varepsilon_0\,P_{3C}{}^2}\,, \qquad \xi C = \frac{3\,(T_C - T_0)}{2\,\varepsilon_0\,P_{3C}{}^4} \qquad (31)$$

Substituting Equations (31) and (5) into Equation (7) or substituting Equations (30) and (4) into Equation (6) results in the following relation:

$$P_3{}^2 = \psi\,P_{3C}{}^2\,, \qquad \text{where} \quad \psi = \frac{2}{3}\left\{\, 1 + \left[\, 1 - \frac{3\,(T - T_0)}{4\,(T_C - T_0)} \,\right]^{1/2} \,\right\} \qquad (32)$$

This equation is the same as Equation (17) derived for the spontaneous polarization of the tetragonal state, except that P_3 and P_{3C} in this case refer to the rhombohedral phase.

A similar relation can be derived for the spontaneous strain x_4 by substituting Equation (32) into Equation (26):

$$x_4 = \psi\,x_{4C}\,, \qquad \text{where} \quad x_{4C} = Q_{44}\,P_{3C}{}^2 \qquad (33)$$

Either Equation (27) or (33) was used to fit the experimental high-temperature rhombohedral spontaneous strain data from Reference 6. The transition temperature T_C was first determined from the fit of the experimental phase diagram [Equation (20)], and then values of the remaining two unknown constants were found that gave the best least-squares fit of the data. The best fit of the PZT 90/10 data was found to be slightly first order, while the best fits of the PZT 80/20, 70/30, and 60/40 compositions were second order. The stain data was then used to calculate the spontaneous polarization through the electrostrictive constants from Reference 13, as shown in Figure 6. The values of the constants used in the calculations are listed in Table II.

V. FITTING THE MORPHOTROPIC PHASE BOUNDARY

In the last two sections constants involving the product of the Curie constant and the fourth and sixth order tetragonal ($\alpha_{11}C$ and $\alpha_{111}C$) and rhombohedral (ζC and ξC) dielectric stiffness constants were determined from spontaneous strain and electrostrictive data. $\alpha_{11}C$ and $\alpha_{111}C$ were determined for PbTiO$_3$ and PZT 32/68, and ζC and ξC for PZT 90/10, 80/20, 70/30, and 60/40. In addition to these data, values of ζC and ξC were calculated for PbZrO$_3$[17]. A value of ζC was also determined for PbTiO$_3$[11].

From the above data the compositional dependences could be estimated for ζC from PbZrO$_3$ to PbTiO$_3$, for ξC only across the rhombohedral phase field, and for $\alpha_{11}C$ and $\alpha_{111}C$ only across the tetragonal phase field. Additional data were therefore needed to determine the compositional dependence of all of these constants across the entire PZT system.

The ζC [$= 3 (\alpha_{11}+ \alpha_{12}) C$] data was plotted in Figure 7 (c) versus composition. This data was fit with the following equation:

$$\zeta C = [(a + bx)\, exp^{-cx} + dx + e]\, 10^{14} , \qquad (34)$$

where a = - 9.6, b = -0.012501, c = 12.6, d = 0.42743, e = 2.6213, exp is the exponential function, and x is the mole fraction of PbTiO$_3$ in PZT. This equation was then used to calculate ζC versus composition.

The rhombohedral sixth-order dielectric stiffness (ξ) cannot become negative when the rhombohedral phase is metastable, and the stable tetragonal phase undergoes a second-order transition to the cubic state. The ξC [$= 3 \alpha_{111}+ 6 \alpha_{112} + \alpha_{123}) C$] data from the last section showed that this constant does decrease across the rhombohedral phase field towards the lead titanate composition, and may level off without becoming negative. To keep this constant from becoming negative, ξC was assumed to be equal to $\alpha_{111}C$ at the lead titanate composition. This is the same as assuming that $\alpha_{123}C$ is equal to six times $\alpha_{112}C$ for PbTiO$_3$. This data point was plotted in Figure 8 (d) along with the rest of the ξC

data, which was then fit with the following equation:

$$\xi C = [(a + bx) \exp^{-cx} + dx + e] \, 10^{14} , \tag{35}$$

where a = 16.225, b = - 0.088651, c = 21.255, d = - 0.76973, e = 0.887, and x is the mole fraction of PbTiO$_3$ in PZT. This equation was then used to calculate ξC versus composition.

The morphotropic phase boundary, where the energies of the tetragonal and high-temperature rhombohedral phases must be equal, was used to extrapolate the $\alpha_{11}C$ and $\alpha_{111}C$ constants into the rhombohedral phase field. The energies of the tetragonal and high-temperature rhombohedral phases were defined by Equations (9) and (11) in Reference 7. Multiplying these equations by the Curie constant results in the following relations:

$$F_T \qquad \Delta G\, C = \alpha_1 C\, P_3^2 + \alpha_{11} C\, P_3^4 + \alpha_{111} C\, P_3^6 \tag{36}$$
$$F_{R(HT)} \qquad \Delta G\, C = 3\, \alpha_1 C\, P_3^2 + \zeta\, C\, P_3^4 + \xi\, C\, P_3^6 \tag{37}$$

Since the Curie constant is the same for the tetragonal and rhombohedral phases, the product of ΔG and C for these two phases should be equal at the morphotropic boundary.

From the data presented in the last two sections, the paraelectric-ferroelectric transition appears to be second order on both sides of the morphotropic boundary, and thus $T_0 = T_C$. The relation for T_C [Equation (20)] was therefore used to calculate T_0, which is needed to determine $\alpha_1 C$ versus composition [see Equation (5)]. Using this procedure to calculate $\alpha_1 C$ with ζC and ξC determined from Equations (34) and (35), the product of the energy ΔG and the Curie constant for the rhombohedral state could be calculated using Equation (37).

A computer program was written to extrapolate the $\alpha_{11}C$ and $\alpha_{111}C$ constants into the rhombohedral phase field by fitting the morphotropic boundary. The first step was to make initial guesses for the values of $\alpha_{11}C$ and $\alpha_{111}C$ for PbZrO$_3$. A quadratic fit of this data and the values of $\alpha_{11}C$ and $\alpha_{111}C$ determined in Section III for the PZT 32/68 and

$PbTiO_3$ compositions were then made using the following equation:

$$\alpha_{11}C \text{ or } \alpha_{111}C = (a + b\,x + c\,x^2)\,10^{13} \qquad (38)$$

The product of the energy ΔG and the Curie constant of the tetragonal state could now be calculated using Equation (36). The morphotropic boundary was then calculated from the cross over of the $\Delta G\,C$ products of the two phases, and a least-squares error with the experimental data was calculated. New values of $\alpha_{11}C$ and $\alpha_{111}C$ for $PbZrO_3$ were chosen, and the procedure repeated until the best least-squares fit of the morphotropic boundary was obtained. The final fit is shown in Figure 2 of Reference 10 by the solid curve. The values and final fittings of the $\alpha_{11}C$ and $\alpha_{111}C$ constants are plotted in Figures 7 and 8. In Equation (38) the final constants for $\alpha_{11}C$ were a = 10.612, b = -22.655, and c = 10.955; and for $\alpha_{111}C$ were a = 12.026, b = -17.296, and c = 9.1790.

This program visually demonstrated how the shape of the morphotropic boundary could be changed by varying the dielectric *stiffness coefficients*. Depending on the values of the coefficients chosen, the phase boundary could be shifted either towards $PbZrO_3$ or $PbTiO_3$, and the shape could be changed from vertical to curved. The bending of the boundary could also be made to go towards $PbZrO_3$ or $PbTiO_3$.

The $\alpha_{12}C$ constant can be calculated from the $\alpha_{11}C$ and ζC [$= 3\,(\alpha_{11} + \alpha_{12})\,C$] constants:

$$\alpha_{12}C = \zeta C / 3 - \alpha_{11}C \qquad (39)$$

Using this relation and Equations (34) and (38) for ζC and $\alpha_{11}C$, $\alpha_{12}C$ was calculated versus composition as shown in Figure 7.

When $\alpha_{11}C$ or ζC change sign tricritical points occur, and the cubic-tetragonal or cubic-rhombohedral transition changes from first to second order. As shown in Figure 7 tricritical points (labeled TCP) occur at the $Pb(Zr_{1-x}Ti_x)O_3$ compositions with values of x equal to 0.102 and 0.717. Between these tricritical points the paraelectric-ferroelectric

transition is second order, and first order regions exist near the end members $PbZrO_3$ and $PbTiO_3$. In the first order regions the $T_C - T_0$ difference and spontaneous polarization at T_C (P_{3C}) can be calculated from the following relations derived from Equations (16) and (31):

$$F_T \qquad P_{3C} = [-\alpha_{11}C / (2\,\alpha_{12}C)]^{1/2}, \qquad T_C - T_0 = \varepsilon_0\,(\alpha_{11}C)^2 / (2\,\alpha_{12}C) \qquad (40)$$

$$F_{R(HT)} \qquad P_{3C} = [-\zeta C / (2\,\xi C)]^{1/2}, \qquad T_C - T_0 = \varepsilon_0\,(\zeta C)^2 / (6\,\xi C) \qquad (41)$$

Using Equations (34), (35), and (38) to calculate the constants in these equations, P_{3C} and $T_C - T_0$ were calculated as shown in Figure 9.

T_C data from the experimental phase diagram were used with the above $T_C - T_0$ calculations to determine T_0 data in the first-order regions. These data were then combined with the T_C data from the second-order region, which is equal to T_0, and fit with the following polynomial equation:

$$T_0 = a + b\,x^2 + c\,x^3 + d\,x^4 + e\,x^5 + f\,x^6, \qquad (42)$$

where a = 189.48, b = 843.40, c = - 2105.5, d = 4041.8, e = - 3828.3, f = 1337.8, and x is the mole fraction of $PbTiO_3$ in PZT.

T_C was then calculated from the following relation:

$$T_C = (T_C - T_0) + T_0, \qquad (43)$$

where T_0 and $T_C - T_0$ were calculated from Equations (40) - (42). T_C was calculated from this equation and plotted in in Figure 2 of Reference 10 along with the experimental data. Equation (42) and (43) were used to calculate T_0 and T_C throughout the rest of this series of papers.

VI. SUMMARY

High-temperature x-ray diffraction data on sol-gel derived PZT 32/68 powder was presented, and used with electrostrictive data to calculate the spontaneous polarization. These data were used with previously published data to determine the values of the higher-order dielectric stiffness coefficients at several different compositions. The compositional dependence of each coefficient was determined by fitting these values with an equation. A set of equations was then established that can be used to calculate values of the coefficients at any composition.

All of the coefficients were assumed to be independent of temperature, except the dielectric stiffness coefficient α_1, which was given a linear temperature dependence based on the Curie-Weiss law. The experimental phase diagram was extensively used in the evaluation of the coefficients, by requiring that the energies of the adjacent phases of a phase transition to be equal at the transition. The first partial derivative stability conditions were also used as additional relations in the evaluation procedure.

The fourth-order tetragonal (α_{11}) and rhombohedral ($\alpha_{11} + \alpha_{12}$) dielectric stiffness coefficients were found to change sign as a function of composition, indicating that two tricritical points occur in the PZT system, where the paraelectric-ferroelectric phase transition changes from first to second order. By extrapolating between the data points, the tricritical points were found to occur at $Pb(Zr_{1-x}Ti_x)O_3$ compositions with x equal to 0.102 and 0.717. The transition was first order from the end members to the tricritical points, and then a large second order region occurs across the phase diagram between the tricritical points.

The tricritical point on the lead zirconate side of the phase diagram was previously found to occur at the PZT 94/6 composition,[2] four percent closer to lead zirconate than where the data in this study indicates that it should occur. This difference may simply be due to the experimental error involved in the measurements and theoretical fitting, or may be related to differences in homogeneity of the powders used (mixed-oxide versus sol-gel).

Haun et al.[4] indicated that the second tricritical point occurred near or possibly at the morphotropic boundary. With the more recent data presented in this paper and a more careful analysis of the previous data, the second tricritical point appears to be located at the PZT 28/72 composition as described above. Differential Scanning Calorimetric (DSC) data on the sol-gel powders prepared in this project also indicated that the second tricritical point occurs near the PZT 28/72 composition. The shape of the DSC peaks at T_C changed from sharp narrow peaks (first order) to very broad peaks (second order) at this composition. Additional work on preparing homogeneous PZT powders, and then determining the lattice constants as a function of temperature from high-temperature x-ray diffraction is needed to locate the tricritical points more precisely.

REFERENCES

[1] R. Clarke and A. M. Glazer, Ferroelectrics, 14, 695 (1976).

[2] R. W. Whatmore, R. W., R. Clarke, and A. M. Glazer, J. Phys. C: Solid State Phys., 11, 3089 (1978).

[3] K. Roleder and J. Handerek, Phase Transitions, 2, 285 (1982).

[4] M. J. Haun, Z. Q. Zhuang, S. J. Jang, H. A. McKinstry, and L. E. Cross, *Proceedings of the 6th IEEE International Symposium on the Applications of Ferroelectrics*, Lehigh, PA, edited by Van Wood (IEEE, New York, 1986) pp. 398-401.

[5] Z. Q. Zhuang, M. J. Haun, S. J. Jang, and L. E. Cross, *Proceedings of the 6th IEEE International Symposium on the Applications of Ferroelectrics*, Lehigh, PA, edited by Van Wood (IEEE, New York, 1986) pp. 394-397.

[6] M. J. Haun, Y. H. Lee, H. A. McKinstry, and L. E. Cross, *Advances in X-ray Analysis, Vol. 30*, edited by C. S. Barrett, J. V. Gilfrich, R. Jenkins, D. E. Leyden, J. C. Russ, and P. K. Predecki, (Plenum Press, New York, 1987) pp. 473-481.

[7] M. J. Haun, E. Furman, S. J. Jang, and L. E. Cross, "Thermodynamic Theory of the Lead Zirconate-Titanate Solid Solution System, Part I: Phenomenology," J. Appl. Phys. (submitted).

[8] M. J. Haun, Z. Q. Zhuang, E. Furman, S. J. Jang, and L. E. Cross, "Thermodynamic Theory of the Lead Zirconate-Titanate Solid Solution System, Part III: Curie Constant and Sixth-Order Polarization Interaction Dielectric Stiffness Coefficients," J. Appl. Phys. (submitted).

[9] M. J. Haun, E. Furman, T. R. Halemane, and L. E. Cross, "Thermodynamic Theory of the Lead Zirconate-Titanate Solid Solution System, Part IV: Tilting of the Oxygen Octahedra," J. Appl. Phys. (submitted).

[10]M. J. Haun, E. Furman, S. J. Jang, and L. E. Cross, "Thermodynamic Theory of the Lead Zirconate-Titanate Solid Solution System, Part V: Theoretical Calculations," J. Appl. Phys. (submitted).

[11]M. J. Haun, E. Furman, S. J. Jang, H. A. McKinstry, and L. E. Cross, J. Appl. Phys., 62, 333 (1987).

[12]B. Cullity, *Elements of X-ray Diffraction Second Edition* (Addison-Wesley, Reading, MA, 1978), pp. 350-368.

[13]M. J. Haun, Z. Q. Zhuang, E. Furman, S. J. Jang, and L. E. Cross, J. Am. Ceram. Soc. (submitted).

[14]M. J. Haun, *Thermodynamic Theory of the Lead Zirconate-titanate Solid Solution System*, Ph.D. thesis in Solid State Science, The Pennsylvania State University (1988).

[15]A. Amin, M. J. Haun, B. Badger, H. A. McKinstry, and L. E. Cross, Ferroelectrics, 65, 107 (1985).

[16]V. G. Gavrilyachenko, R. I. Spinko, M. A. Martynenko, and E. G. Fesenko, Fiz. Tverd. Tela 12, 1532 (1970) [Sov. Phys.-Solid State 12, 1203 (1970)].

[17]M. J. Haun, T. J. Harvin, M. T. Lanagan, Z. Q. Zhuang, S. J. Jang, and L. E. Cross, J. Appl. Phys. (to be submitted).

LIST OF FIGURES AND TABLES

Figure 9. The spontaneous polarization at T_C (P_{3C}) [(a) and (b)] and the T_C - T_0 difference [(c) and (d)] plotted versus composition in the first order regions of the phase diagram.

Table I. Constants used to Fit the Spontaneous Strain Data and to Calculate the Spontaneous Polarization Data for the Tetragonal Compositions.

Table II. Constants used to Fit the Spontaneous Strain Data and to Calculate the Spontaneous Polarization Data for the Rhombohedral Compositions

Table I. Constants used to Fit the Spontaneous Strain Data and to Calculate the

Spontaneous Polarization Data for the Tetragonal Compositions.

	PbTiO$_3$
T_C (°C)	492.2
T_0 (°C)	478.8
$T_C - T_0$ (°C)	13.4
x_{1C} (10^{-2})	- 0.362
x_{3C} (10^{-2})	1.24
Q_{11} (10^{-2} m^4/C^2)	8.9
Q_{12} (10^{-2} m^4/C^2)	- 2.6
P_{3C} (C/m^2)	0.373
$\alpha_{11}C$ (10^{12} m^5 °C/C^{2}F)	- 10.878
$\alpha_{111}C$ (10^{13} m^9 °C/C^{4}F)	3.909

	PZT 32/68
$T_C = T_0$ (°C)	436.2
a Q_{11}	-15.496
a Q_{12}	4.8904
b (°C^{-1})	1.0307
Q_{11} (10^{-2} m^4/C^2)	7.70
Q_{12} (10^{-2} m^4/C^2)	- 2.43
a (10^{-2} C^2/m^4)	- 2.0125
$\alpha_{11}C$ (10^{12} m^5 °C/C^{2}F)	2.7224
$\alpha_{111}C$ (10^{13} m^9 °C/C^{4}F)	4.5091

Table II. Constants used to Fit the Spontaneous Strain Data and to Calculate the Spontaneous Polarization Data for the Rhombohedral Compositions

	PZT 90/10
T_C (°C)	257.674
T_0 (°C)	257.655
$T_C - T_0$ (°C)	0.019
x_{4C} (10^{-5})	3.5328
Q_{44} (10^{-2} m^4/C^2)	4.9
P_{3C} (C/m^2)	0.0329
ζC (10^{14} m^5 °C/C^{2}F)	- 0.059390
ξC (10^{15} m^9 °C/C^{4}F)	2.7458

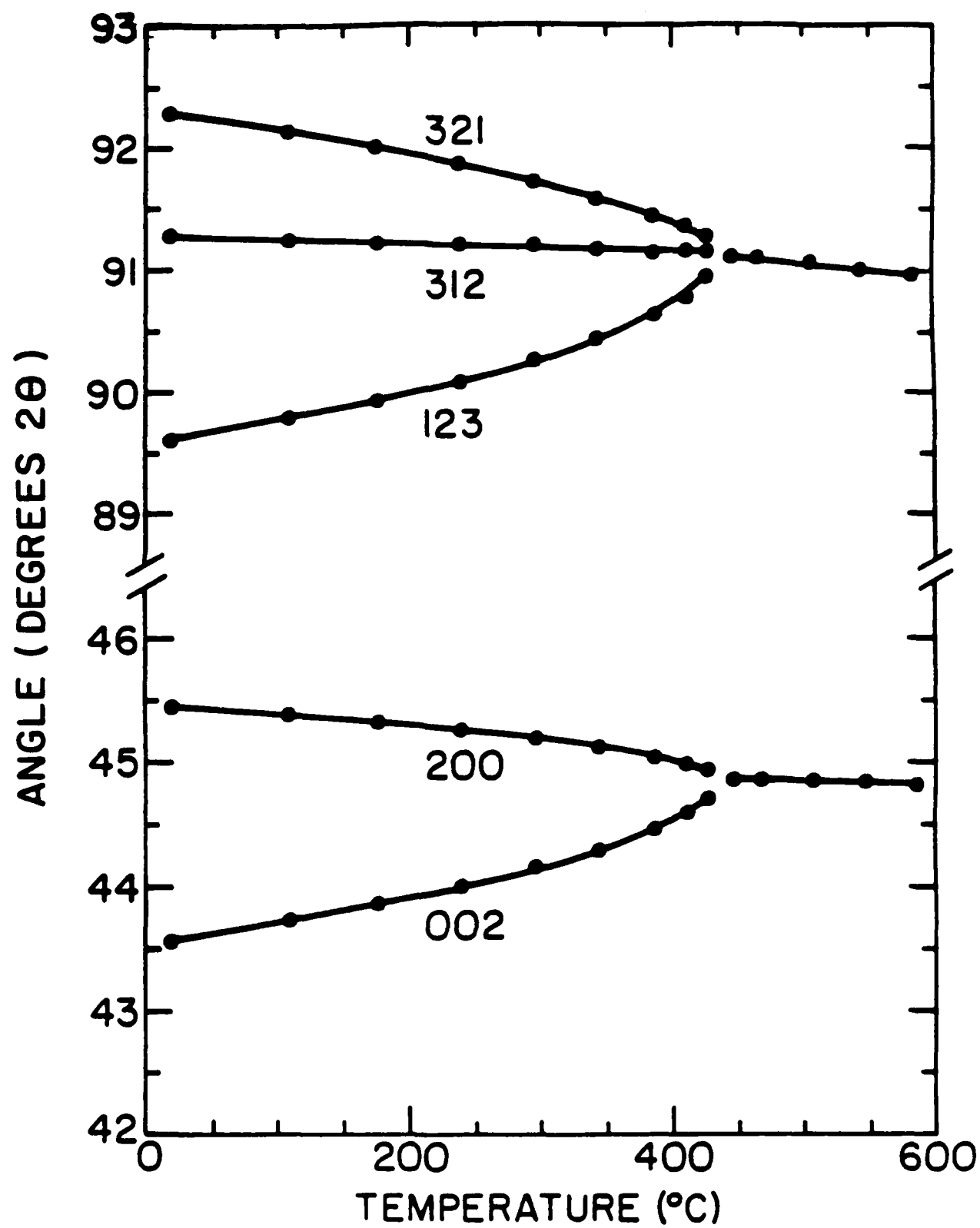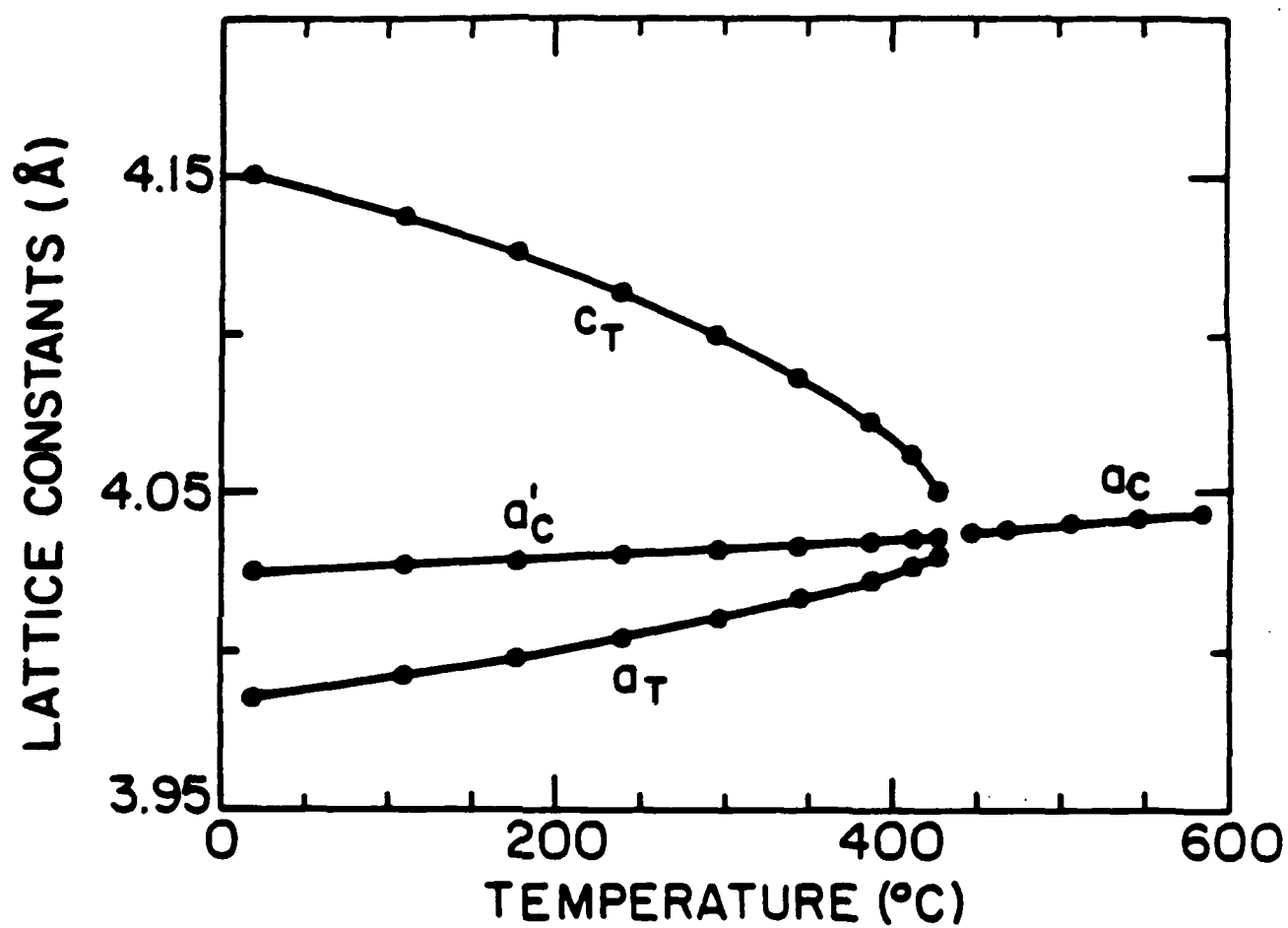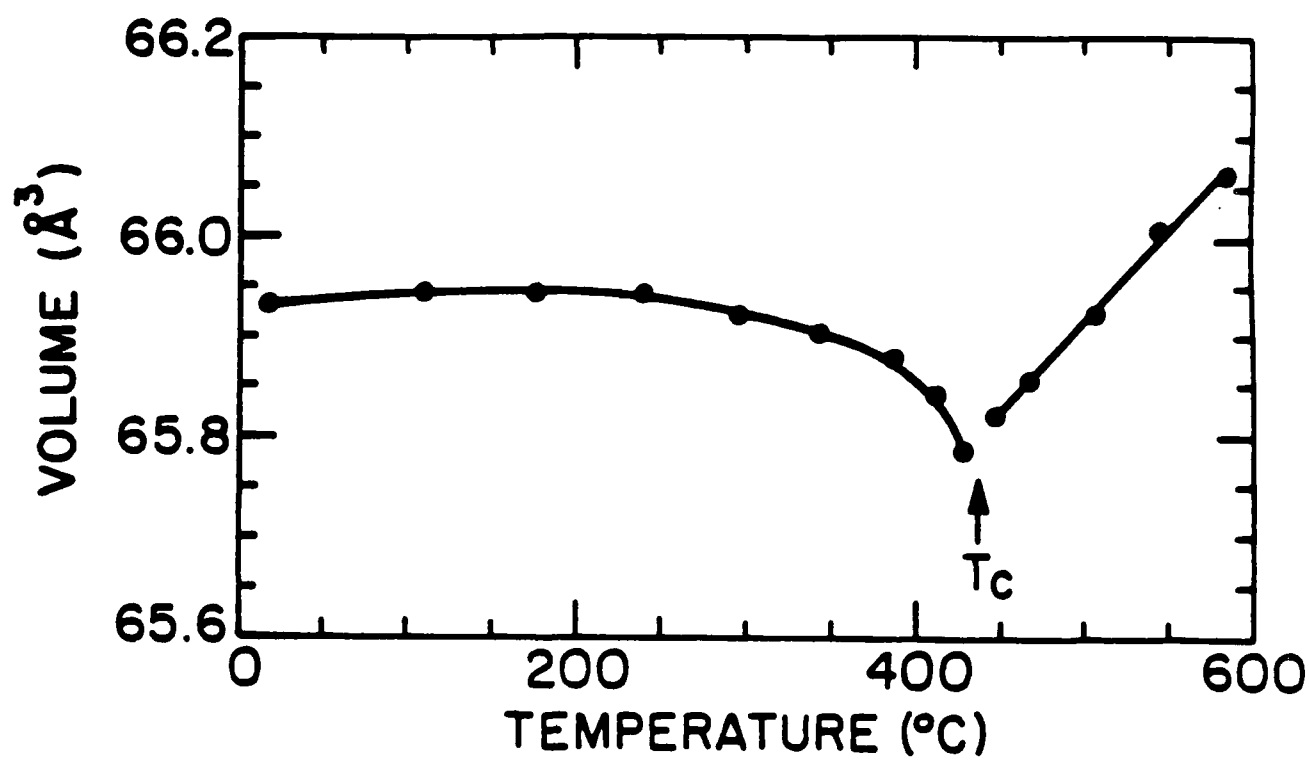|	PZT 80/20	PZT 70/30	PZT 6040
$T_C = T_0$ (°C)	298.40	334.41	366.16
$a\,Q_{44}$ (10^{-3})	- 2.2600	-1.7487	-5.4780
b (10^{-2} °C^{-1})	2.2808	2.8542	0.55338
Q_{44} (10^{-2} m^4/C^2)	5.17	5.52	6.29
a (10^{-2} C^2/m^4)	- 4.3713	-3.1679	-8.7091
ζC (10^{14} m^5 °C/C^{2}F)	1.6992	1.8737	1.9715
ξC (10^{15} m^9 °C/C^{4}F)	3.5153	3.5153	1.3454

Fig. 1

Fig. 2

Fig. 3

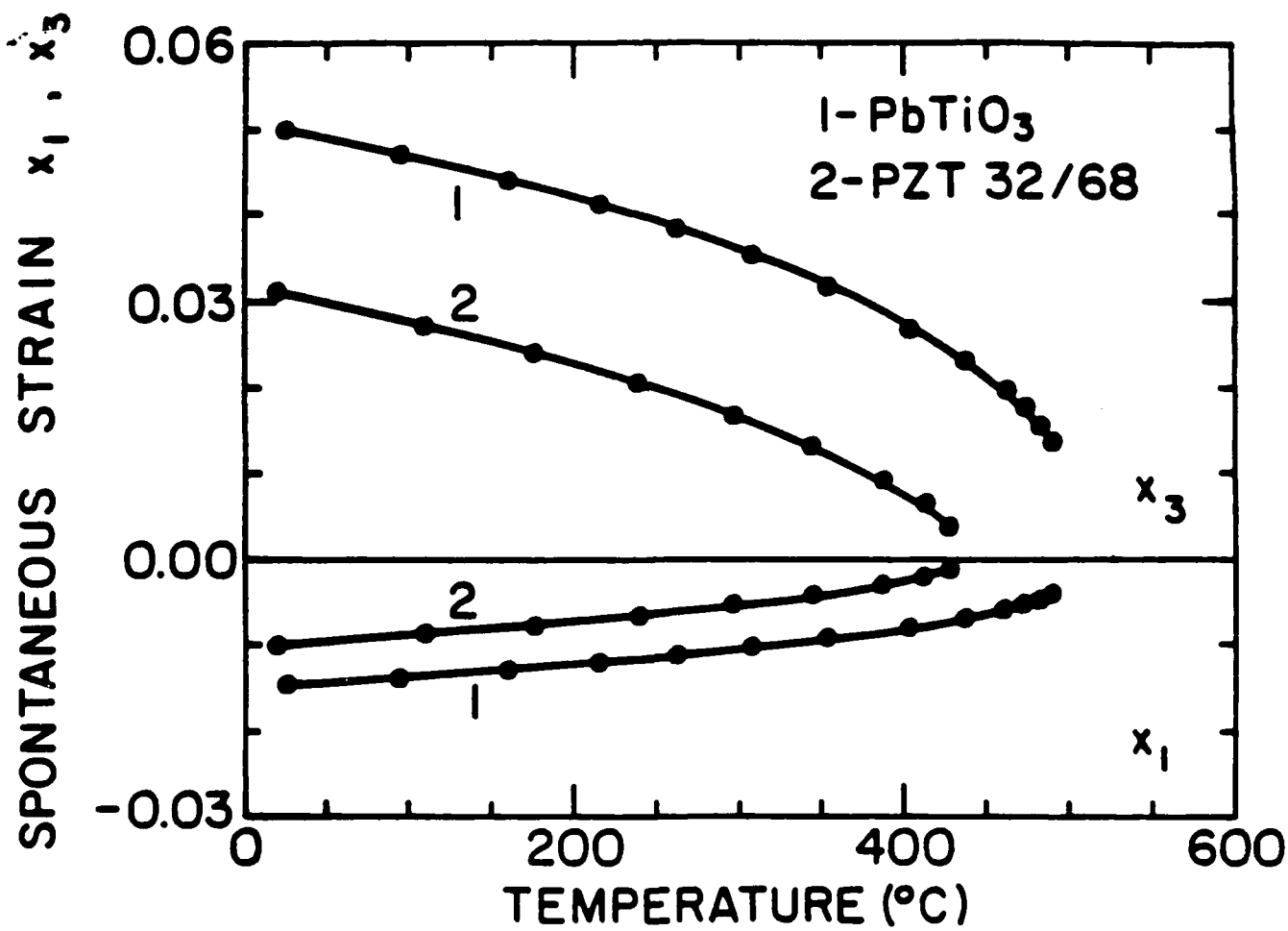Fig. 4
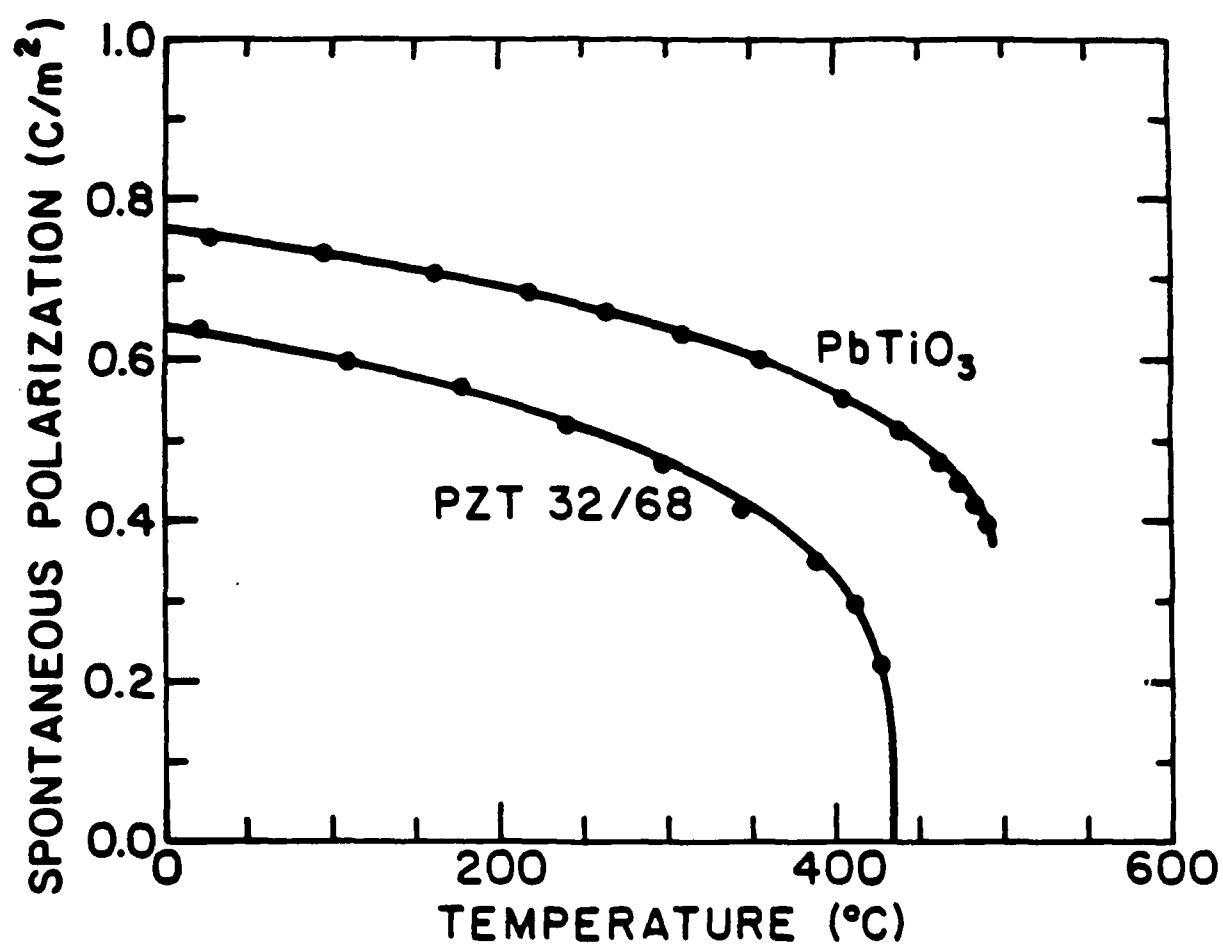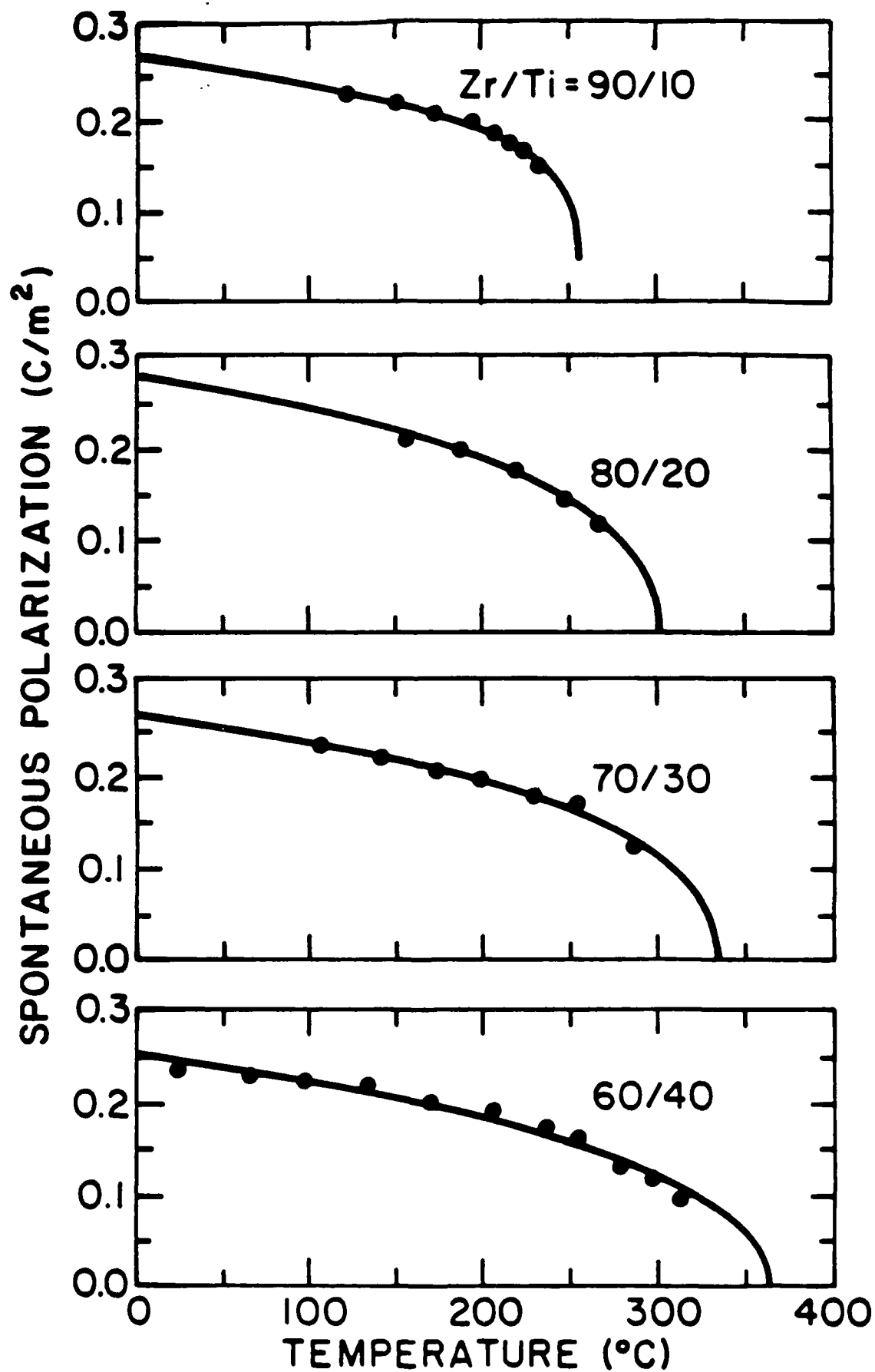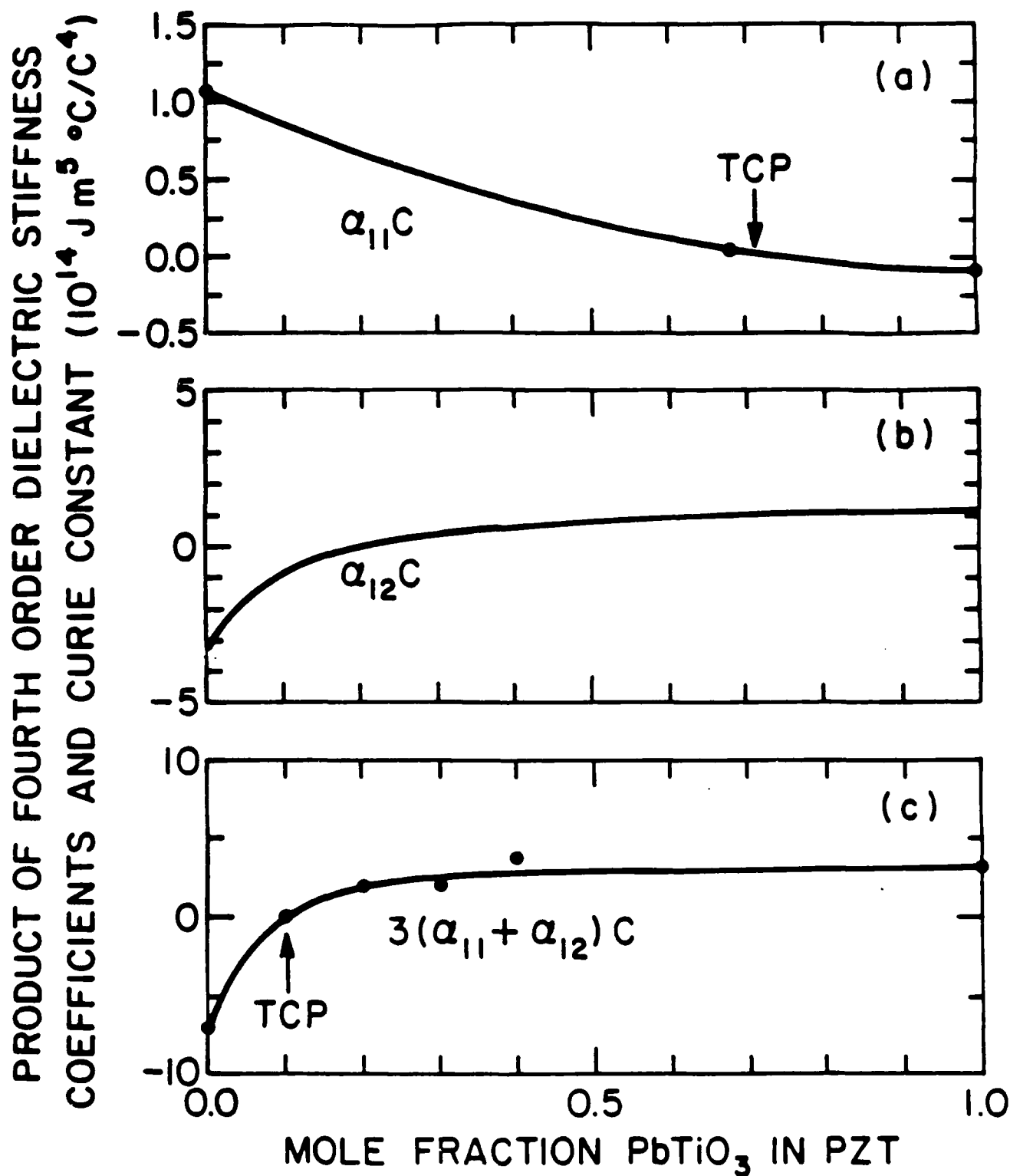
Fig. 5

Fig. 6

Fig. 7

Fig. 8
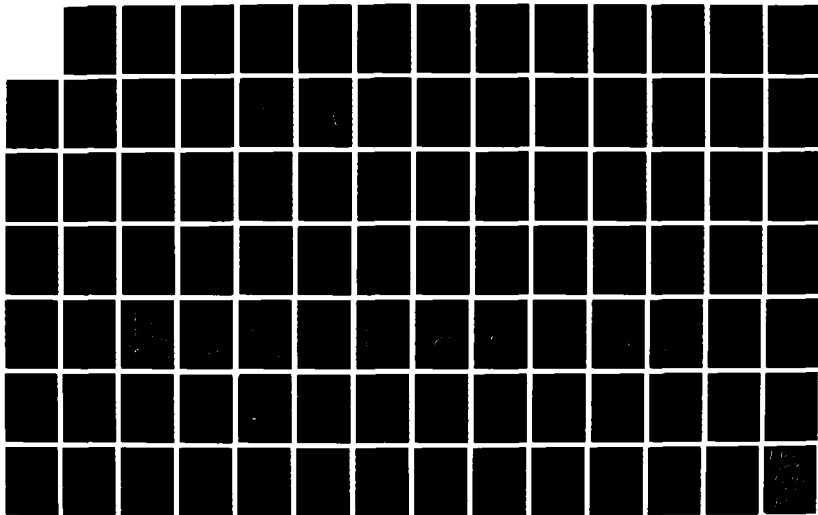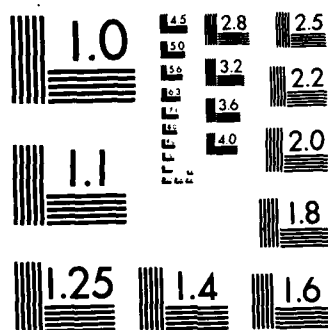
MICROCOPY RESOLUTION TEST CHART

NATIONAL BUREAU OF STANDARDS-1963-A

Fig. 9

THERMODYNAMIC THEORY OF THE LEAD ZIRCONATE-TITANATE SOLID SOLUTION SYSTEM, PART III: CURIE CONSTANT AND SIXTH-ORDER POLARIZATION INTERACTION DIELECTRIC STIFFNESS COEFFICIENTS

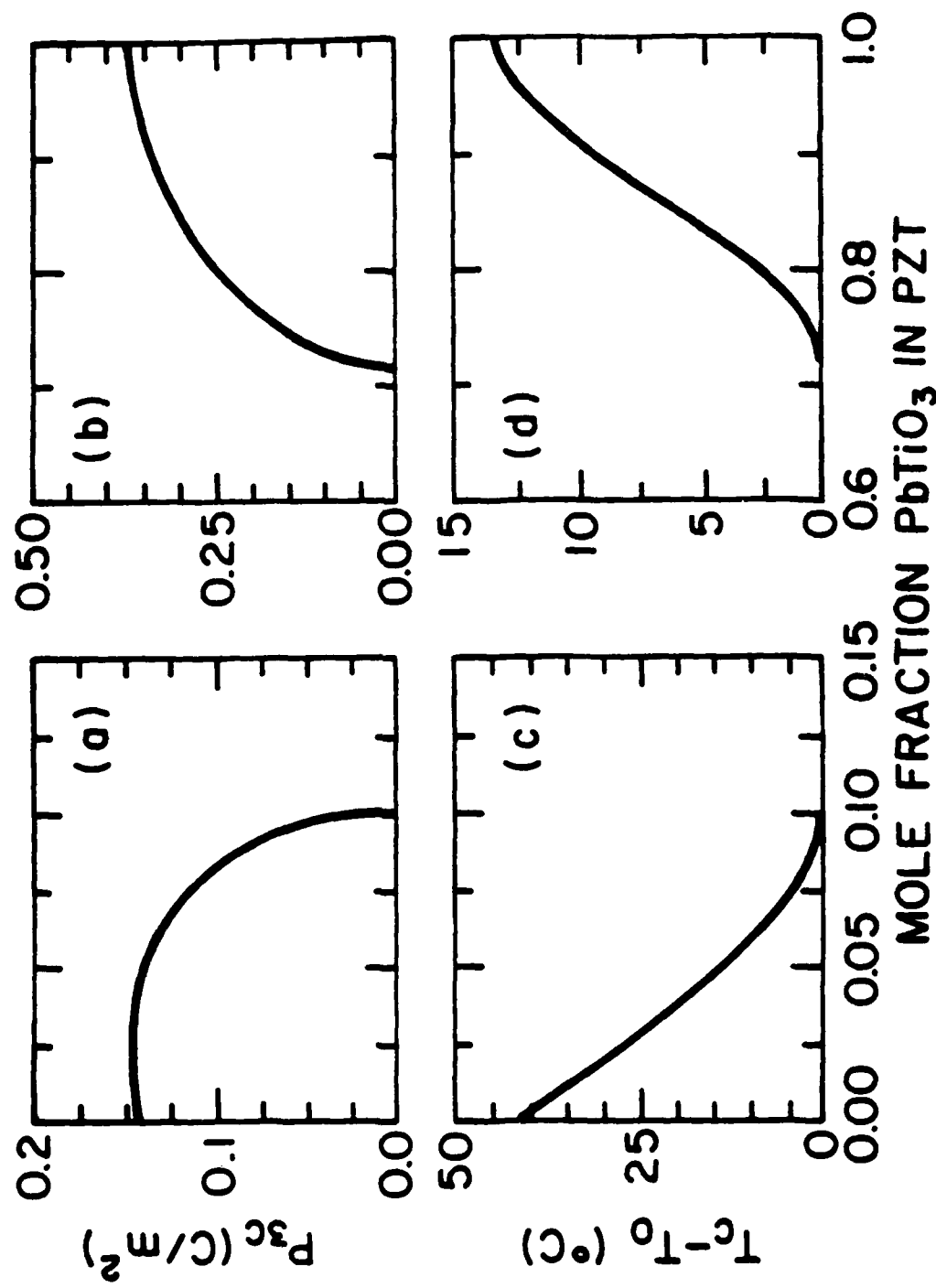M. J. Haun[†], Z. Q. Zhuang[††], E. Furman[†††], S. J. Jang, and L. E. Cross

Materials Research Laboratory
The Pennsylvania State University
University Park, PA 16802

Values of the Curie constant (C) and sixth-order polarization interaction dielectric stiffness coefficients (α_{112} and α_{123}) are needed for the development of a thermodynamic theory for the entire lead zirconate-titanate (PZT) solid solution system. Low-temperature dielectric data measured on pure homogeneous polycrystalline PZT samples were used to determine values of these coefficients at several compositions across the phase diagram. Equations were then fit to this data to determine the compositional dependence of the coefficients. The Curie constant was found to form a peak in the middle of the phase diagram at the PZT 50/50 composition.

[†]Now at Du Pont Experimental Station, Electronics Dept., Bldg. 334, Wilmington. DE, 19898.

[††]Visiting Scientist from the Department of Inorganic Materials Science and Engineering, South China Institute of Technology, Guangzhou, The People's Republic of China.

[†††]Now at Allied-Signal Inc., Morristown, NJ, 07960 5.1

I. INTRODUCTION

This paper is the third paper in a series of five papers[1-4] describing the development of a thermodynamic theory for the entire lead zirconate-titanate (PZT) solid solution system. Values of the Curie constant (C) and sixth-order polarization interaction dielectric stiffness coefficients (α_{112} and α_{123}) are needed for the development of this theory.

Due to the lack of experimental data, the Curie constant was originally assumed to be independent of composition in the theory developed for the single-cell region of the PZT system.[5] Amin et al.[6] later found from a combination of calorimetric and phenomenological data that the Curie constant was dependent on composition with a peak forming near the morphotropic boundary between the tetragonal and rhombohedral phases. The theory was then modified to account for the compositional dependence of the Curie constant.[7] The Curie constant data determined by Amin et al.[6] extends from lead titanate to the morphotropic boundary between the tetragonal and rhombohedral phases. Additional data were needed to complete the compositional dependence of the Curie constant from the morphotropic boundary to lead zirconate.

In this paper values of C, α_{112}, and α_{123} will be determined as a function of composition from low-temperature polycrystalline dielectric data. In the next section the results of the low-temperature dielectric measurements will be presented. These data will then be used in Section III to determine values of C, α_{112}, and α_{123}. A summary of this paper will be presented in Section IV.

II. LOW-TEMPERATURE DIELECTRIC MEASUREMENTS

Additional experimental data was needed to determine values of the Curie constant and α_{112} and α_{123} coefficients. Low-temperature polycrystalline dielectric data was chosen for this purpose. At low temperatures the thermally activated contributions to the polycrystalline dielectric properties should "freeze out". The remaining dielectric properties

were assumed to be due to an averaging of the single-domain properties.

Zhuang et al.[8] fabricated pure homogeneous polycrystalline ceramic PZT samples from sol-gel derived powders. The same procedure was used to prepare disc shaped samples for use in this study. The samples were cut and polished, and sputtered with gold electrodes. The samples with thermal-resistance wire attached as leads, were then shielded in a copper enclosure in an Air Products and Chemicals model LT-3-110 cryogenics system to cool the temperature to 4.2 K. The dielectric constant and loss were measured at 1 KHz on a Hewlett Packard 4270A automatic digital capacitance bridge.

After measuring the dielectric properties on the unpoled samples at 4.2 K, the same samples were poled with electric fields of 20 to 40 KV/cm for 4 to 30 minutes. The piezoelectric strain coefficient d_{33} was measured using a Berlincourt Piezo-d_{33} meter to determine the completeness of poling. The poled samples were then cooled back down to 4.2 K, and the dielectric properties were remeasured. The unpoled (ε_{33}), and poled ($\varepsilon_{33}{}^P$, parallel to the poling direction) dielectric constant data is listed in Table I.

The Bruggeman formula[9] was used to relate the poled ($\varepsilon_{33}{}^P$) and unpoled (ε_{33}) dielectric constants of the tetragonal and rhombohedral polycrystalline samples to the single-domain constants:

$$\varepsilon_{33}{}^P = 1/4 \, (\varepsilon_{11} - 2 \, \vartheta \, (\varepsilon_{11} + \varepsilon_{33}) + \{[\varepsilon_{11} - 2 \, \vartheta \, (\varepsilon_{11} + \varepsilon_{33})]^2 + 8 \, \varepsilon_{11}\varepsilon_{33}\}^{1/2}) \qquad (1)$$

$$\varepsilon_{33} = 1/4 \, (\varepsilon_{11} + \{\varepsilon_{11}{}^2 + 8 \, \varepsilon_{11}\varepsilon_{33}\}^{1/2}). \qquad (2)$$

ε_{11} and ε_{33} are the dielectric constants perpendicular and parallel to the poling direction, and ϑ is the fraction of 90° or 71° (109°) domain alignment. ε_{11} and ε_{33} were assumed to be equal to the dielectric susceptibilities η_{11} and η_{33} (actually $\varepsilon_{ij} = \eta_{ij} + 1$) for the tetragonal compositions and equal to η_{11}' and η_{33}' for the rhombohedral compositions [see Equations (27) and (29) in Reference 1].

In addition to the poled and unpoled ceramic dielectric constants, the fraction of 90° or 71°(109°) domain alignment ϑ is required to use Equations (1) and (2) to calculate the

single-domain constants. Turik et al.[9] used an x-ray method to determine ϑ as a function of composition. These data were used to approximate values of ϑ as listed in Table I.

The differences between the poled and unpoled ceramic dielectric constants at low temperatures (listed in Table I) showed a similar behavior as was seen at room temperature.[9,10] By poling the samples the dielectric constant decreased for the rhombohedral compositions, and slightly increased for the tetragonal compositions. Turik et al.[9] attributed these changes from poling as being due to the reduction of the clamping effect from the 180° domains. When 180° domains are present, the dielectric constant is lowered from a clamping effect between these domains. By poling a ceramic sample virtually all of the 180° domains reorient closest to the poling direction, and the clamping effect is reduced causing the dielectric constant to increase.

However, 90° or 71°(109°) domain reorientation also occurs during poling, which decreases the dielectric constant if ε_{33} is less than ε_{11}. Thus the dielectric constant will increase or decrease after poling depending on which of these competing mechanisms dominates. In the tetragonal state the small fraction of the 90° domains that realign from poling does not quite cancel out the increase in dielectric constant from the reduction of the clamping effect of the 180° domains, and therefore the dielectric constant increases slightly. In the rhombohedral state a large fraction of the 71° (109°) domains align from poling and dominate the increase from the reduction of the clamping effect, causing the dielectric constant to decrease. In addition, a smaller fraction of 180° domains exist in a rhombohedra ceramic compared to a tetragonal one.[11]

Because of the clamping effect, as described above, Equations (1) and (2) were only used to calculate the single-domain dielectric susceptibilities η_{11}' and η_{33}' for the rhombohedral PZT 94/6 through 54/46 compositions using the data from Table I at 4.2 K . This data is listed in Table II. The single-domain dielectric susceptibilities of the PZT 52/48, 50/50, and 40/60 compositions will be calculated using a different procedure in the next section. The single-domain data will then be used to calculate values of the Curie constant,

and the α_{112} and α_{123} coefficients.

III. EVALUATION OF THE CURIE CONSTANT AND SIXTH-ORDER POLARIZATION INTERACTION DIELECTRIC STIFFNESS COEFFICIENTS

In the second paper in this series[2] the compositional dependences of the $\alpha_{11}C$, $\alpha_{111}C$, ζC, and ξC constants were determined. These constants with the $\alpha_1 C$ constant can be used to calculate the spontaneous polarization and $\Delta G\,C$ of the tetragonal and high temperature rhombohedral phases [Equations (7), (23), (36), and (37) in Reference 2]. In addition to these constants, the Curie constant C, and the polarization interactions coefficients α_{12}, α_{112}, and α_{123} are required to calculate the second derivative properties, such as the dielectric properties [see Equations (27) and (29) in Reference 1].

The $\alpha_{12}C$ constant was calculated from the $\alpha_{11}C$ and ζC [$= 3\,(\alpha_{11} + \alpha_{12})\,C$] constants in Reference 2. A combination of the $\alpha_{112}C$ and $\alpha_{123}C$ constants can be calculated from the $\alpha_{111}C$ and ξC [$= (3\,\alpha_{111} + 6\,\alpha_{112} + \alpha_{111})\,C$] constants with the following relation:

$$(6\,\alpha_{112} + \alpha_{123})\,C = \xi C - 3\,\alpha_{111}C \qquad (3)$$

Using this equation allowed $(6\,\alpha_{112} + \alpha_{123})\,C$ to be calculated from the values of the ξC and $\alpha_{111}C$ that were determined in Reference 2, but additional data were still needed to separate the $\alpha_{112}\,C$ and $\alpha_{123}\,C$ constants.

The low-temperature dielectric data presented in the last section were used to calculate the Curie constant and to separate the dielectric stiffness coefficients α_{112} and α_{123}. To accomplish this the high-temperature rhombohedral equations were used at low temperatures, where actually the low-temperature rhombohedral phase is stable, because of the following reasons.

To calculate the dielectric susceptibility coefficients of the low-temperature rhombohedral phase, the polarization-tilt angle coupling coefficients must be determined, in addition to the dielectric stiffness coefficients [see Equation (30) in Reference 1]. The dielectric properties have been experimentally shown to only change very slightly at the transition between the high and low temperature rhombohedral phases.[12] A fairly good assumption can then be that the dielectric susceptibility coefficients of the high and low temperature rhombohedral phases are equal at the transition between these phases. Using this assumption with the methods described in this paper and the second and fourth papers of this series to determine the other coefficients, the constants needed to calculate the dielectric susceptibilities of the low-temperature rhombohedral phase can be solved for.

However, when using the low-temperature rhombohedral dielectric susceptibility equations and the experimental ceramic data at low temperatures in the present theory (tilt angle coefficients are independent of temperature and only go up to the fourth order), the resulting values of the Curie constant will not agree with the available experimental data. A temperature dependence was added to the second order tilt angle related coefficient [β_1 in Equation (1) of Reference 1], but this still did not resolve the problem. Probably what is needed, in addition to this temperature dependence, is to add a sixth-order tilt angle term to the energy function. But if this is done the equations for the spontaneous polarization and tilt angle will change from quadratic to quartic. At this point the additional complexity resulting from a sixth-order tilt angle term is probably not warranted, and there is not enough experimental data available to properly determine these additional constants.

The question now is how can the low-temperature ceramic dielectric data be used to determine the Curie constant and to separate the sixth order polarization interaction coefficients, if the low-temperature rhombohedral equations will not give reasonable results with the present theory. The dielectric properties of the high and low temperature rhombohedral phases were experimentally found to be very similar at the transition between these phases. If the dielectric properties of these two phases remain similar down to low

temperatures, then the high-temperature rhombohedral dielectric susceptibilities relations could be used at low temperatures.

Using the high-temperature rhombohedral relations at low temperatures produced very reasonable results. A Curie constant of 2×10^5 °C was obtained for the PZT 90/10 composition, which is in excellent agreement with experimental single-crystal measurements.[12] Thus this indicates that the high and low temperature rhombohedral dielectric properties are probably similar down to even very low temperatures (4.2 K). The high-temperature rhombohedral dielectric susceptibility relations were therefore used for the dielectric properties of both the high and low temperature rhombohedral phases, which appears to be a fairly good assumption.

The η_{11}' and η_{33}' data for the rhombohedral PZT 94/6 through 54/46 compositions were used to calculate the Curie constant, and to separate the α_{112} and α_{123} constants from the following high-temperature rhombohedral dielectric stiffness relations:

$$\eta_{11}' = C / \{\varepsilon_0 \, [(T - T_0) / \varepsilon_0 + 12 \, \alpha_{11} C \, P_3^2 + (30 \, \alpha_{111} C + 12 \, \alpha_{112} C - 2 \, \alpha_{123} C) \, P_3^4]\}$$

(4)

$$\eta_{33}' = C / \{\varepsilon_0 \, [(T - T_0) / \varepsilon_0 + 4 \, \zeta C \, P_3^2 + 10 \, \xi C \, P_3^4]\}$$

(5)

These equations from derived from Equations (29), (33), and (40) from Reference 1.

Equation (5) was used to calculate the Curie constant from the η_{33}' data in Table II, and from values of the ζC and ξC constants from Equations (34) and (35) from Reference 2. Equations (4) and (5) were then combined to calculate the $\alpha_{112} C$ and $\alpha_{123} C$ constants using Equations (38) and (42) from Reference 2 to determine values of T_0, $\alpha_{11} C$, and $\alpha_{111} C$. The C, $\alpha_{112} C$, and $\alpha_{123} C$ data are listed in Table II.

The $\alpha_{112} C$ data listed in Table II with the lead titanate value from Reference 13 were fit with the following relation:

$$\alpha_{112} C = a \exp^{-bx} + cx + d ,$$

(6)

where a = 58.804, b = 29.397, c = -3.3754, d = 4.2904, exp is the exponential function, and x is the mole fraction $PbTiO_3$ in PZT.

The compositional dependence of the $\alpha_{123}C$ constant was determined from the following relation derived from equation (3):

$$\alpha_{123}C = \xi C - 3\,\alpha_{111}C - 6\,\alpha_{112},\tag{7}$$

where ξC and $\alpha_{111}C$ were determined from Equations (35) and (38) from Reference 2, and $\alpha_{112}C$ was determined from Equation (6) above. The data from Table II and the calculations from Equations (6) and (7) are shown in Figure 1.

The Curie constants of the PZT 52/48 and 50/50 compositions were determined by substituting Equations (4) and (5) into Equation (1), and using the $\varepsilon_{33}{}^{P}$ data from Table I, along with the dielectric stiffness constants calculated from the previously given equations. Values of $\eta_{11}{}'$ and $\eta_{33}{}'$ were then calculated from Equations (4) and (5) and are listed in Table II. This procedure was also used for the tetragonal PZT 40/60 composition using Equations (27) and (36) from Reference 1 for the tetragonal dielectric susceptibilities. The values of C, η_{11}, and η_{33} are listed in Table II.

The best least-squares fit of the following relations were used to fit the compositional dependence of the Curie constant using the data listed in Table II along a value of 1.5×10^5 °C for $PbTiO_3$:

For x ≤ 0.5 : $C = [2.1716 / (1 + 500.05\ x)^2 + 0.131\ x + 2.01]\ 10^5$

For x ≥ 0.5 : $C = [2.8339 / (1 + 126.56\ x)^2 + 1.4132]\ 10^5$ (8)

The Curie constant data and fitting from this equation are plotted in Figure 2. Amin et al.[7] also found a peak to occur in the Curie constant at the PZT 50/50 composition, although their peak value was somewhat larger than the results presented here (7.7 versus 4.3×10^5 °C). Tsuzuki et al.[14] experimentally found Curie constant values of 5.8 and 6.0×10^5 °C from single-crystal dielectric measurements on PZT 50/50 and 51/49 compositions.

The dielectric data listed in Table II are plotted in Figure 3, along with the theoretical calculations using the constants determined in this paper. The cross over of the η_{11}' and η_{33}' coefficients on the rhombohedral side of the diagram resulted from the extrapolation of the constants between the compositions where the data points occur, and may or may not be a real effect in the material. In any case the dielectric anisotropy becomes very small in this region. A more detailed discussion of the dielectric anisotropy will be provided Reference 4.

IV. SUMMARY

The dielectric properties were measured on unpoled and poled polycrystalline samples at 4.2 K. These data were used to calculate the single-domain dielectric susceptibility coefficients using the Bruggeman relation. Values of the Curie constant and α_{112} and α_{123} coefficients were calculated from the single-domain data. Equations were then used to fit these values to determine the compositional dependence of the coefficients for use in the development of a thermodynamic theory for the PZT system. As a summary of this paper and the second paper of the series,[2] Table III gives values of the coefficients of the energy function.

The Curie constant was found to form a peak at the PZT 50/50 composition, similar to the compositional dependence of the electrostrictive constants.[15] This type of behavior is in agreement with earlier data in the literature,[6,7,14] but at this point it is not clear whether the peak is occuring due to the morphotropic boundary between the tetragonal and rhombohedral phases or due to some other effect. The Curie constant is a constant from the high-temperature cubic state, and thus should probably not be related to the morphotropic boundary. By studying the compositional dependence of these constants in other solid solution systems where a morphotropic boundary occurs away from the 50/50 composition [e.g. $Pb(Mg_{1/3}Nb_{2/3})O_3$ - $PbTiO_3$ system] may help to resolve some of these questions.

REFERENCES

[1] M. J. Haun, E. Furman, S. J. Jang, and L. E. Cross, "Thermodynamic Theory of the Lead Zirconate-Titanate Solid Solution System, Part I: Phenomenology," J. Appl. Phys. (submitted).

[2] M. J. Haun, E. Furman, H. A. McKinstry, and L. E. Cross, "Thermodynamic Theory of the Lead Zirconate-Titanate Solid Solution System, Part II: Tricritical Behavior," J. Appl. Phys. (submitted).

[3] M. J. Haun, E. Furman, T. R. Halemane, and L. E. Cross, "Thermodynamic Theory of the Lead Zirconate-Titanate Solid Solution System, Part IV: Tilting of the Oxygen Octahedra," J. Appl. Phys. (submitted).

[4] M. J. Haun, E. Furman, S. J. Jang, and L. E. Cross, "Thermodynamic Theory of the Lead Zirconate-Titanate Solid Solution System, Part V: Theoretical Calculations," J. Appl. Phys. (submitted).

[5] A. Amin, *Phenomenological and Structural Studies of Lead Zirconate- Titanate Piezoceramics*, Ph.D. Thesis in Solid State Science, The Pennsylvania State University (1979).

[6] A. Amin, L. E. Cross, and R. E. Newnham, Ferroelectrics 65, 107 (1985).

[7] A. Amin, M. J. Haun, B. Badger, H. A. McKinstry, and L. E. Cross, Ferroelectrics 65, 107 (1985).

[8] Z. Q. Zhuang, M. J. Haun, S. J. Jang, and L. E. Cross, Am. Ceram. Soc., (submitted).

[9] A. V. Turik, M. F. Kupriyanov, E. N. Sidorenko, and S. M. Zaitsev, Zh. Tekh. Fiz. 50, 2146 (1980) [Sov. Phys. Tech. Phys. 25, 1251(1980)].

[10] Z. Q. Zhuang, M. J. Haun, S. J. Jang, and L. E. Cross, *Proceedings of the 6th IEEE International Symposium on the Applications of Ferroelectrics*, Lehigh, PA, edited by Van Wood (IEEE, New York, 1986) pp. 394-397.

[11] D. Berlincourt and H. A. Krueger, J. Appl. Phys. 30, 1804 (1959).

[12]R. W. Whatmore, R. W., R. Clarke, and A. M. Glazer, J. Phys. C: Solid State Phys., **11**, 3089 (1978).

[13]M. J. Haun, Thermodynamic Theory of $PbTiO_3$, J. Appl. Phys. **62**, 3331 (1987).

[14]K. Tsuzuki, K. Sakata, and M. Wada, Ferroelectrics, **8**, 501 (1974).

[15]M. J. Haun, Z. Q. Zhuang, E. Furman, S. J. Jang, and L. E. Cross, Am. Ceram. Soc. (submitted).

LIST OF FIGURES AND TABLES

Figure 1. Product of the sixth-order polarization interaction dielectric stiffness coefficients and the Curie constant plotted versus composition. The data points were determined from experimental data. The solid curves are fits of the data using Equations (6) and (7).

Figure 2. The Curie constant plotted versus composition. The data points are from Table II. The solid curve is a fitting of the data using Equation (8).

Figure 3. The dielectric susceptibility coefficients η_{11} and η_{33} in the tetragonal state and η_{11}' and η_{33}' in the rhombohedral state plotted versus composition at 4.2 K. The data points are from Table II, except for the points at $PbTiO_3$ which are from Reference 13. The solid curves are the theoretical calculations after determining the compositional dependence of the coefficients.

Table I. The Dielectric Constant at 4.2 K on Poled and Unpoled Ceramic Samples and the Fraction of 90° (or 71, 109°) Domain Alignment ϑ.

Table II. Calculations from the Low Temperature Ceramic Dielectric Data.

Table III. Values of the Coefficients of the Energy Function at 25 °C.

Table I. The Dielectric Constant at 4.2 K on Poled and Unpoled Ceramic Samples and the Fraction of 90° (or 71, 109°) Domain Alignment ϑ.

Zr/Ti	ε_{33}^P	ε_{33}	ϑ
94/6	93.2	87.2	0.65
90/10	106.2	101.1	0.65
70/30	139.4	135.3	0.65
60/40	173.2	156.2	0.63
54/46	282.6	232.5	0.50
52/48	324.3	303.0	0.34
50/50	326.8	328.4	0.30
40/60	200.6	202.0	0.23

Table II. Calculations from the Low Temperature Ceramic Dielectric Data.

Zr/Ti	η_{11}' or η_{11}	η_{33}' or η_{33}	C $(10^5\,°C)$	$\alpha_{112}C$ $(10^{14}\,m^9\,°C/\,C^4\,F)$	$\alpha_{123}C$ $(10^{15}\,m^9\,°C/\,C^4\,F)$
Rhombohedral					
94/6	98.0	84.1	2.0031	13.905	- 3.3019
90/10	110.2	98.4	2.0823	7.0625	- 1.8033
70/30	142.6	133.1	2.1648	3.3549	- 1.5592
60/40	187.5	146.8	2.4243	3.1431	- 1.5008
54/46	338.4	189.4	3.1714	2.4256	- 1.1019
52/48	392.3	243.3	4.0965	——	——
50/50	429.7	254.1	4.2962	——	——
Tetragonal					
40/60	325.1	110.4	2.6951	——	——

Table III. Values of the Coefficients of the Energy Function at 25 °C.

	Mole Fraction PbTiO$_3$ in PZT										
	0.0	0.1	0.2	0.3	0.4	0.5	0.6	0.7	0.8	0.9	1.0
T_C (°C)	231.5	256.5	300.6	334.4	364.3	392.6	418.4	440.2	459.1	477.1	492.1
C (10^5 °C)	2.027	2.050	2.083	2.153	2.424	4.247	2.664	1.881	1.642	1.547	1.500
Q_{11} (10^{-2} C/m^2)	4.620	5.080	5.574	6.175	7.260	9.660	8.116	7.887	8.142	8.504	8.900
Q_{12} (10^{-2} C/m^2)	-1.391	-1.540	-1.720	-1.997	-2.708	-4.600	-2.950	-2.480	-2.446	-2.507	-2.600
Q_{44} (10^{-2} C/m^2)	4.664	4.900	5.165	5.522	6.293	8.190	6.710	6.356	6.417	6.569	6.750
α_1 (10^7 m/F) at 25°C	-4.582	-6.376	-7.470	-8.116	-7.904	-4.887	-8.340	-12.47	-14.84	-16.17	-17.08
α_{11} (10^7 m^5/C^2 F)	52.35	41.25	31.29	22.30	13.62	4.764	3.614	0.6458	-3.050	-5.845	-7.253
α_{12} (10^8 m^5/C^2 F)	-16.71	-4.222	-0.0345	1.688	2.391	1.735	3.233	5.109	6.320	7.063	7.500
ζ (10^8 m^5/C^2 F)	-34.42	-0.2897	9.284	11.75	11.26	6.634	10.78	15.52	18.05	19.44	20.32
α_{111} (10^8 m^9/C^4 F)	5.932	5.068	4.288	3.560	2.713	1.336	1.859	2.348	2.475	2.518	2.606
α_{112} (10^8 m^9/C^4 F)	311.2	34.45	18.14	15.27	12.13	6.128	8.503	10.25	9.684	8.099	6.100
α_{123} (10^9 m^9/C^4 F)	-104.1	-8.797	-7.545	-7.052	-5.690	-2.894	-4.063	-5.003	-4.901	-4.359	-3.660
ξ (10^9 m^9/C^4 F)	84.41	13.39	4.627	3.176	2.402	1.183	1.596	1.851	1.652	1.256	0.7818

Fig. 1
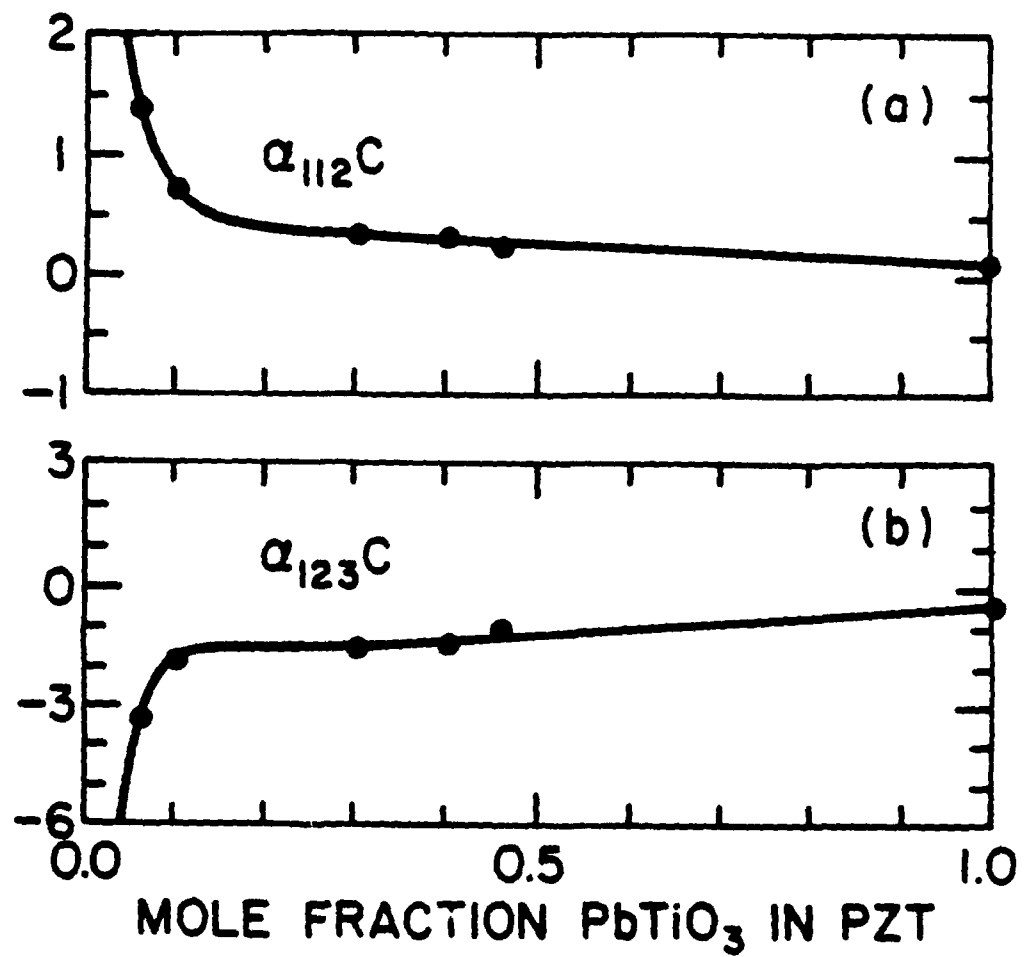
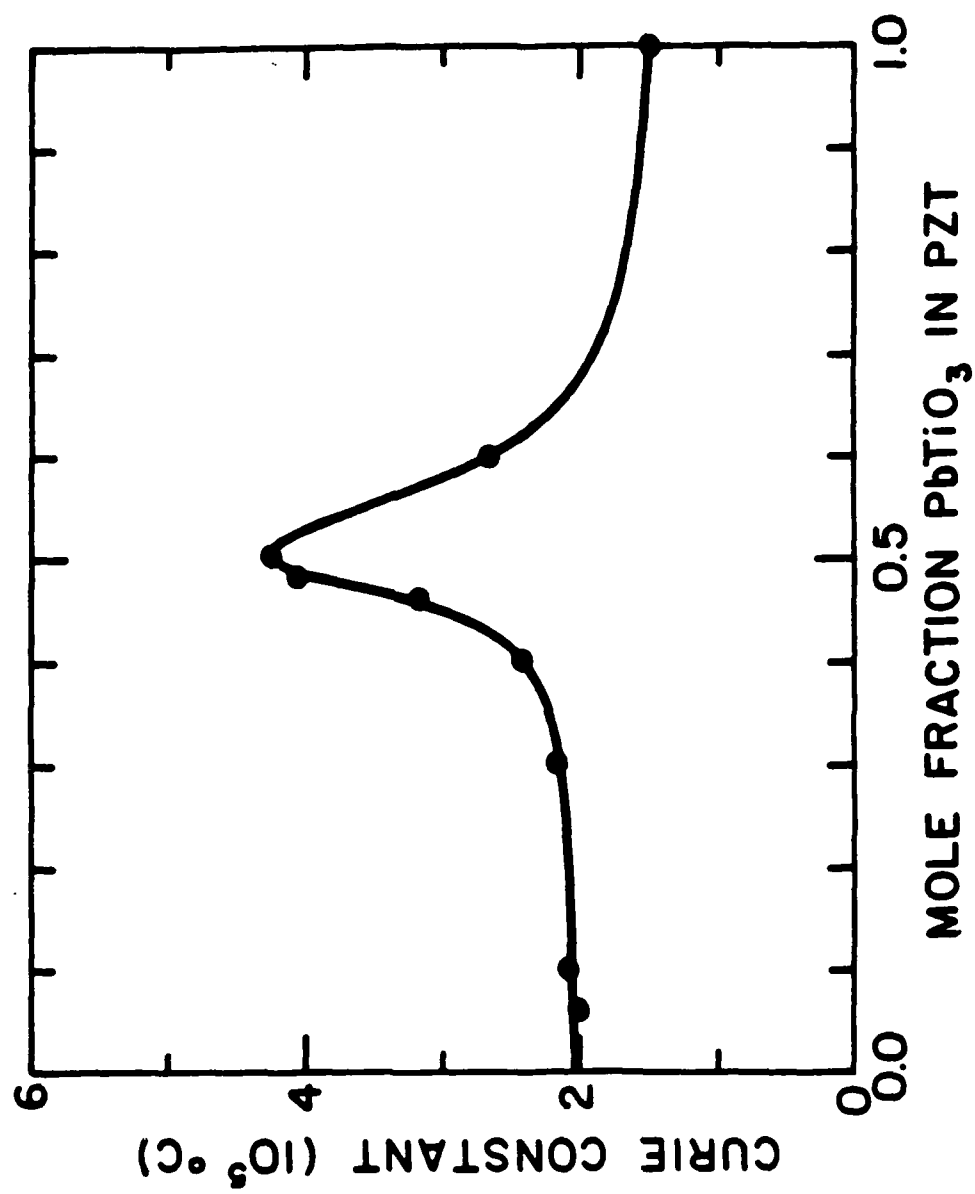CURIE CONSTANT $(10^5\ °C)$

MOLE FRACTION PbTiO$_3$ IN PZT

Fig. 2
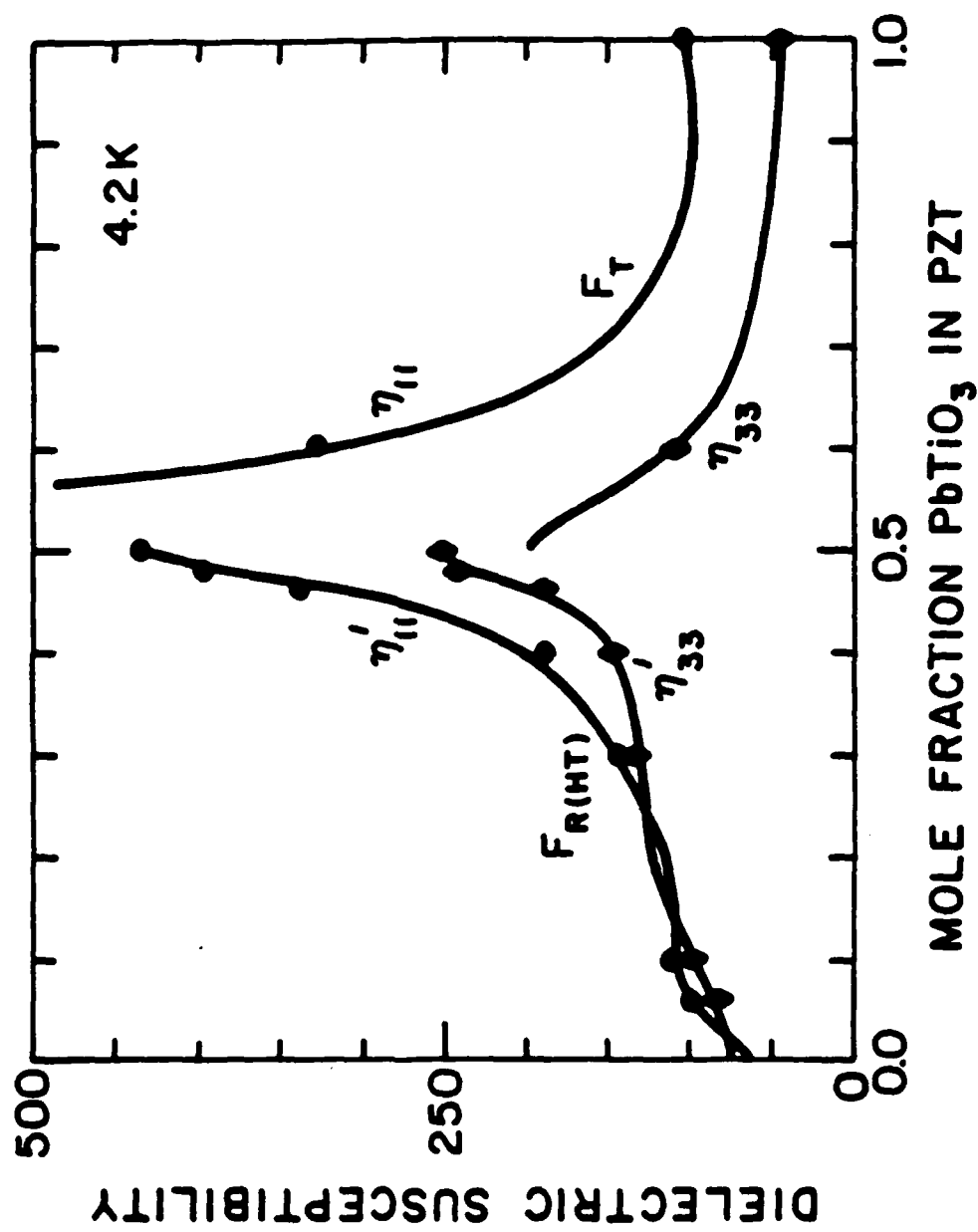
Fig. 3

THERMODYNAMIC THEORY OF THE LEAD ZIRCONATE-TITANATE SOLID SOLUTION SYSTEM, PART IV: TILTING OF THE OXYGEN OCTAHEDRA

M.J. Haun,[†] E. Furman,[††] T.R. Halemane,[†††] and L.E. Cross

Materials Research Laboratory
The Pennsylvania State University
University Park, PA 16802

Values of coefficients related to the tilting of the oxygen octahedra in the low-temperature rhombohedral phase of the lead zirconate-titanate (PZT) solid solution system are needed in the development of a thermodynamic theory of the PZT system. In this paper these coefficients will be determined from experimental spontaneous strain and oxygen octahedral tilt angle data.

Values of the tilt angle related coefficients β_1, β_{11} and Φ are assumed to be independent of temperature and are then related to P_H, P_L and T_R where P_H is the spontaneous polarization in the untilted phase and P_L the polarization in the tilted phase at the transition temperature T_R between tilted and nontilted structures.

P_L and θ_L are derived from experimental data for the PZT 90/10 composition, and used together with spontaneous strain values at this composition to determine electrostriction (Q_{44}) and rotostriction R_{44} constants. These constants are then in turn used to derive P_L and θ_L values for other PZT compositions from the spontaneous strain vs temperature at each composition, and in the final paper in this sequence to derive the β_1, β_{11} and Φ values for these compositions.

[†]Now at DuPont Experimental Station, Electronics Dept., Bldg. 334, Wilmington, DE 19898.
[††]Now at Allied-Signal Inc., Morristown, NJ 07960.
[†††]Now at AT&T Bell Laboratories, Holmdel, NJ 07733.

I. INTRODUCTION

This paper is the fourth paper in a series of five papers[1-4] describing the development of a thermodynamic theory for the entire lead zirconate-titanate (PZT) solid solution system. In the low-temperature rhombohedral phase in the PZT system the oxygen octahedra tilt or rotate about the polar axis. In the first paper of this series the oxygen octahedral tilt angle was included in the PZT energy function as an order parameter [see Equation (1) in Reference 1] to account for the low-temperature rhombohedral phase. In this paper the tilt angle related coefficients of the energy function will be determined.

II. EVALUATION OF THE TILT ANGLE RELATED COEFFICIENTS

The tilt angle related coefficients will be determined from the available experimental low-temperature rhombohedral spontaneous strain and tilt angle data. Multiplying the energy of the low-temperature rhombohedral state [Equation (12) in Reference 1] by the Curie constant results in the following relation:

$$F_{R(LT)} \qquad \Delta G \, C = 3 \, \alpha_1 C \, P_3{}^2 + \zeta \, C \, P_3{}^4 + \xi \, C \, P_3{}^6 + 3 \, \beta_1 C \, \theta_3{}^2$$
$$+ 3 \, \beta_{11} C \, \theta_3{}^4 + 3 \, \phi \, C \, P_3{}^2 \, \theta_3{}^2 . \tag{1}$$

$$\text{where} \quad \phi \, C = (\gamma_{11} + 2 \, \gamma_{12} + \gamma_{44}) \, C \tag{2}$$

$\zeta \, C$ and $\xi \, C$ were defined by Equation (24) in Reference 2.

Equations for the spontaneous polarization P_3 and tilt angle θ_3 can be found from the first partial derivative relations [Equations (17) and (18) in Reference 1]:

$$P_3{}^2 \text{ and } \theta_3{}^2 = \frac{-b + [b^2 - 4 \, a \, c]^{1/2}}{2 \, a} .$$

where for $P_3{}^2$:
$$a = \xi \, C$$
$$b = 2/3 \; \zeta \, C - (\phi \, C)^2/(2 \, \beta_{11} C)$$
$$c = \alpha_1 \, C - \beta_1 C \, \phi \, C/(2 \, \beta_{11} C) \tag{3}$$

and for θ_3^2:
$$a = 4 \xi C (\beta_{11}C)^2/(\phi C)^2$$
$$b = \phi C + 4/3\, \beta_{11}C/(\phi C)\, [3\, \xi C\, \beta_1 C\, /(\phi C) - \zeta C]$$
$$c = \alpha_1 C + \beta_1 C/(\phi C)\, [\xi C\, \beta_1 C\, /(\phi C) - 2/3\, \zeta C] \tag{4}$$

Values of the $\alpha_1 C$, ζC, and ξC coefficients were determined in the second paper in this series. Thus the tilt angle related coefficients $\beta_1 C$, $\beta_{11}C$, and ϕC are the only unknown coefficients in these equations. These coefficients were assumed to be independent of temperature, and were related to three new constants at the high to low temperature rhombohedral transition temperature, T_R, using the first partial derivative stability conditions [Equations (17) and (18) in Reference 1], and by equating the energies of the two phases at the boundary [Equations (1) above and Equation (37) in Reference 2]. This resulted in the following equations:

$$\phi C = -1/\theta_L^2\, [2\,(3\, \alpha_{11}C + \alpha_{12}C)\,(P_H^2 - P_L^2)$$
$$+ (15\, \alpha_{111}C + 14\, \alpha_{12}C + \alpha_{123}C)\,(P_H^4 - P_L^4)] \tag{5}$$

$$\beta_1 C = -\phi C\, P_L^2 + 1/\theta_L^2\, [(T_R - T_0)/\epsilon_0\,(P_H^2 - P_L^2) + 2/3\, \zeta C\,(P_H^4 - P_L^4)$$
$$+ 2/3\, \xi C\,(P_H^6 - P_L^6)] \tag{6}$$

$$\beta_{11}C = 1/\theta_L^4\, [(T_R - T_0)/(2\, \epsilon_0)\,(P_H^2 - P_L^2) + \zeta C/3\,(P_H^4 - P_L^4)$$
$$+ \xi C/3\,(P_H^6 - P_L^6) - \beta_1 C\, \theta_L^2 - \phi C\, P_L^2 \theta_L^2] \tag{7}$$

P_H and P_L are the spontaneous polarization of the high and low temperature rhombohedral states at T_R. θ_L is the tilt angle of the low-temperature rhombohedral state at T_R.

P_H can be calculated from Equation (23) in Reference 2 using the constants determined in Reference 2. Thus by determining T_R, P_L, and θ_L the ϕC, $\beta_1 C$, and $\beta_{11}C$ constants can be calculated. When calculating these constants, the ϕC constant should be found first from Equation (5). This value should then be used in Equation (6) to calculate the $\beta_1 C$ constant. Finally the values of the ϕC and $\beta_1 C$ constants should be used in Equation (7) to solve for the $\beta_{11}C$ constant.

The following least squares fit of the experimental phase diagram was used to determine the compositional dependence of T_R:

For $x \leq 0.15$: $T_R = a + bx + cx^2$
where $a = -105.07$, $b = 2812.6$, $c = -7665.9$

For $x \geq 0.15$: $T_R = a + bx + cx^2 + dx^3 + ex^4$
where $a = 5.5465$, $b = 2388.8$, $c = -13864.$, $d = 32282.$, $e = -32675.$ (8)

In fitting the data with $x \geq 0.15$ an additional data point was added at the PZT 50/50 composition at a temperature of -273 °C. This was required to keep the high to low temperature rhombohedral boundary from crossing the morphotropic boundary at low temperatures. The fit of the experimental data using these equations is shown in Reference 4 in Figure 2.

Glazer et al.[5] determined the spontaneous tilt angle for the PZT 90/10 composition at 25 and 60 °C. The values of the tilt angle reported represent the rotation about the cubic [111] direction. In the three-dimensional energy function used in this theory components (θ_3) of the resultant tilt were included. Thus the component tilts were first calculated from the resultant tilts that were reported in the literature. The following relation was derived to relate the component tilts (θ_3) about each orthogonal axis to the resultant tilt (θ_S) about the body diagonal:

$$\cos \theta_3 = 1/3 \, (2 + \cos \theta_S) \qquad (9)$$

Another relation was also found to give similar results as Equation (9) for small angles:

$$3^{1/3} \theta_3 = \theta_S \qquad (10)$$

Equation (10) was used to calculate the component tilt (θ_3) from Glazer et al.'s data.

This data was then used to determine the P_L and θ_L constants for the PZT 90/10 composition that gave the best least-squares fit using Equation (4) combined with Equations

(5) - (8). The resulting values of P_L and θ_L are listed in Table I. The experimental data and the fit using these constants is shown in Figure 5 in Reference 4.

The rotostrictive R_{44} constant was used to fit the low-temperature rhombohedral spontaneous strain x_4 data (from Reference 6) for the PZT 90/10 composition using Equation (24) from Reference 1, and the values of P_L and θ_L determined above. Using the value of the electrostrictive constant Q_{44} of 0.049 m^4/C^2 from Reference 7, resulted in a poor fit of the experimental data. However, a good fit was obtained by varying both the Q_{44} and R_{44} constants. The best least-squares fit resulted in Q_{44} and R_{44} values of 0.0433 m^4/C^2 and - 1.93 x 10^{-4} deg^{-2}, respectively. The experimental strain data and the fit using these values is shown in Figure 1(a).

The change in the Q_{44} constant from high to low temperature rhombohedral phases may indicate that the tilting of the oxygen octahedra influences the electrostriction, resulting in different electrostrictive constants in these two phases. Another possible cause of this could be that the tilt angle coefficients are temperature dependent and/or that a higher order tilt angle coefficient is needed (θ^6 term). However, to not complicate matters any more than they already are, the Q_{44} and R_{44} constants of the low-temperature rhombohedral state were assumed to have the values given above independent of temperature and composition. The values of the electrostrictive constants of the high temperature rhombohedral state were still kept the same as given in Reference 7.

Using the same values of the Q_{44} and R_{44} constants given above for the PZT 90/10 composition, values of P_L and θ_L were found that gave the best least-squares fit of the experimental spontaneous strain data for the PZT 80/20 composition. These values are listed in Table II. The experimental data and fit using these values are plotted in Figure 1(b).

The spontaneous strain x_4 was measured at two temperatures in the low-temperature rhombohedral state for the PZT 70/30 composition. Since there were only two data points, a procedure was used to combine these data with a single tilt angle value at 9K that was measured by Amin et al.[8] for the PZT 60/40 composition.

The first step was to make an initial guess at a value of P_L for the PZT 70/30 composition. This value of P_L was used with the P_L values listed in Table I for the PZT 90/10 and 80/20 compositions to solve for a quadratic compositional dependence of P_L (three unknown constants and three data points). This equation was used to extrapolate a value of P_L to the PZT 60/40 composition, which allowed a value of θ_L to be found that fit the tilt angle data at 9K. This value of θ_L was used with the θ_L values listed in Table I for the PZT 90/10 and 80/20 compositions to solve for a quadratic compositional dependence of θ_L. This equation was then used to calculate a value of θ_L back at the PZT 70/30 composition. This value was used with the initial guess of P_L to determine the spontaneous strain x_4, and to calculate the least-squares error with the two data points. Another guess of P_L for the PZT 70/30 composition was then made, and the entire procedure repeated until the values that gave the best least-squares error were found.

A problem developed from the procedure described above: P_L became less than P_H for compositions near PZT 60/40. The difference in the values between P_L and P_H decreased from around PZT 80/20 to PZT 60/40, which seems to be in agreement with pyroelectric measurements.[9] However, it was felt that P_L should probably not become less than P_H (the polarization should increase when going to the low-temperature rhombohedral phase). Thus an additional manipulation was used to keep P_L from becoming less than P_H. To allow the difference between P_L and P_H to decrease as the titanium content increased, but to keep this difference from going to zero within the stability region of the low-temperature rhombohedral phase, an additional P_L data point was included in determining the compositional dependence of P_L. This value was arbitrarily chosen by letting P_L become equal to P_H at the PZT 50/50 composition. This effectively moved the composition where P_L became equal to P_H into a metastable region.

This value of P_L at PZT 50/50 (listed in Table I) was then used with the previous values of P_L for the PZT 90/10, 80/20, and 70/30 compositions to determine the compositional dependence of P_L by fitting the data with a cubic polynomial equation (four

unknowns and four data points). This equation was used to calculate a P_L value back at the PZT 60/40 composition. Using this value a new θ_L value for PZT 60/40 was found by refitting the experimental tilt angle data point at 9 K. This value of θ_L for PZT 60/40 was then used with the previous values of θ_L for the PZT 90/10, 80/20, and 70/30 compositions to determine the compositional dependence of θ_L from a cubic polynomial fit.

The final values of P_L and θ_L used in the fitting are listed in Table I, and plotted in Figure 2. The cubic compositional fits, also plotted in Figure 2, of these data are:

$$P_L \text{ and } \theta_L = a + b x + c x^2 + d x^3,$$

where for P_L:

$$\begin{aligned} a &= 0.28079 \\ b &= -0.030117 \\ c &= -0.46150 \\ d &= 1.8367 \end{aligned} \tag{11}$$

and for θ_L:

$$\begin{aligned} a &= 0.91540 \\ b &= 12.967 \\ c &= -40.255 \\ d &= 11.417 \end{aligned} \tag{12}$$

The experimental spontaneous strain data and final fit for the PZT 70/30 composition are plotted in Figures 1(c). The experimental tilt angle data point and final fit for the PZT 60/40 composition is plotted in Figure 5 in Reference 4.

With the compositional dependences of T_R, P_L, and θ_L determined from Equations (8), (11), and (12), the tilt angle related constants $\beta_1 C$, $\beta_{11} C$, and ϕC can be calculated from Equations (5) - (7).

III. SUMMARY

The tilt angle related coefficients, $\beta_1 C$, $\beta_{11} C$, and ϕC, were related to three new constants, T_R, P_L and θ_L, at the transition between the high and low temperature

rhombohedral phases. The transition temperature between these phases, T_R, was determined from the phase diagram. Values of the spontaneous polarization and tilt angle of the low-temperature rhombohedral phase at T_R, P_L and θ_L, were determined from experimental spontaneous strain and tilt angle data. These values were then fit with equations to determine the compositional dependence of P_L and θ_L. These equations will be used in the last paper in this series to calculate the values of β_1, β_{11}, and ϕ for theoretical calculations of the phase stability and properties of the low-temperature rhombohedral phase. As a summary of this paper Table II gives values of these constants at four PZT compositions.

REFERENCES

[1] M. J. Haun, E. Furman, S. J. Jang, and L. E. Cross, "Thermodynamic Theory of the Lead Zirconate-Titanate Solid Solution System, Part I: Phenomenology," J. Appl. Phys. (submitted).

[2] M. J. Haun, E. Furman, H. A. McKinstry, and L. E. Cross, "Thermodynamic Theory of the Lead Zirconate-Titanate Solid Solution System, Part II: Tricritical Behavior," J. Appl. Phys. (submitted).

[3] M. J. Haun, E. Furman, T. R. Halemane, and L. E. Cross, "Thermodynamic Theory of the Lead Zirconate-Titanate Solid Solution System, Part III: Curie Constant and Sixth-order Polarization Interaction Dielectric Stiffness Coefficients," J. Appl. Phys. (submitted).

[4] M. J. Haun, E. Furman, S. J. Jang, and L. E. Cross, "Thermodynamic Theory of the Lead Zirconate-Titanate Solid Solution System, Part V: Theoretical Calculations," J. Appl. Phys. (submitted).

[5] A. M. Glazer, S. A. Mabud, and R. Clarke, Acta Cryst. B34, 1060 (1978).

[6] M. J. Haun, Y. H. Lee, H. A. McKinstry, and L. E. Cross, Advances in X-ray Analysis, Vol. 30, edited by C. S. Barrett, J. V. Gilfrich, R. Jenkins, D. E. Leyden, J. C. Russ, and P. K. Predecki (Plenum Press, New York, 1987) pp. 473-481.

[7] M. J. Haun, Z. Q. Zhuang, E. Furman, S. J. Jang, and L. E. Cross, Am. Ceram. Soc. (submitted).

[8] A. Amin, R. E. Newnham, L. E. Cross, and D. E. Cox, J. Solid State Chemistry 37, 248 (1981).

[9] Z. Q. Zhuang, M. J. Haun, A. Bhalla, S. J. Jang, and L. E. Cross, unpublished data.

LIST OF FIGURES AND TABLES

Table I. Values of P_L and θ_L.

Zr/Ti	P_L (C/m^2)	θ_L (deg.)
90/10	0.275	1.82
80/20	0.271	1.99
70/30	0.280	1.49
60/40	——	0.392
50/50	0.380	——

Table II. Values of the Tilt Angle Related Coefficients at 25 °C.

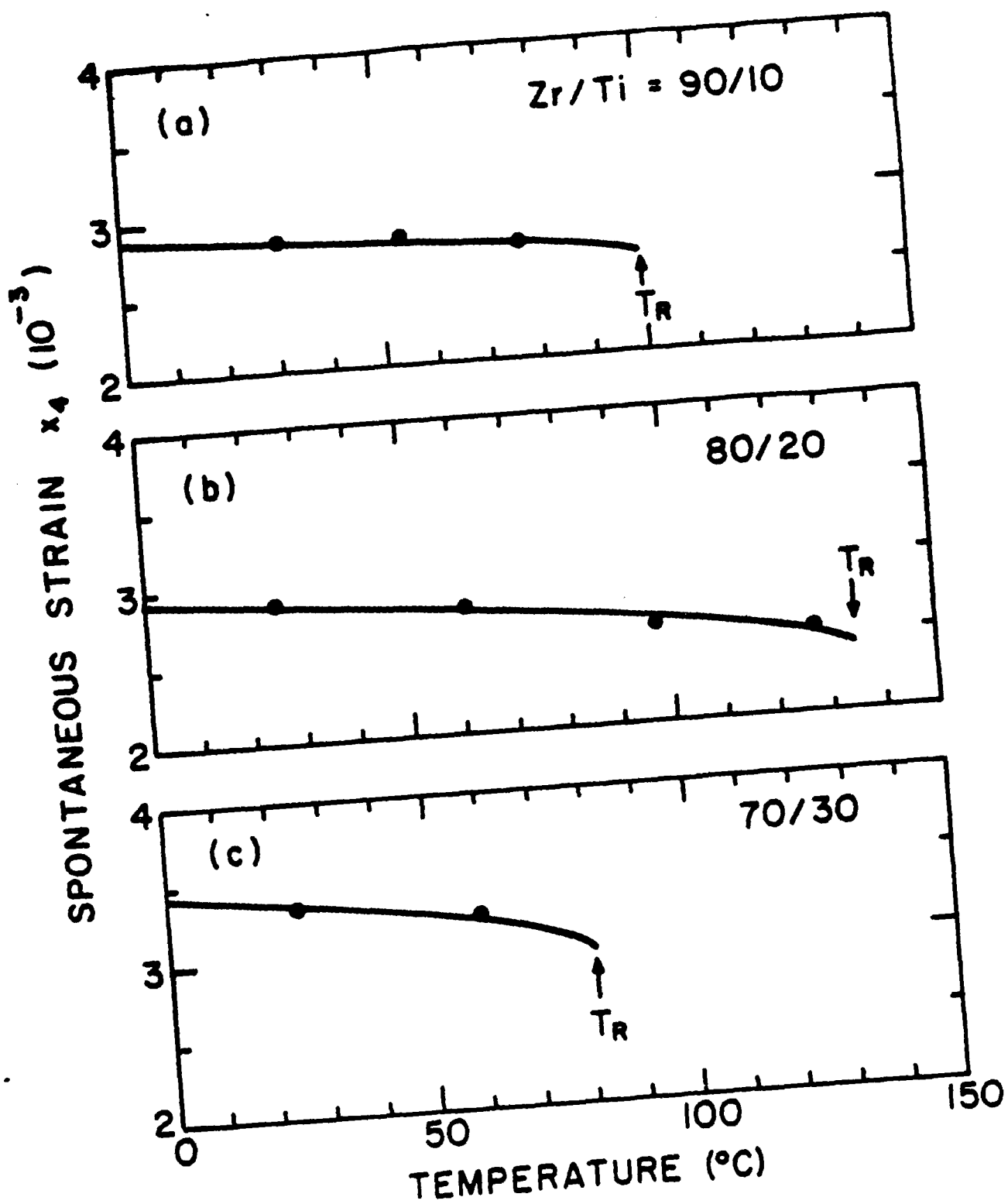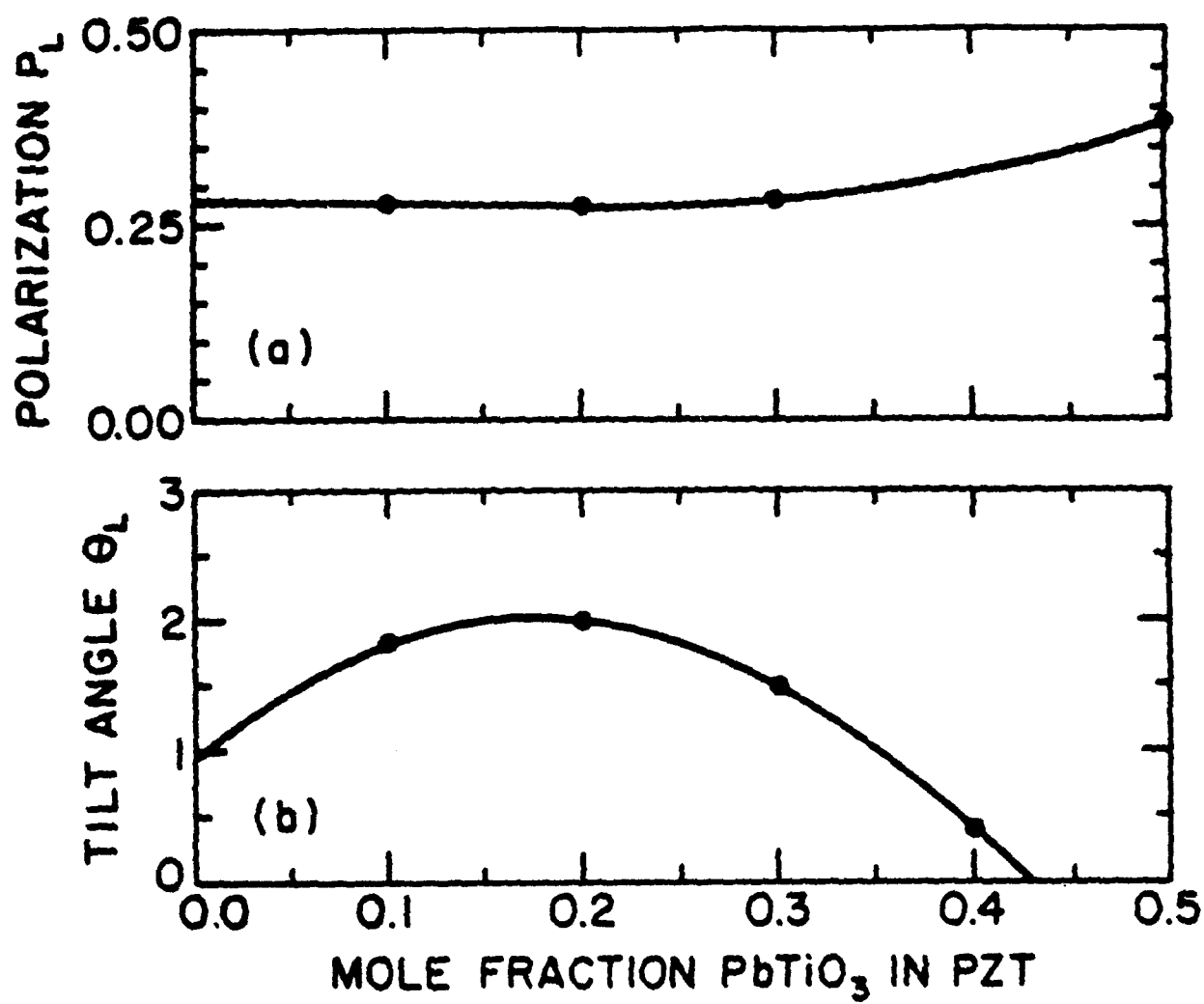|	Mole Fraction PbTiO$_3$ in PZT			
	0.1	0.2	0.3	0.4
β_1 (10^5 J/m^3 Deg^2)	5.618	3.395	4.343	29.79
β_{11} (10^4 J/m^3 Deg^4)	2.506	1.674	1.682	4.174
ϕ (10^6 m/F Deg^2)	- 9.626	- 6.428	- 6.502	- 31.82

Fig. 1

Fig. 2

THERMODYNAMIC THEORY OF THE LEAD ZIRCONATE-TITANATE SOLID SOLUTION SYSTEM, PART V: THEORETICAL CALCULATIONS

M.J. Haun,[†] E. Furman,[††] S.J. Jang, and L.E. Cross

Materials Research Laboratory
The Pennsylvania State University
University Park, PA 16802

In this final paper of a sequence of five papers presenting details of a thermodynamic phenomenology for the whole $PbZrO_3:PbTiO_3$ solid solution family, the constants derived in the earlier papers are used to calculate the temperature and composition dependence of the Elastic Gibbs Free Energy ΔG_1 at zero stress, the spontaneous electric polarization and the spontaneous tilt of the oxygen octahedra in a single domain, the anisotropic weak field dielectric permittivity and the piezoelectric constants for compositions all across the phase diagram.

These data can be used to determine the intrinsic component of the behavior of any pure lead zirconate:lead titanate in any part of the phase field and at any temperature, and thus can form a first step in the separation of the experimentally observed properties into their intrinsic (single domain) component and their extrinsic domain and defect related responses.

The function proposed is certainly not the final word for PZT, and will clearly be subjected to continuous modification and improvement as new and better experimental data becomes available. The purpose of the exercise has been to correlate a very wide panoply of experimental data within a single function and to extract from it the constants which would be directly accessible if single domain single crystals could be grown at the interesting $PbZrO_3:PbTiO_3$ compositions.

[†]Now at DuPont Experimental Station, Electronics Dept., Bldg. 334, Wilmington, DE 19898.
[††]Now at Allied-Signal Inc., Morristown, NJ 07960.

I. INTRODUCTION

This paper is the final paper in a series of five papers[1-4] describing the development of a thermodynamic theory for the entire lead zirconate-titanate (PZT) solid solution system. In this paper theoretical calculations will be made using the equations that were derived in the first paper[1] of the series, and the values of the coefficients determined in the second, third, and fourth papers.[2-4] The antiferroelectric calculations will be made using the coefficients that were determined in Reference 5.

The free energies of each phase will be calculated in the next section and used to determine the phase diagram. In Section III the spontaneous polarization and tilt angle will be calculated. The dielectric and piezoelectric properties will then be calculated in Sections IV and V, followed by a summary and discussion of the future applications of this theory.

II. PHASE DIAGRAM

In the second paper of the series products of the dielectric stiffness coefficients (α_{ij}) and the Curie constant (C) were shown to be independent of C. These new constants (α_{ij} C) can be used to calculate products of the free energies and the Curie constant (ΔG C), which are also independent of C. Since the Curie constant is the same in all of the solutions of the energy function, the ΔG C products can be used to determine the phase stability independent of the effect of the compositional dependence of C.

In Figure 1 the product of the energies and Curie constant (C) are plotted versus composition at three temperatures. The solution with the lowest ΔG C product corresponds to the stable phase, and a phase transition occurs when the curves cross. At 25 °C [Figure 1(c)] the tetragonal solution has the lowest ΔG C on the lead titanate side of the figure, and is thus the stable phase. Moving across the figure towards lead zirconate the tetragonal phase remains stable to the dashed line labeled 5. At this point the ΔG C of the high-temperature rhombohedral solution becomes less than that of the tetragonal phase, and a

phase transition occurs between these phases (the morphotropic phase boundary).

Continuing across the figure the high-temperature rhombohedral phase remains stable to the dashed line labeled 4, where a transition to the low-temperature rhombohedral phase occurs. This phase is then stable until the dashed line labeled 2 is reached, and a transition to the antiferroelectric orthorhombic phase occurs. At higher temperatures an additional region of high-temperature rhombohedral phase develops between the low-temperature rhombohedral and antiferroelectric orthorhombic phase fields. The low-temperature rhombohedral phase field also becomes narrower as the temperature is increased.

The ΔG C curves for the low-temperature rhombohedral and antiferroelectric orthorhombic phases shown in Figure 1 were only drawn over the regions where these phases were stable. The compositional dependence of the antiferroelectric orthorhombic phase was determined by equating the energies of this phase with the high-temperature rhombohedral phase at the transition between these states (described in Reference 5). Since this transition only extends over a narrow compositional region, the above method will only apply over this region. Thus the energy of the antiferroelectric orthorhombic phase should only be calculated within this region.

In the case of the low-temperature rhombohedral phase the ΔG C can be calculated over a very small region into the adjacent phase fields, at which point either the spontaneous polarization becomes imaginary, or the low-temperature rhombohedral phase undergoes a metastable phase transition to the cubic state. At this point additional work needs to be conducted to more completely understand what is actually happening. This is particularly important in gaining a better understanding of the change in the spontaneous polarization from the high to low temperature rhombohedral phases, as will be discussed in more detail in the next section.

Calculating the ΔG C product of the ferroelectric orthorhombic phase provided an independent check on the values of the coefficients of the energy function. As shown in

Figure 1 this phase was found to be metastable across the phase diagram, indicating that the ratios of the coefficients are at least in the right range.

By plotting the composition versus temperature where the ΔG C products of the solutions cross, the phase diagram is obtained as shown in Figure 2. The data points are from the experimental phase diagram,[6] and the solid curves are from the theoretical calculations. The excellent agreement between the experimental data and theoretical calculations is to be expected, because the data was used to determine values of the coefficients in such a way as to cause the energies of the adjacent phases of a transition to be equal at the transition. However, this agreement shows that the energy function and values of the coefficients that have been determined will quantitatively model all of the known phase transitions of the PZT solid solution system.

The inflection point in the transition temperature T_C between the cubic and high-temperature rhombohedral phases near the PZT 90/10 composition (see Figure 2) appears to be due to the tricritical behavior. The Curie-Weiss temperature T_0 should form a continuous function with a continuous slope across the phase diagram, because it is determined from the cubic phase. In the second-order region T_C is equal to T_0, but in the first-order regions T_0 becomes less than T_C. The $T_C - T_0$ difference increases very quickly over a narrow compositional region, from zero at the tricritical point to 42 °C for lead zirconate (see Figure 9 in Reference 2). This therefore provides an explanation for the inflection point in T_C near the PZT 90/10 composition.

A question now arises as to why a similar change in T_C is not seen at the second tricritical point near the PZT 28/72 composition. This may be because the $T_C - T_0$ difference only changes from zero at the tricritical point to 13.4 °C for lead titanate, and this smaller change occurs over a much wider compositional range. In addition there is not enough T_C data on the phase diagram in this region to really be able to notice this type of change in T_C. Additional high-temperature x-ray diffraction work is needed to more precisely locate the second tricritical point. In the process of this work it would be interesting to try and see if

T_C does change in a similar (but smaller) way as occurs on the lead zirconate side.

III. SPONTANEOUS POLARIZATION AND TILT ANGLE

Figure 3 shows the calculated spontaneous polarization plotted versus temperature for five tetragonal PZT compositions. The first order transitions of the $PbTiO_3$ and PZT 20/80 compositions can be seen by the discontinuous changes in the polarization at T_C. The other three compositions have second order transitions causing the polarization to change continuously at T_C. The dielectric stiffness coefficient α_{11} changes sign at a tricritical point between the PZT 20/80 and 30/70 compositions causing the transition to change from first to second order. This tricritical point was estimated to occur at the PZT 28/72 composition from an extrapolation in Reference 2.

The calculated spontaneous polarization data shown in Figure 3 are in good agreement with the available experimental data. The value of 0.75 C/m^2 at 25 °C for lead titanate is equal to Gavrilyachenko et als.[7] experimental single-crystal measurement. The polarization values for the PZT 40/60 composition are slightly larger than the single-crystal measurements from 25 to 200 °C of Tsuzuki et al.[8] They commented that the polarization was not completely saturated in their hysteresis loops, which would result in lower values of the polarization. The close agreement between the calculated polarization and experimental measurements indicates that the proper values of the electrostrictive constants were.

The spontaneous polarization of four rhombohedral compositions with the high to low temperature rhombohedral phase transition is plotted versus temperature in Figure 4. The resultant polarization ($= 3^{1/2} P_3$) along the [111] direction was plotted in this figure. The small first order change in the polarization of the PZT 90/10 composition at the high-temperature rhombohedral to cubic transition (T_C) can be seen in Figure 4 (a). The other three compositions [Figures 4 (b) - (d)] all have a second order transition at T_C. This is because the fourth order rhombohedral dielectric stiffness ($\alpha_{11} + \alpha_{12}$) is slightly

negative for the PZT 90/10 composition, and then changes sign at a tricritical point (close to PZT 90/10) and becomes positive for the other three compositions.

The high to low temperature rhombohedral phase transition is first order for all compositions, as can be seen in Figure 4 by the discontinuous change in the polarization at this transition. This discontinuous change in the polarization increases from PZT 90/10 to 80/20, but then decreases as the titanium content is increased further, and becomes very small for the PZT 60/40 composition. This may explain why Zhuang et al.[9] found from pyroelectric measurements that the polarization only slightly changes through the high to low temperature rhombohedral transition for the PZT 70/30 and 60/40 compositions, but a large change occurs for the PZT 90/10 and 94/6 compositions.

The spontaneous polarization data for the PZT 90/10 composition [Figure 4 (a)] is in fairly good agreement with the single-crystal measurements by Clarke and Glazer.[10] Some of their experimental data in the high-temperature rhombohedral region was used to determine the electrostrictive Q_{44} constant for this composition, and thus good agreement occurs in this region. However, their data showed a decrease in the polarization on cooling in the high-temperature rhombohedral state close to the transition to the low-temperature phase, possibly due to a leakage of charge during their measurements. In this region the theoretically calculated polarization continues to increase as the temperature is decreased.

The spontaneous tilt angle was also calculated versus temperature for several compositions as shown in Figure 5. The resultant tilt angle about the cubic [111] direction $(= 3^{1/2} \theta_3)$ was plotted. The data points are the only available experimental values of the tilt angle, and were determined from neutron diffraction by Glazer et al.[11] and Amin et al.[12] These data were used in determining values for two of the coefficients (see Reference 4), and thus the theory and experimental data should agree. The theoretical calculations can be used to determine values of the tilt angle at other compositions and temperatures, as shown in this figure.

The spontaneous tilt angle was also plotted in Figure 6 versus composition at several different temperatures. The curve labeled θ_L represents the tilt angle at the high to low temperature rhombohedral transition (T_R). The discontinuity in the slope of the curves at the PZT 85/15 composition occurs due to the relations that was used to fit T_R [Equation (8) in Reference 4].

Figures 4 and 5 show that the spontaneous polarization and tilt angle increase very quickly after transforming to the low-temperature rhombohedral phase, especially the compositions with greater titanium content. This may indicate a limitation of the present theory. For the PZT 70/30 and 60/40 compositions the discontinuous change in the polarization at the high to low temperature rhombohedral transition is very small compared to the sudden increase in polarization that occurs just below the transition. This increase in polarization in the low-temperature rhombohedral phase is even more noticeable when the polarization is plotted versus composition at different temperatures as shown in Figure 7. If the spontaneous polarization as a function composition does actually increase in the low-temperature rhombohedral phase as much as is shown in this figure, then it seems that the previous experimental measurements of the polarization on ceramic samples would have found a similar effect.

The polarization should increase going to the low-temperature rhombohedral phase, but the increase calculated from this theory seems to be too large. Two possible explanations of this large increase in polarization in the low-temperature rhombohedral phase will now be described.

The first possibility is that this large increase may actually occur, and that the previous measurements on ceramic samples missed this effect, because not enough measurements were made. The effect of the morphotropic boundary on the ceramic data, where a coexistence of tetragonal and rhombohedral phases occurs, may have also made it more difficult to measure the polarization in the narrow region where the high-temperature rhombohedral phase is stable. Additional polarization measurements on homogeneous

888

ceramic samples would be useful in trying to see how the polarization changes in this region.

The second possibility, which seems more likely, is that the present theory does not adequately model the spontaneous polarization in the low-temperature rhombohedral phase for the compositions with greater titanium content. This could be due to the assumptions made in determining the coefficients. For example, the Q_{44} and R_{44} constants were assumed to be independent of composition and temperature in the low-temperature rhombohedral phase. The values of these constants were determined at the PZT 90/10 composition, and then used for the other compositions. The calculated polarization in the low-temperature rhombohedral phase of the PZT 90/10 composition does not have the large increase that occurs in the PZT 70/30 and 60/40 compositions. Therefore, it seems likely that the Q_{44} and R_{44} constants are dependent on composition, and if this was accounted for the large increase in polarization in the PZT 70/30 and 60/40 compositions would be decreased. However, at this time there is not enough experimental data available in the literature to determine these compositional dependences. Additional tilt angle data obtained from neutron diffraction would possibly solve this problem.

Another significant change could be made to the present theory by adding a temperature dependence to the second-order tilt angle related coefficient (β_1), and/or a sixth-order tilt angle term. Again the problem with this is that there is not enough data to properly determine all of these coefficients. The addition of a sixth-order tilt angle term will also greatly complicate the theory, because the equations for the spontaneous polarization and tilt angle in the low-temperature rhombohedral phase will change form quadratic to quartic.

The above discussion has shown that there may be some limitation to how well the present theory can quantitatively calculate the spontaneous polarization of the low-temperature rhombohedral phase for the compositions with greater titanium content. Due to the lack of tilt angle data and to avoid complicating the theory significantly more than it already is, the present theory is probably the best that it can be at this time, and is probably adequate for most applications.

IV. DIELECTRIC PROPERTIES

The calculated dielectric susceptibility coefficients of PZT 50/50 were plotted versus temperature in Figure 8. In comparison to the properties of $PbTiO_3$ (see Figure 8 in Reference 13), the dielectric susceptibilities and anisotropy have become much larger. The transition at T_C is also second order for PZT 50/50, while $PbTiO_3$ is first order. The second-order transition causes the dielectric susceptibility to go to infinity at T_C.

The compositional dependence of the dielectric susceptibility coefficients at 25 °C is plotted in Figure 9. A peak occurs in these coefficients at the PZT 50/50 composition due to the peak that formed in the Curie constant (see Figure 2 in Reference 3). The increase in dielectric anisotropy (η_{11}/η_{33}) that occurs from $PbTiO_3$ to the PZT 50/50 composition is due to the change in the ratios of the dielectric stiffness coefficients (α_{12}/α_{11}, $\alpha_{112}/\alpha_{111}$, and $\alpha_{123}/\alpha_{111}$) as a function of composition.

On the rhombohedral side of the peak the anisotropy decreases and η_{11}' eventually even becomes less than η_{33}'. This effect is at least partially due to compositional dependence of the ratios of the dielectric stiffness coefficients, but may also be due to an internal pressure that may develop within the perovskite structure when a larger zirconium ion is replaced by the smaller titanium ion. Amin et al.[14] showed that for the PZT 50/50 composition the application of hydrostatic stress would cause the anisotropy to decrease, and thus this might partially account for the small dielectric anisotropy on the $PbZrO_3$ side on the PZT system. Using the present theory of PZT the effect of mechanical boundary conditions on the properties and phase stability should now be investigated in more detail across the entire PZT system.

The dielectric susceptibility coefficients of two rhombohedral compositions, PZT 60/40 and 90/10, were plotted versus temperature in Figures 10 and 11. A similar change in the behavior of the dielectric anisotropy occurs from PZT 60/40 to 90/10 as occurred from PZT 50/50 to $PbTiO_3$. For PZT 90/10 and $PbTiO_3$ (see Figure 8 in Reference 13) the dielectric susceptibility parallel to the polar axis (η_{33} or η_{33}') is larger than the perpendicular

susceptibility (η_{11} or η_{11}') at high temperatures, but smaller at low temperatures.

At high temperatures close to T_C for rhombohedral compositions close to the morphotropic boundary (Ti content > 0.45) a problem develops when calculating the dielectric susceptibility coefficient η_{11}' using the coefficients from References 2 and 3. At a temperature below T_C the η_{11}' coefficient will increase to infinity, and then become negative between this temperature and T_C. This is simply due to the values of the coefficients used, and indicates that in this region these values are not quite right. Because of this problem, care should be taken in calculating the rhombohedral dielectric susceptibilities at high temperatures for compositions near the morphotropic boundary. Considering that all of the coefficients were assumed to be independent of temperature, except α_1, and that some of the coefficients were determined at T_C (232 - 492 °C) and others at 4.2 K, it is amazing that everything works as well as it does, and that more problems have not occurred.

Away from this region the calculated dielectric properties are in fairly good agreement with the available experimental data. Haun et al.[13] showed that the calculated dielectric susceptibility coefficients and anisotropy of $PbTiO_3$ were in good agreement with Fesenko et al.'s[15] experimental single-crystal data at low temperatures, where the defect contributions to the experimental measurements had "frozen out". The theoretically calculated dielectric properties near the morphotropic boundary have similar values as the experimental measurements on single crystals by Tsuzuki et al.[8] Good agreement was also found between the calculated dielectric properties and Clarke and Whatmore's[16] PZT 90/10 single-crystal measurements.

V. PIEZOELECTRIC PROPERTIES

The calculated piezoelectric voltage coefficients g_{ij} (assumed to be equal to the b_{ij} coefficients) for the PZT 50/50, 60/40, and 90/10 compositions were plotted versus temperature in Figures (12) - (14). The g_{ij} coefficients plotted in these figures are based on

the cubic axes. Thus the x_3 axis is along the polar axis for the tetragonal coefficients, but not for the rhombohedral coefficients.

Since the electrostrictive constants were assumed to be independent of temperature, the negative temperature dependence of the g_{ij} coefficients was caused by the temperature dependence of the spontaneous polarization. The PZT 90/10 composition has a first-order change in the spontaneous polarization, which causes discontinuities in the g_{ij} coefficients at T_C. The PZT 50/50 and 60/40 compositions undergo second order transitions, and thus the g_{ij} coefficients change continuously from a value of zero at T_C.

The compositional dependence of the g_{ij} coefficients at 25 °C is plotted in Figure 15 Since the electrostrictive constants were given a compositional dependence (see Figure 2 in Reference 17), the compositional dependence of the g_{ij} coefficients depends on the electrostrictive constants and the spontaneous polarization (see Figure 7). The result is that the g_{ij} coefficients change with composition as shown in Figure 15. The compositional dependences of the g_{ij} coefficients are much smaller than that of the d_{ij} coefficients, which will be presented next.

The piezoelectric charge coefficients d_{ij} of the PZT 50/50 composition were plotted versus temperature in Figure 16. The positive temperature dependence of the d_{ij} coefficients was caused by the strong temperature dependence of the dielectric susceptibility coefficients. In Figure 17 the d_{ij} coefficients are plotted versus composition at 25 °C, showing the large peak in these coefficients near the morphotropic boundary. The large increase of the η_{11} coefficient from $PbTiO_3$ to the PZT 50/50 composition (see Figure 9) caused a large increase to also occur in the d_{15} coefficient.

For the rhombohedral compositions the d_{ij} coefficients were calculated based on the original cubic axes, resulting in four independent nonzero coefficients. The relations for the rhombohedral coefficients are more complicated than those for the tetragonal coefficients, because two terms are involved in three of the four relations [see Equations (44) and (45) in Reference 1]. These two terms are often competing with one term being positive, while the

other is negative. In addition the η_{12} coefficient can be positive or negative depending on the composition and temperature.

The d_{ij} coefficients are plotted versus temperature for two rhombohedral compositions, PZT 60/40 and 90/10, in Figures 18 and 19. The d_{33} and d_{15} coefficients form similar shaped curves for both compositions, but the d_{31} and d_{14} coefficients have definite differences.

For the PZT 60/40 composition the d_{14} coefficient is negative at all temperatures, and becomes more negative with increasing temperature. The d_{14} coefficient of the PZT 90/10 composition is slightly negative at low temperatures, and then becomes positive at about -100 °C, and continues to increase with increasing temperature. These differences are due to the η_{12} coefficient, which is negative for the PZT 60/40 composition, and positive for the PZT 90/10 composition (except at low temperatures where it changes sign and becomes negative).

The d_{31} coefficient of the 60/40 composition is negative, and becomes more negative with increasing temperature. For the PZT 90/10 composition the d_{31} coefficient is negative at low temperatures, becomes more negative with increasing temperature, and then suddenly increases and becomes positive just below T_C. This behavior is due to the η_{12} coefficient, and also due to the two terms in the d_{31} relation, which are of opposite sign with one dominating at low temperatures and the other at high temperatures.

The rhombohedral d_{ij} coefficients described above are based on the original cubic axes. At this point what needs to be done in the future is to rotate the axes, so that the new x_3 axis is along the rhombohedral polar direction. This would reduce the number of independent nonzero coefficients to three (d_{33}, d_{31}, and d_{15}), similar to the tetragonal d_{ij} matrix, and thus simplify the analysis of these coefficients.

The calculated d_{ij} coefficients have similar values as the experimental ceramic data near the morphotropic boundary. The only available single-crystal data was measured by Gavrilyachenko and Fesenko[18] on lead titanate. Their data were compared with the

theoretical lead titanate calculations in Reference 13. Fairly good agreement was found, especially for the d_{31} coefficient.

VI. SUMMARY AND FUTURE APPLICATIONS OF THE THEORY OF PZT

The applications of compositions of the PZT solid solution system as piezoelectric transducers, pyroelectric detectors, electro-optic devices, and explosively induced charge storage devices were described in the first paper of this series to demonstrate the technological importance of PZT. These applications use PZT in polycrystalline ceramic form, and thus the properties of these ceramics are well established in the literature. However, the mechanisms contributing to these outstanding ceramic properties of PZT are not well understood, because of the complexity of the interactions within the ceramic.

A first step in the analysis of a ferroelectric ceramic material is to separate the intrinsic and extrinsic contributions to the properties. The intrinsic contributions result from the averaging of the single-domain single-crystal properties, while the extrinsic contributions arise from the interactions at grain or phase boundaries and from the domain wall or thermal defect motions. Unfortunately, due to the difficulty of growing good quality single crystals of PZT, very little single-crystal data is available. Thus the goal of this project was to develop a thermodynamic phenomenological theory to calculate the single-domain properties of PZT. This theory could then be used to separate the intrinsic and extrinsic contributions to the ceramic properties. In addition there are several other applications of this theory, which will be described later in this summary.

In the first paper of this series a modified elastic Gibbs free energy function was expanded in powers of the ferroelectric and antiferroelectric measures of the polarization. An additional order parameter was also included to account for the tilting of the oxygen octahedra in the low-temperature rhombohedral phase. The resulting energy function can be used to model the phase transitions and single-domain properties of the PZT system.

Solutions to this energy function were used to derive relations for the energies; spontaneous polarizations, strains, and tilt angles; and dielectric and piezoelectric properties corresponding to the different phases in the PZT system.

All of the coefficients of the energy function were assumed to be independent of temperature, except the ferroelectric and antiferroelectric dielectric stiffness coefficients α_1 and σ_1, which was given a linear temperature dependence based on the Curie-Weiss law. The experimental phase diagram was extensively used in the evaluation of the coefficients, by requiring that the energies of the adjacent phases of a phase transition to be equal at the transition. The first partial derivative stability conditions were also used as additional relations in the evaluation procedure.

Without single-crystal data, the development of this theory was complicated and involved indirect methods of determining the coefficients of the energy function. Additional experimental data were needed to determine the compositional dependence of the coefficients. A sol-gel procedure was used to prepare pure homogeneous PZT powders across the phase diagram to be used in collecting additional PZT data. The lattice constants versus temperature were determined from these powders from high-temperature x-ray diffraction, and used to calculate the spontaneous strain.[2,13,19] The sol-gel derived powders were also used to fabricate ceramic samples for dielectric, piezoelectric, elastic, pyroelectric, and electrostrictive measurements.[3,17,20,21,22] These data were very important in completing the evaluation of the coefficients of the energy function.

The compositional dependence of the cubic electrostrictive constants across the PZT system were determined from a combination of single crystal and ceramic data using series and parallel averaging relations (analogous to the Reuss and Voigt methods of averaging the elastic constants).[17] An interesting result of this work was that the electrostrictive constants form a peak at the PZT 50/50 composition. In addition, the ratios of the electrostrictive constants change with composition in such a way as to explain the compositional dependence of the electromechanical anisotropy found in PZT ceramics.[23] The electromechanical

anisotropy is very large in compositions near the end members $PbTiO_3$ and $PbZrO_3$, but becomes very small for compositions in the center of the phase diagram near the morphotropic phase boundary.

In the second paper of this series the electrostrictive data were used with the spontaneous strain data to calculate the spontaneous polarization, which was used to determine values of the higher-order dielectric stiffness coefficients. In the third paper of this series low-temperature ceramic dielectric data were particularly important in determining the compositional dependence of the Curie constant, and in separating the sixth-order polarization interaction coefficients (α_{112} and α_{123}). The tilt angle related coefficients were determined in the fourth paper of the series from spontaneous strain and tilt angle data. The compositional dependence of the antiferroelectric orthorhombic free energy was determined by combining data from a separate theory developed for $PbZrO_3$ with the requirement that the energies of the high-temperature rhombohedral and antiferroelectric orthorhombic phases must be equal at the transition between these phases.[5]

After determining values of the coefficients at several different compositions as described above, the compositional dependence of the coefficients was determined by fitting an equation to these values. A set of equations was then established that can be used to calculate values of the coefficients at any composition.

Using these equations the phase stability, spontaneous polarization and tilt angle, and dielectric and piezoelectric properties were calculated. The theoretically calculated phase diagram was shown to quantitatively model the experimental phase diagram. An independent check of the coefficients was also made by calculating the free energy of the ferroelectric orthorhombic state, which showed that this phase was metastable across the phase diagram as experimentally expected. The spontaneous polarization and tilt angle were calculated for several compositions across the phase diagram. These calculations were in good agreement with the available experimental single-crystal data. The dielectric and piezoelectric properties were also calculated and found to be in good agreement with the experimental data. As a

summary of these calculations the theoretical properties of PZT at 25°C are listed in Table I.

Some limitations of the present theory were found. Due to the lack of experimental data for the low-temperature rhombohedral phase, especially tilt angle data, some assumptions were necessary in determining the compositional dependence of the tilt angle related coefficients. In addition these coefficients were assumed to be independent of temperature, and only tilt angle terms up to the fourth power were included. With these assumptions the calculations of the spontaneous polarization, tilt angle, and dielectric properties were still in fairly good agreement with the experimental single-crystal data at the PZT 90/10 composition.

The problems developed in the calculations for compositions with greater titanium content. The spontaneous polarization calculated in the low-temperature rhombohedral phase for the PZT 70/30 and 60/40 compositions increased more than would be expected. Another problem was found when calculating the dielectric susceptibility (negative values resulted) in the high-temperature rhombohedral phase at temperatures near T_C and at compositions close to the morphotropic boundary. However, away from this small region the dielectric properties could be calculated with good agreement with the available experimental data.

The present theory could be improved as additional experimental data becomes available. In particular, additional spontaneous strain data on very homogeneous powders are needed to more precisely locate the tricritical point on the lead titanate side of the phase diagram. Strain data on compositions close to lead zirconate are also needed to determine the compositional dependence of the antiferroelectric related coefficients. As described above additional tilt angle data are needed to more accurately determine the tilt angle related coefficients.

In this series of papers a single energy function and set of coefficients was presented that can be used to model all of the known phase transitions in the PZT solid solution system. This theory can also be used to calculate the single domain properties of PZT. In addition to the properties calculated in this thesis, the theory can be used to calculate the

elastic compliances at constant field, the dielectric susceptibilities at constant strain (the dielectric susceptibilities calculated in this paper were at constant stress), and thermal properties such as the entropy change and latent heat at a transition.[26,27] This theory can now be used for several different applications.

One application that this theory has already been used for was to help explain the large electromechanical anisotropy that occurs in $PbTiO_3$ ceramics, but not in the single crystal properties. By averaging the single-crystal constants obtained from this theory, a large electromechanical anisotropy was found to occur due to the particular values of the single-crystal electrostrictive ratios of $PbTiO_3$.[23] Other compositions in ceramic form, such as PZT 50/50, have small electromechanical anisotropy, because the values of the single crystal electrostrictive ratios have changed.

The intrinsic and extrinsic contributions to the properties of polycrystalline PZT ceramics can now be separated with the results of this theory. By using simple averaging relations the intrinsic contributions to the ceramic properties can be calculated from the theoretical single-domain properties. By then comparing these properties with the experimental measurements on ceramic samples, the extrinsic contributions can be determined. Comparisons with low-temperature and high-frequency measurements on ceramics will be particularly useful in seeing where these extrinsic contributions "freeze out" at low temperature and "relax out" at high frequencies. After separating the extrinsic contributions, comparisons of these results should be made with the calculations from other theories, such as that by Arlt and Peusens,[28] where the domain wall contributions to the dielectric constant of $BaTiO_3$ ceramics were calculated.

This theory can also be used to study the effects of electrical and mechanical boundary conditions on the properties and phase stability, which should also lead to a better understanding of ferroelectric polycrystalline materials where the boundary conditions may vary from grain to grain. Amin et al.[14,29] did study these effects using the earlier phenomenological theory that was developed for the morphotropic phase boundary region.[30]

They found that the application of an electric field would easily transform the rhombohedral state to the tetragonal state, but that by applying a field to the tetragonal state would not transform it to the rhombohedral state. They then concluded "that this may be part of the reason there is a rapid escalation of coercivity against poling in the tetragonal phase compositions." Amin et al.[14] also studied the effect of hydrostatic pressure on the properties and phase stability, and found that for morphotropic boundary compositions the rhombohedral phase can easily be transformed to the tetragonal phase from hydrostatic pressure. Additional studies of the effects of electrical and mechanical boundary conditions should now be continued using the more complete theory of PZT that has now been developed.

The energy function developed for PZT was based on the elastic Gibbs free energy, which resulted in dielectric stiffness coefficients under constant stress conditions. If the Helmholtz free energy had been used, then the dielectric stiffness coefficients would be under constant strain conditions. The fourth-order dielectric stiffness coefficients from these two energy functions can be related through terms involving the electrostrictive and elastic constants.[26,31] Since the fourth-order dielectric stiffness coefficients changed signs and caused the tricritical behavior to occur, it would now be useful to compare these coefficients with the coefficients from the Helmoltz function to see if the tricritical behavior is due to the electrostrictive coupling, or due to the intrinsic behavior of the material. Also by comparing the coefficients of these energy functions additional understanding of the phase stability may be gained.

With the phenomenological theory now developed for the PZT system extensions into more complex systems, such as lanthanum modified PZT (PLZT), can now be started. This should be very important, because for most technological applications PZT is modified with other ions. Extending the PZT theory into the PLZT system should also be useful in furthering the understanding relaxor type ferroelectric materials.

In addition to the applications described above, the phenomenological theory of PZT will provide a method of collecting all of the dielectric, piezoelectric, elastic, and thermal data into an organized and easily tractable form.

REFERENCES

[1] M. J. Haun, E. Furman, S. J. Jang, and L. E. Cross, "Thermodynamic Theory of the Lead Zirconate-Titanate Solid Solution System, Part I: Phenomenology," J. Appl. Phys. (submitted).

[2] M. J. Haun, E. Furman, H. A. McKinstry, and L. E. Cross, "Thermodynamic Theory of the Lead Zirconate-Titanate Solid Solution System, Part II: Tricritical Behavior," J. Appl. Phys. (submitted).

[3] M. J. Haun, Z. Q. Zhuang, E. Furman, S. J. Jang, and L. E. Cross, "Thermodynamic Theory of the Lead Zirconate-Titanate Solid Solution System, Part III: Curie Constant and Sixth-Order Polarization Interaction Dielectric Stiffness Coefficients," J. Appl. Phys. (submitted).

[4] M. J. Haun, E. Furman, T. R. Halemane, and L. E. Cross, "Thermodynamic Theory of the Lead Zirconate-Titanate Solid Solution System, Part IV: Tilting of the Oxygen Octahedra," J. Appl. Phys. (submitted).

[5] M. J. Haun, T. J. Harvin, M. T. Lanagan, Z. Q. Zhuang, S. J. Jang, and L. E. Cross, "Thermodynamic Theory of $PbZrO_3$," J. Appl. Phys. (to be submitted).

[6] B. Jaffe, W. J. Cook, and H. Jaffe, *Piezoelectric Ceramics* (Academic Press, London, 1971).

[7] V. G. Gavrilyachenko, R. I. Spinko, M. A. Martynenko, and E. G. Fesenko, Fiz. Tved. Tela 12, 1532 (1970) [Sov. Phys.-Solid State 12, 1203 (1970)].

[8] H. Tsuzuki, K. Sakata, and M. Wada, Ferroelectrics 8, 501 (1974).

[9] Z. Q. Zhuang, M. J. Haun, A. Bhalla, S. J. Jang, and L. E. Cross, unpublished data.

[10] R. Clarke and A. M. Glazer, Ferroelectrics 12, 207 (1976).

[11] A. M. Glazer, S. A. Mabud, and R. Clarke, Acta Cryst., B34, 1060 (1978).

[12] A. Amin, R. E. Newham, and L. E. Cross, J. Solid State Chemistry 37, 248 (1981).

[13] M. J. Haun, E. Furman, S. J. Jang, H. A. McKinstry, and L. E. Cross, J. Appl. Phys., 62, 333 (1987).

[14] A. Amin, R. E. Newham, and L. E. Cross, Phys. Rev. B 34, 1595 (1986).

[15] E. G. Fesenko, V. G. Gavrilyachenko, E. V. Zarochentsev, Izv. Akad. Nauk SSSR Ser. Fiz. 34, 2541 (1970) [Bull. Acad. Sci. USSR 34, 2262 (1970)].

[16] R. Clarke, and R. W. Whatmore, J. of Crystal Growth, 33, 29 (1976).

[17] M. J. Haun, Z. Q. Zhuang, E. Furman, S. J. Jang, and L. E. Cross, Am. Ceram Soc. (submitted).

[18] V. G. Gavrilyachenko and E. G. Fesenko, Kristallografiya 16, 640 (1971) [Sov. Phys.-Crystallogr. 16, 549 (1971)].

[19] M. J. Haun, Y. H. Lee, H. A. McKinstry, and L. E. Cross, *Advances in X-ray Analysis, Vol. 30*, edited by C. S. Barrett, J. V. Gilfrich, R. Jenkins, D. E. Leyden, J. C. Russ, and P. K. Predecki, (Plenum Press, New York, 1987) pp. 473-481.

[20] Z. Q. Zhuang, M. J. Haun, S. J. Jang, and L. E. Cross, *Proceedings of the 6th IEEE International Symposium on the Applications of Ferroelectrics*, Lehigh, PA, edited by Van Wood (IEEE, New York, 1986) pp. 394-397.

[21] Z. Q. Zhuang, M. J. Haun, S. J. Jang, and L. E. Cross, Amer. Ceram. Soc. (to be published).

[22] Z. Q. Zhuang, M. J. Haun, A. Bhalla, S. J. Jang, and L. E. Cross, unpublished data.

[23] M. J. Haun, E. Furman, S. J. Jang, and L. E. Cross, Trans. IEEE Ultrasonics, Ferroelectrics and Frequency Control Soc., (to be published).

[24] R. W. Whatmore, R. W., R. Clarke, and A. M. Glazer, J. Phys. C: Solid State Phys., 11, 3089 (1978).

[25] M. J. Haun, Z. Q. Zhuang, S. J. Jang, H. A. McKinstry, and L. E. Cross, *Proceedings of the 6th IEEE International Symposium on the Applications of Ferroelectrics*, Lehigh, PA, edited by Van Wood (IEEE, New York, 1986) pp. 398-401.

[26] A. F. Devonshire, Phil. Mag., 42, 1065 (1951).

[27] E. Fatuzzo and W. J. Merz, *Ferroelectricity* (Wiley, New York, 1967).

[28]G. Arlt and H. Peusens, Ferroelectrics 48, 213 (1983).

[29]A. Amin and L. E. Cross, Jpn. J. Appl. Phys. 24 (Suppl. 24-2), 229 (1985).

[30]A. Amin, M. J. Haun, B. Badger, H. A. McKinstry, and L. E. Cross, Ferroelectrics, 65, 107 (1985).

[31]A. F. Devonshire, Phil. Mag. 40, 1040 (1949).

LIST OF FIGURES AND TABLES

Table I. The Theoretical Properties of PZT at 25 °C.

	Mole Fraction PbTiO$_3$ in PZT[*]									
	0.1	0.2	0.3	0.4	0.5	0.6	0.7	0.8	0.9	1.0
P_S (C/m^2)	0.57	0.66	0.65	0.50	0.50	0.57	0.64	0.70	0.74	0.75
θ_S (Deg.)	5.42	7.36	6.64	—	—	—	—	—	—	—
η_{33} or η_{33}'	219.	277.	280.	295.	382.	197.	116.	86.4	72.9	66.6
η_{11} or η_{11}'	195.	262.	360.	529.	1721.	498.	218.	143.	121.	124.
g_{33} (10^{-3} Vm/N)	26.8	30.9	34.6	41.9	96.6	92.9	101.	114.	124.	134.
g_{31} (10^{-3} Vm/N)	-8.13	-9.53	-11.2	-15.6	-46.0	-33.8	-31.8	-34.2	-37.1	-39.2
g_{15} (10^{-3} Vm/N)	12.9	14.3	15.5	18.1	41.0	38.4	40.8	44.9	48.6	50.9
d_{33} (10^{-12} C/N)	47.2	72.1	107.	189.	327.	162.	104.	87.2	81.2	79.2
d_{31} (10^{-12} C/N)	-13.3	-21.6	-38.5	-80.5	-156.	-58.9	-32.6	-26.2	-23.9	-23.1
d_{14} (10^{-12} C/N)	1.81	1.27	-7.26	-25.1	—	—	—	—	—	—
d_{15} (10^{-12} C/N)	24.2	34.5	42.0	60.0	624.	169.	78.6	57.0	52.1	56.1

[*]The values listed from 0.1 to 0.4 were calculated from the high-temperature rhombohedral equations, except for P_S and θ_S from 0.1 to 0.3 which were calculated from the low-temperature rhombohedral equations. The values listed from 0.5 to 1.0 were calculated from the tetragonal equations. $P_S = P_3$ in the tetragonal state, but $P_S = 3^{1/2} P_3$ in the rhombohedral states. $\theta_S = 3^{1/2} \theta_3$. η_{11} and η_{33} were used in the tetragonal state, and η_{11}' and η_{33}' (see Section 2.5) were used in the rhombohedral state. The piezoelectric coefficients are all based on the cubic axes.
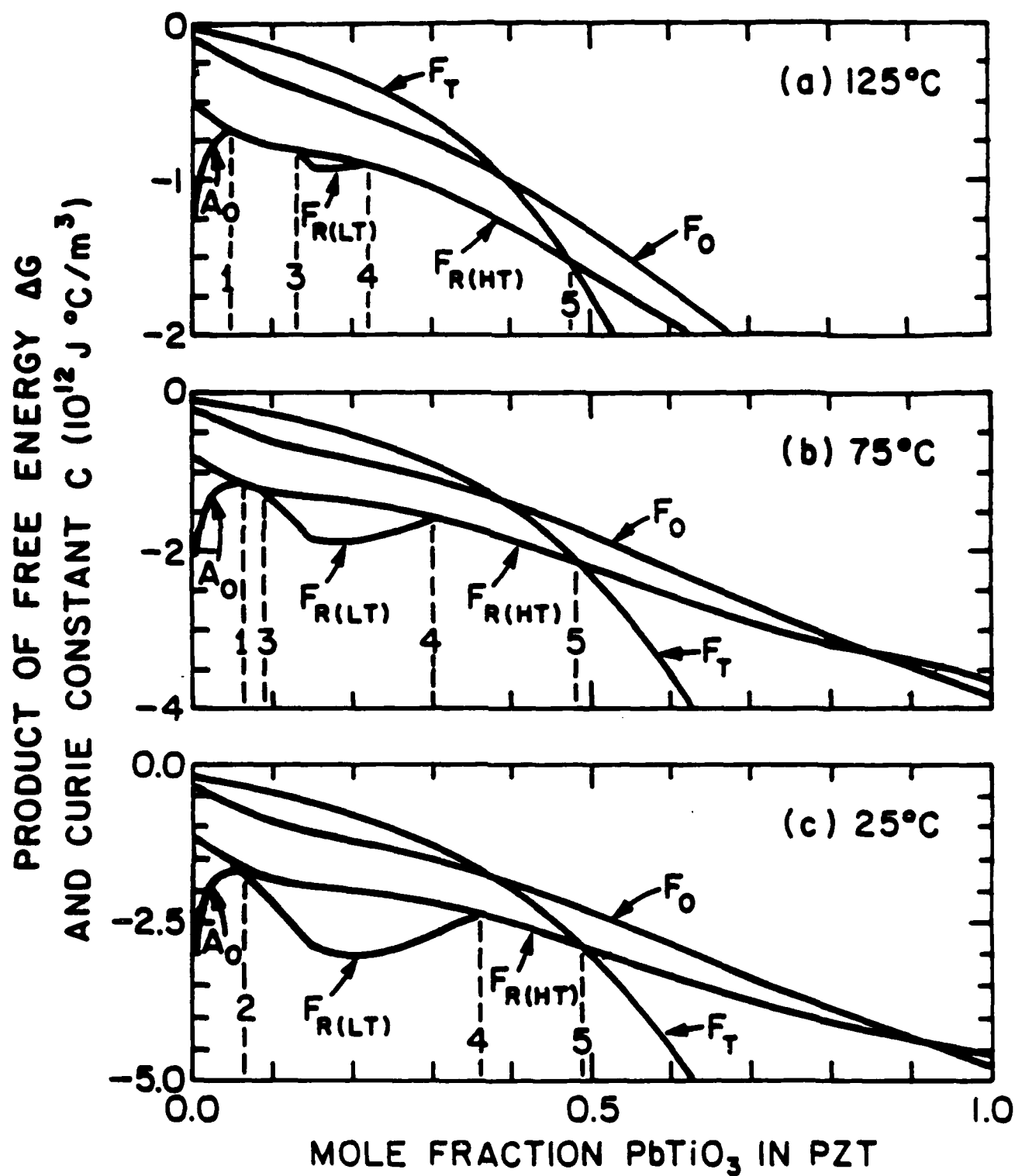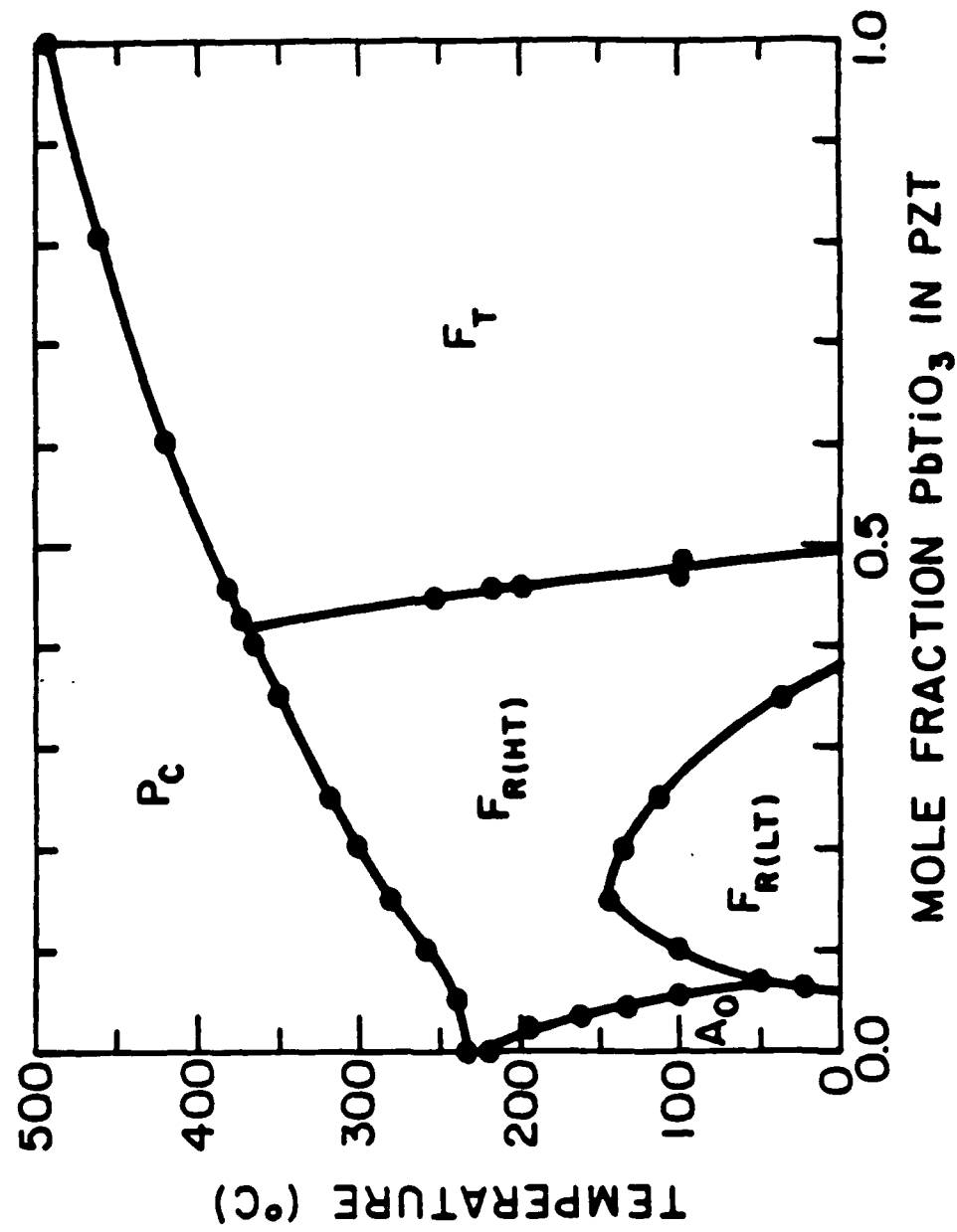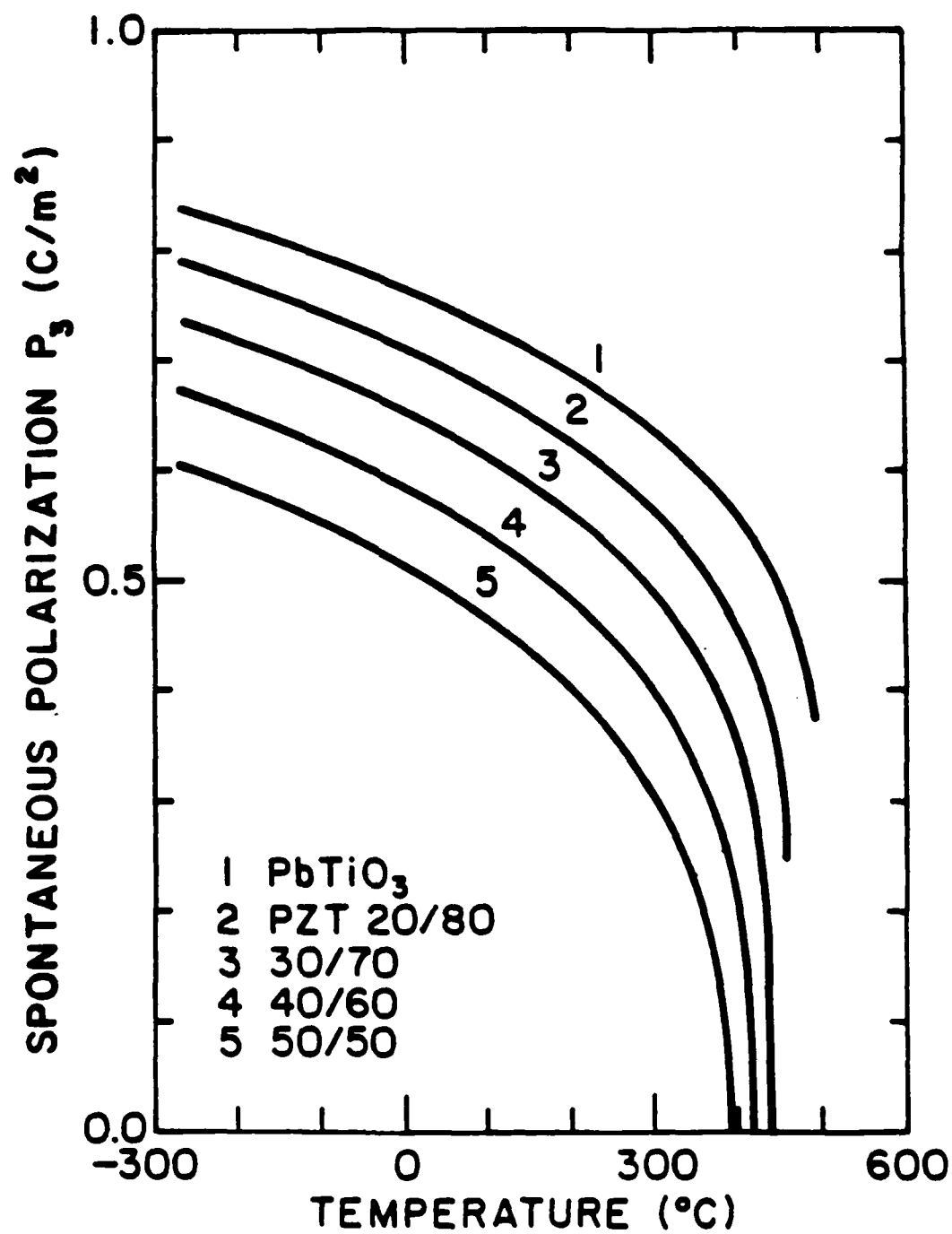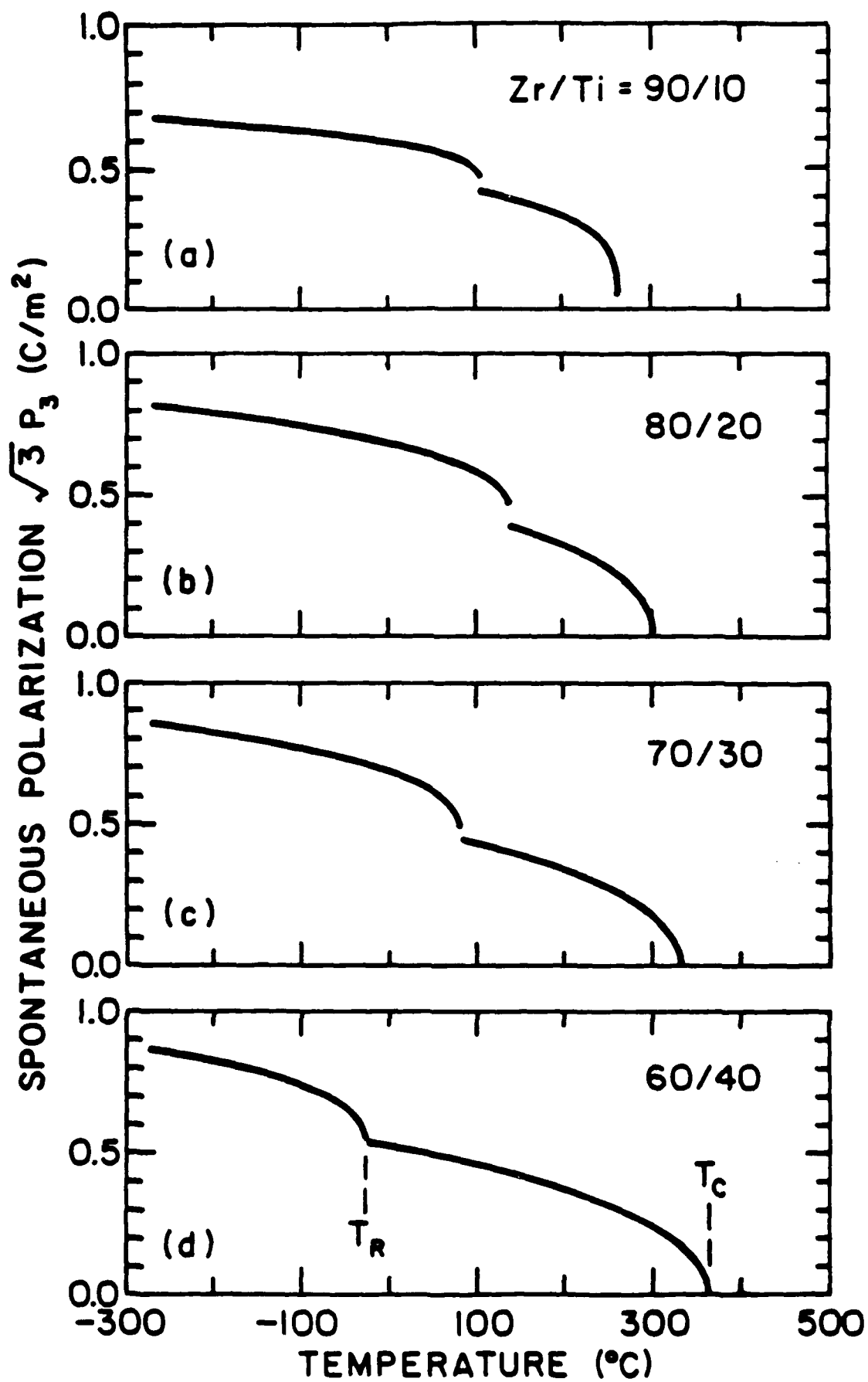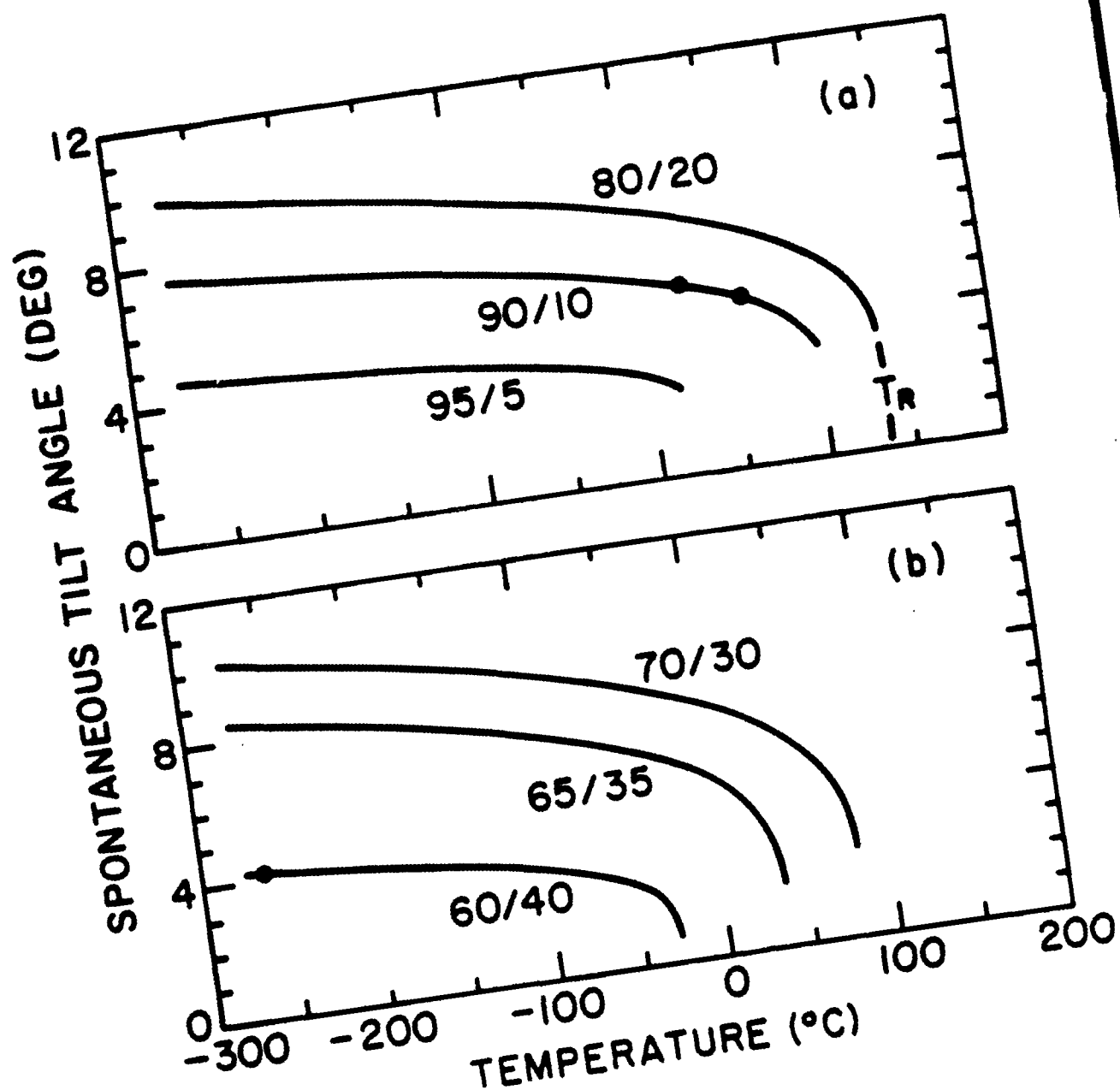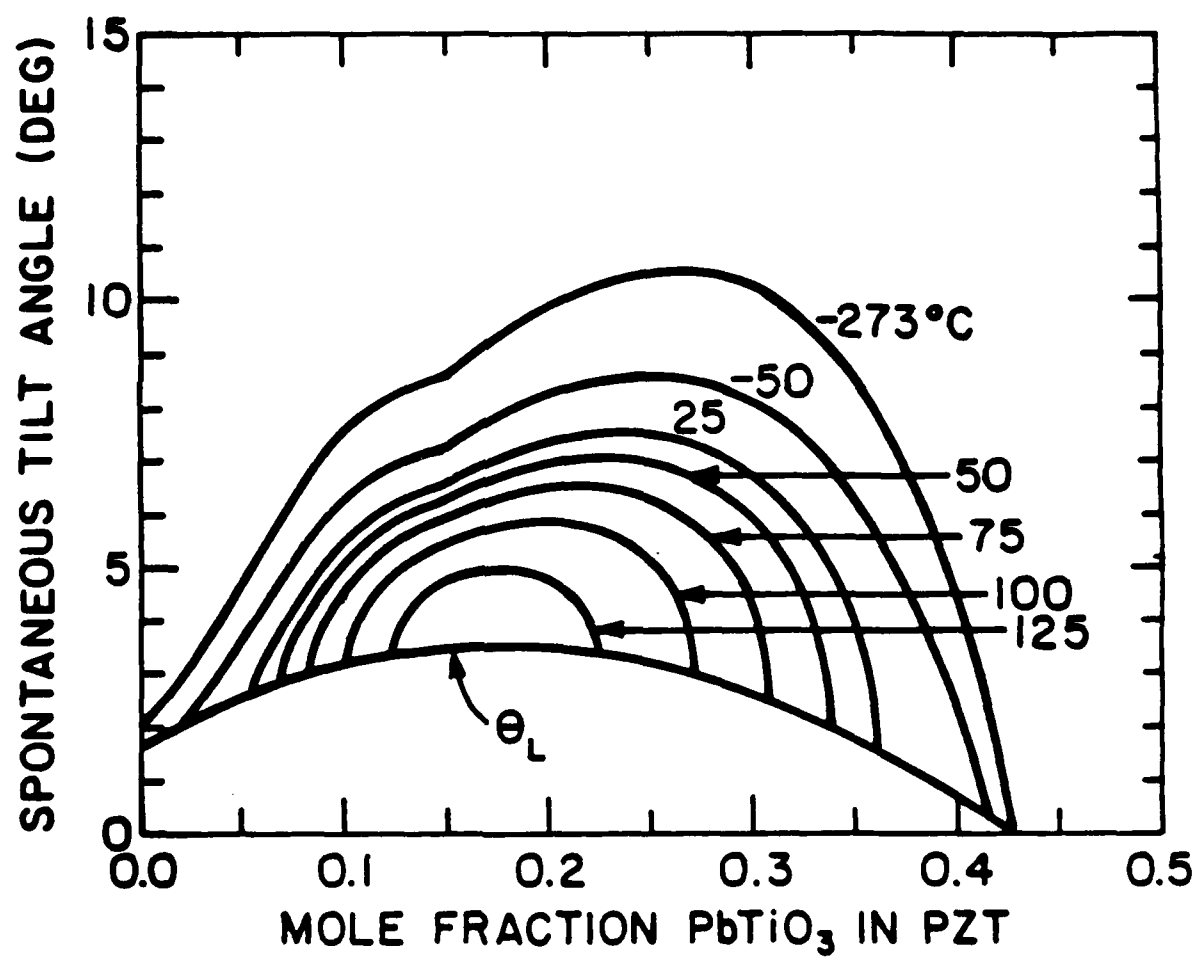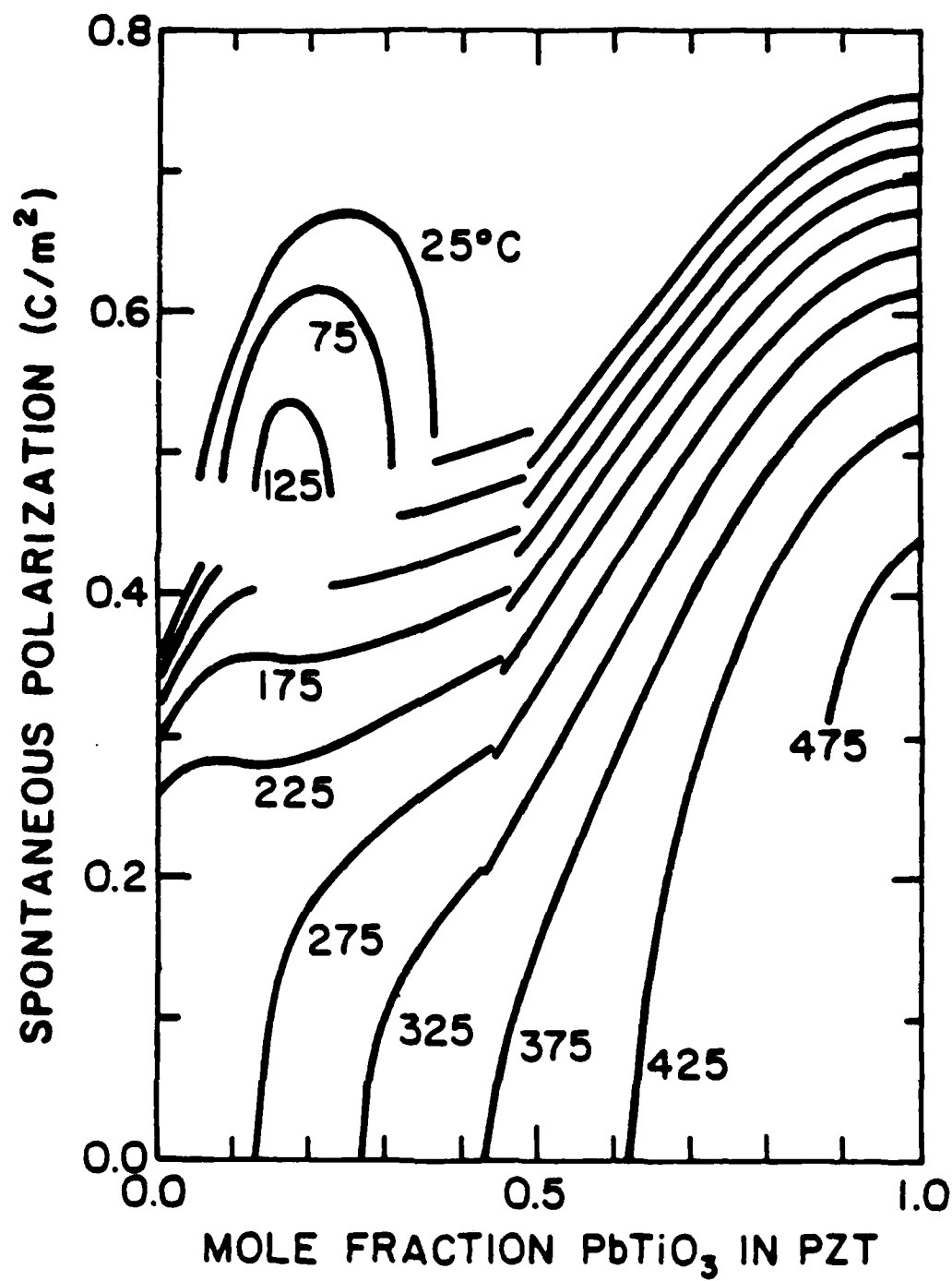
Fig. 1

Fig. 2

Fig. 3

Fig. 4

Fig. 5

Fig. 6

Fig. 7
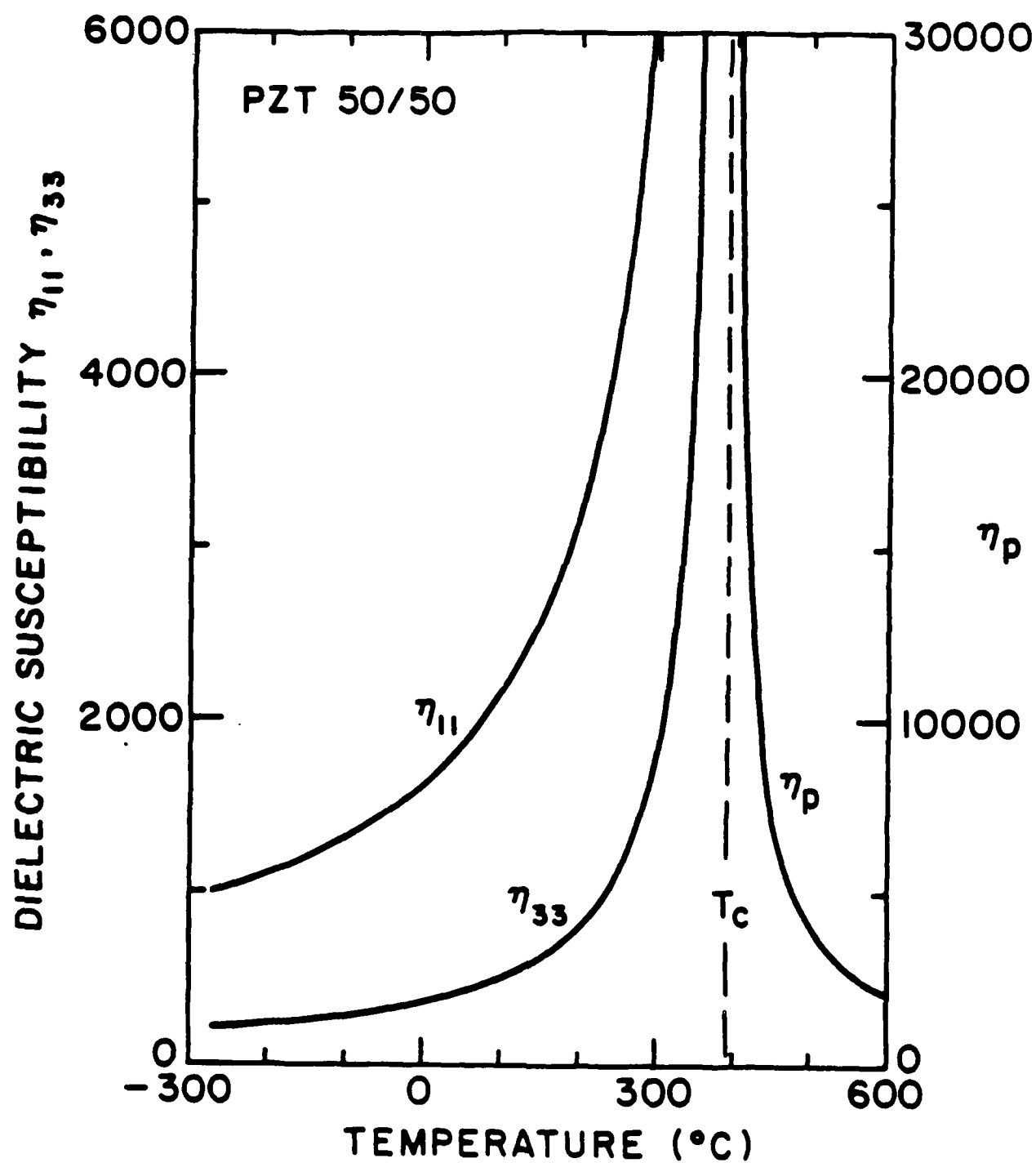
Fig. 8
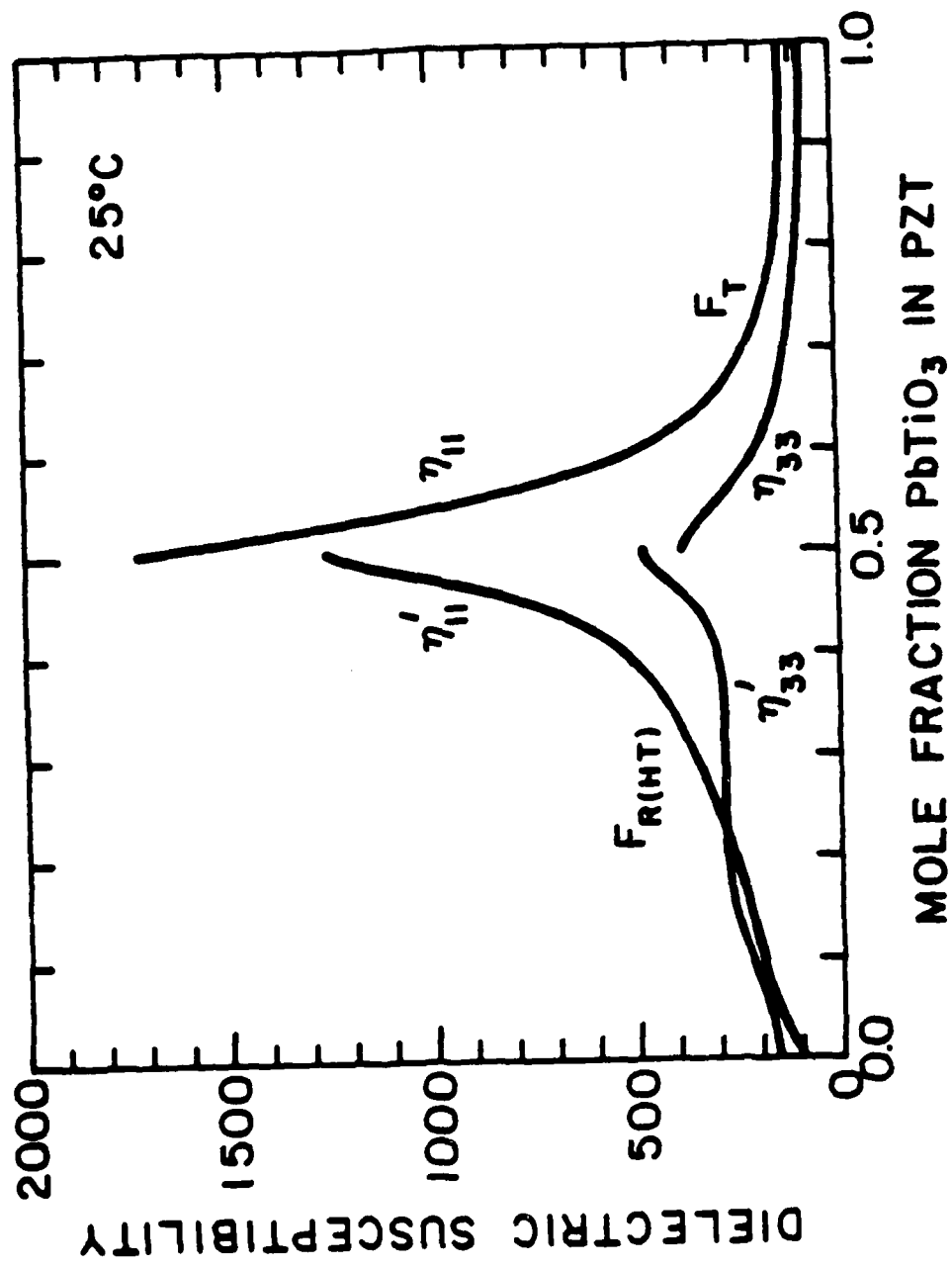
Fig. 9
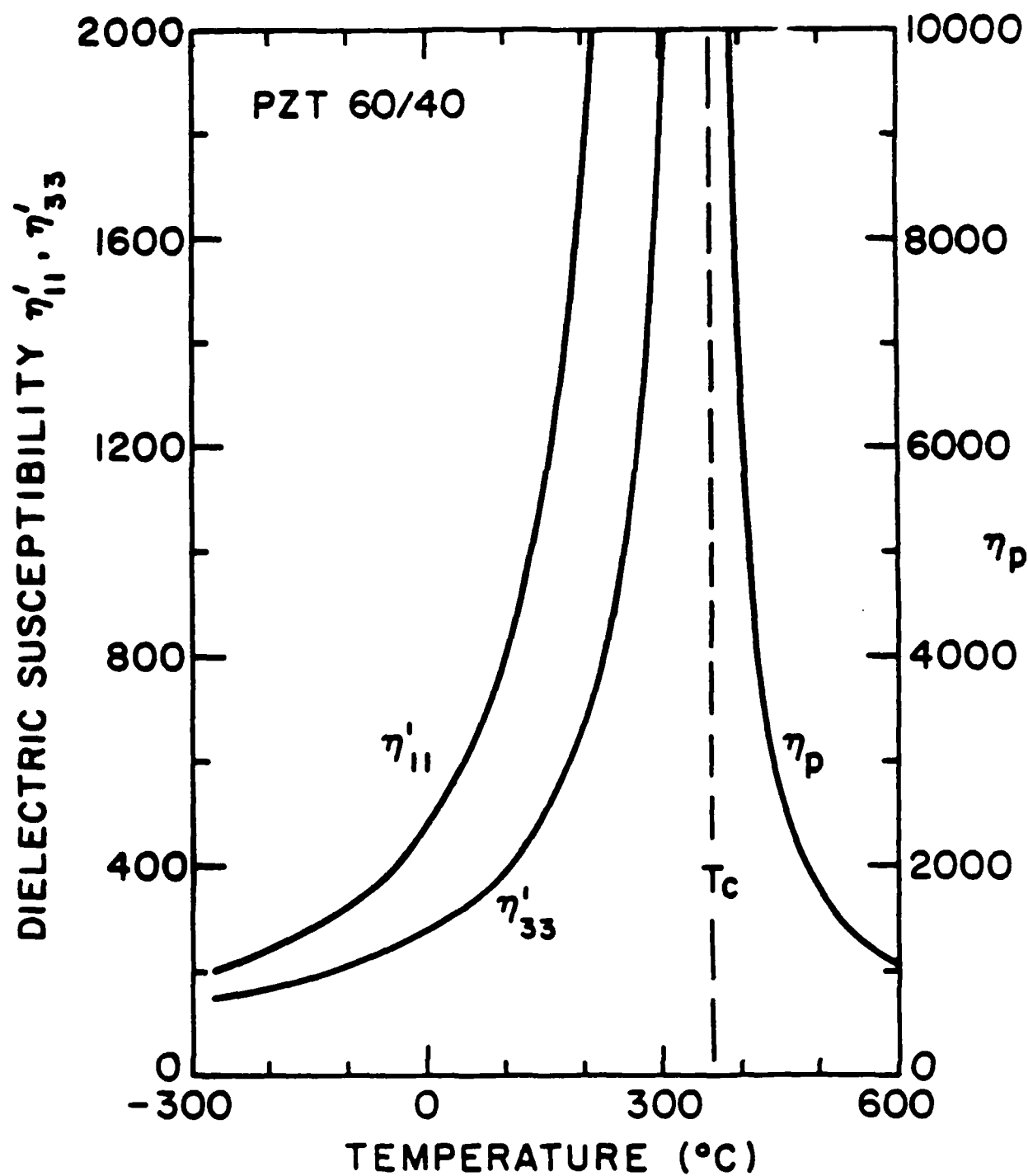
Fig. 10
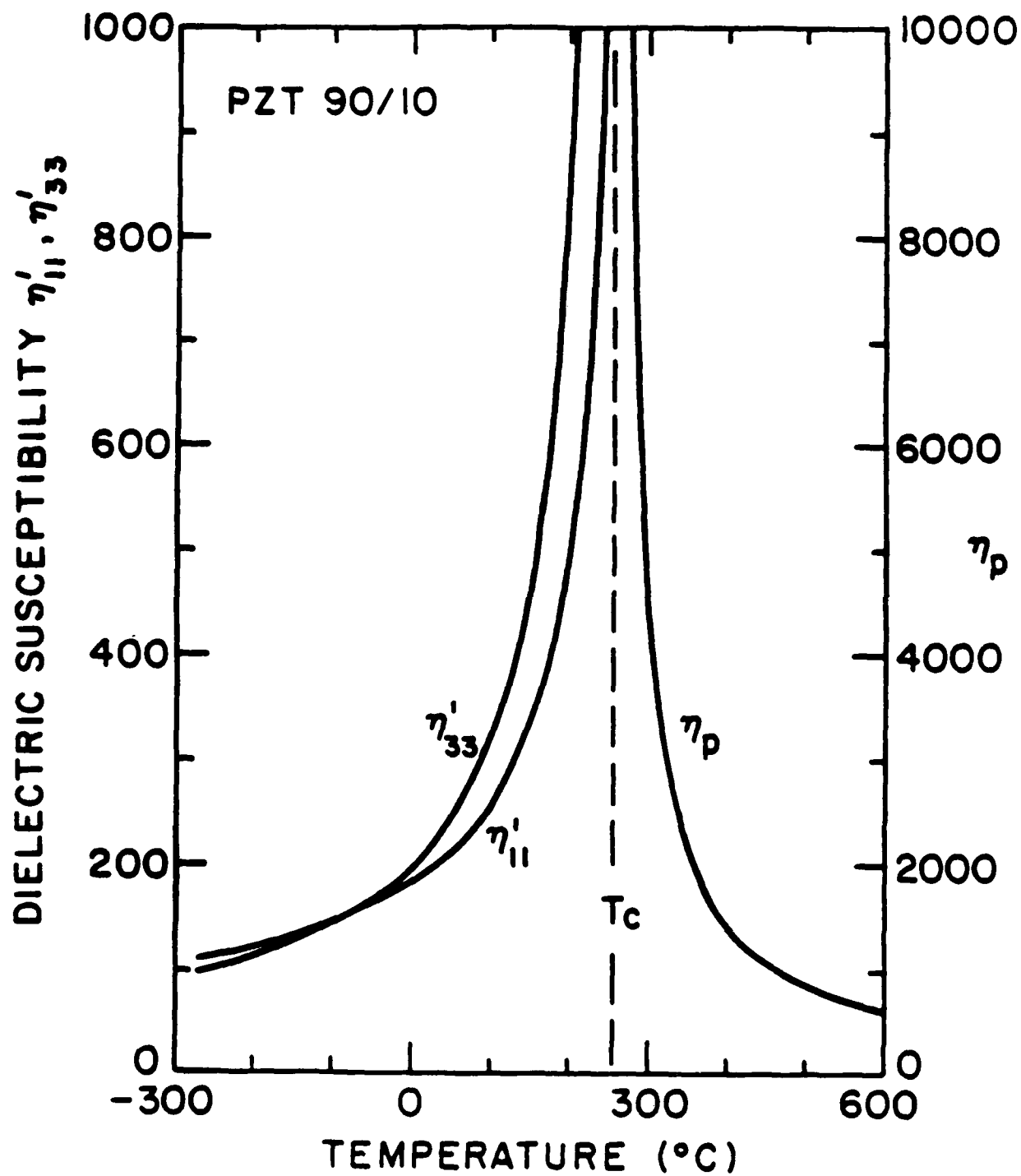
Fig. 11
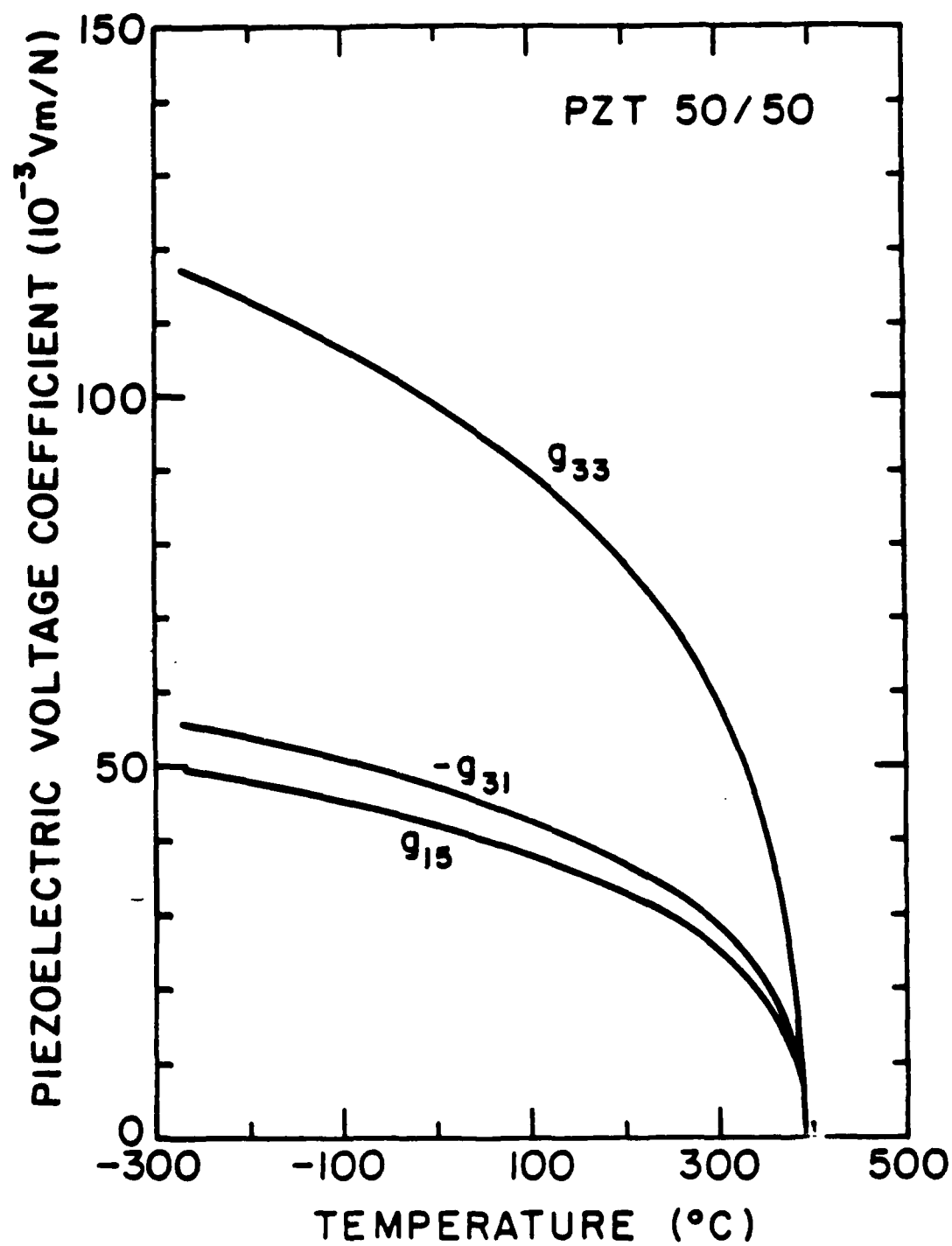
Fig. 12
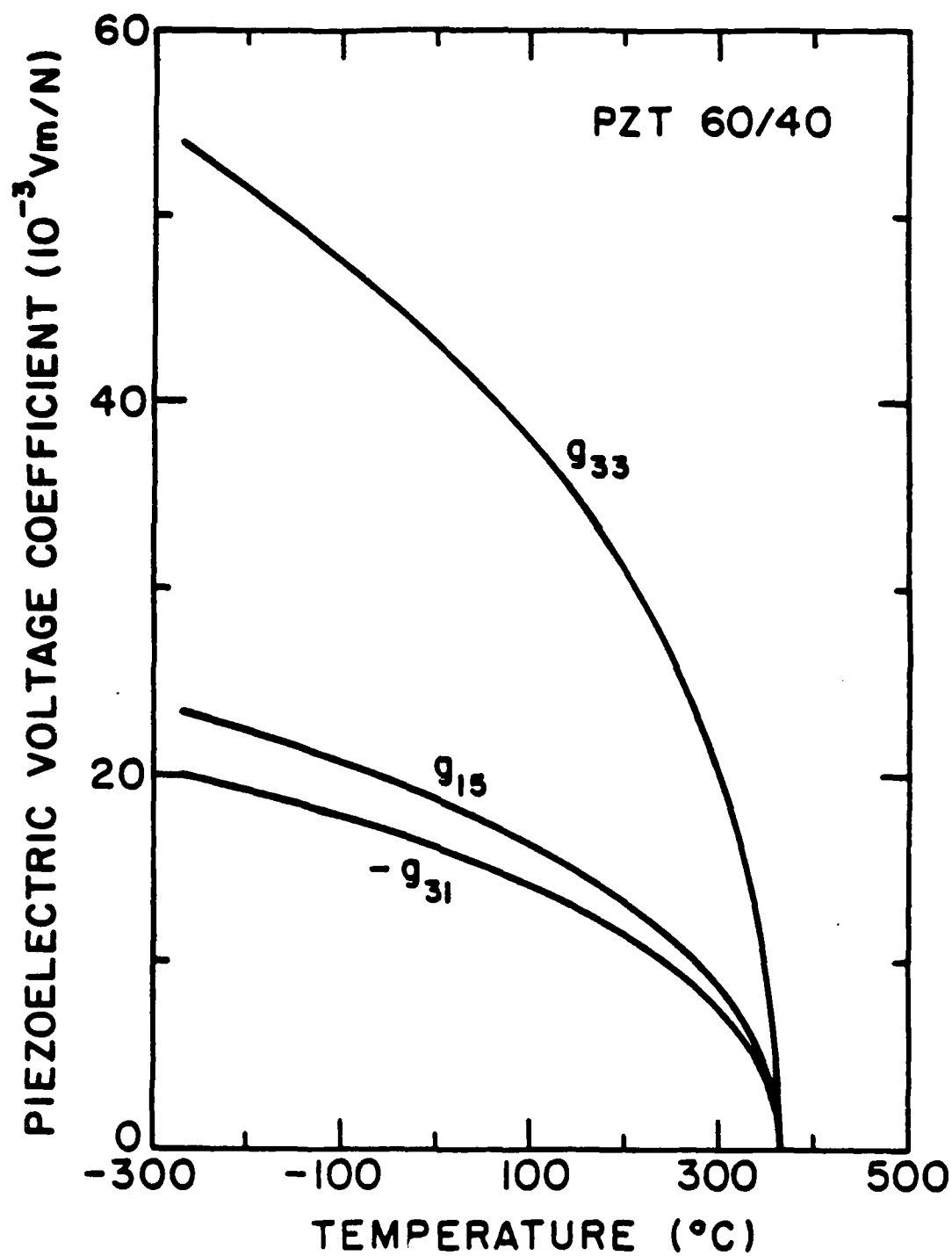
Fig. 13
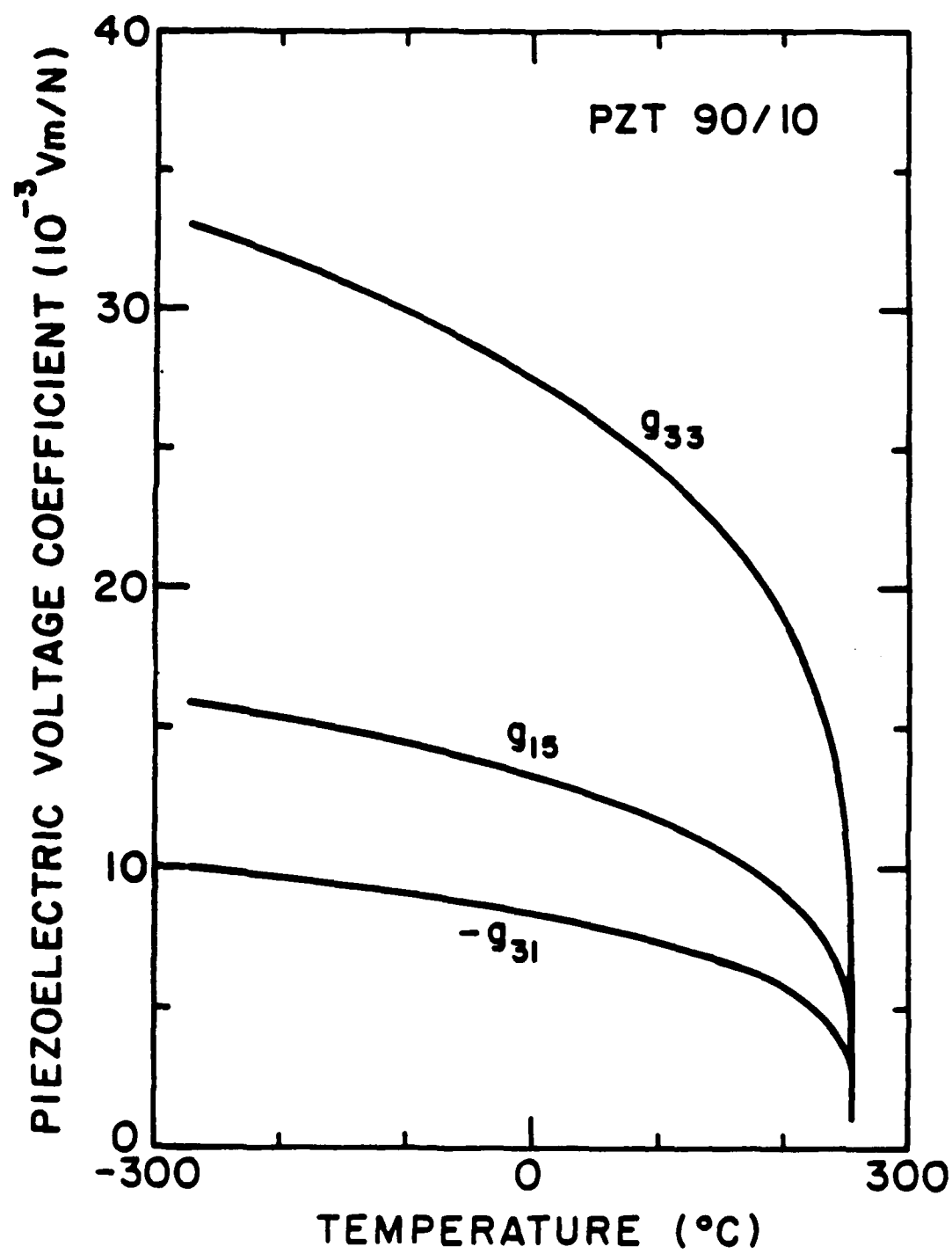
Fig. 14
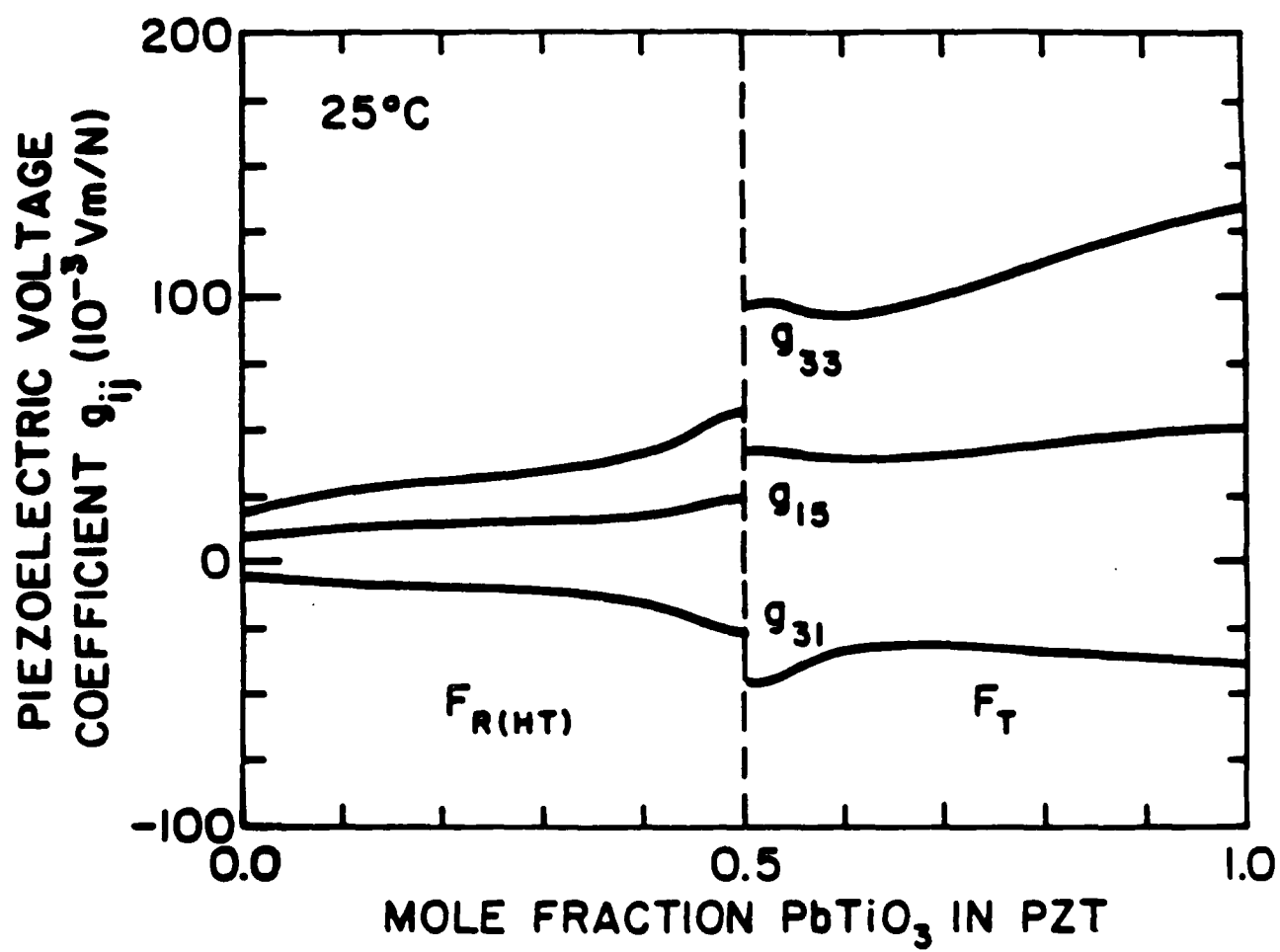
Fig. 15
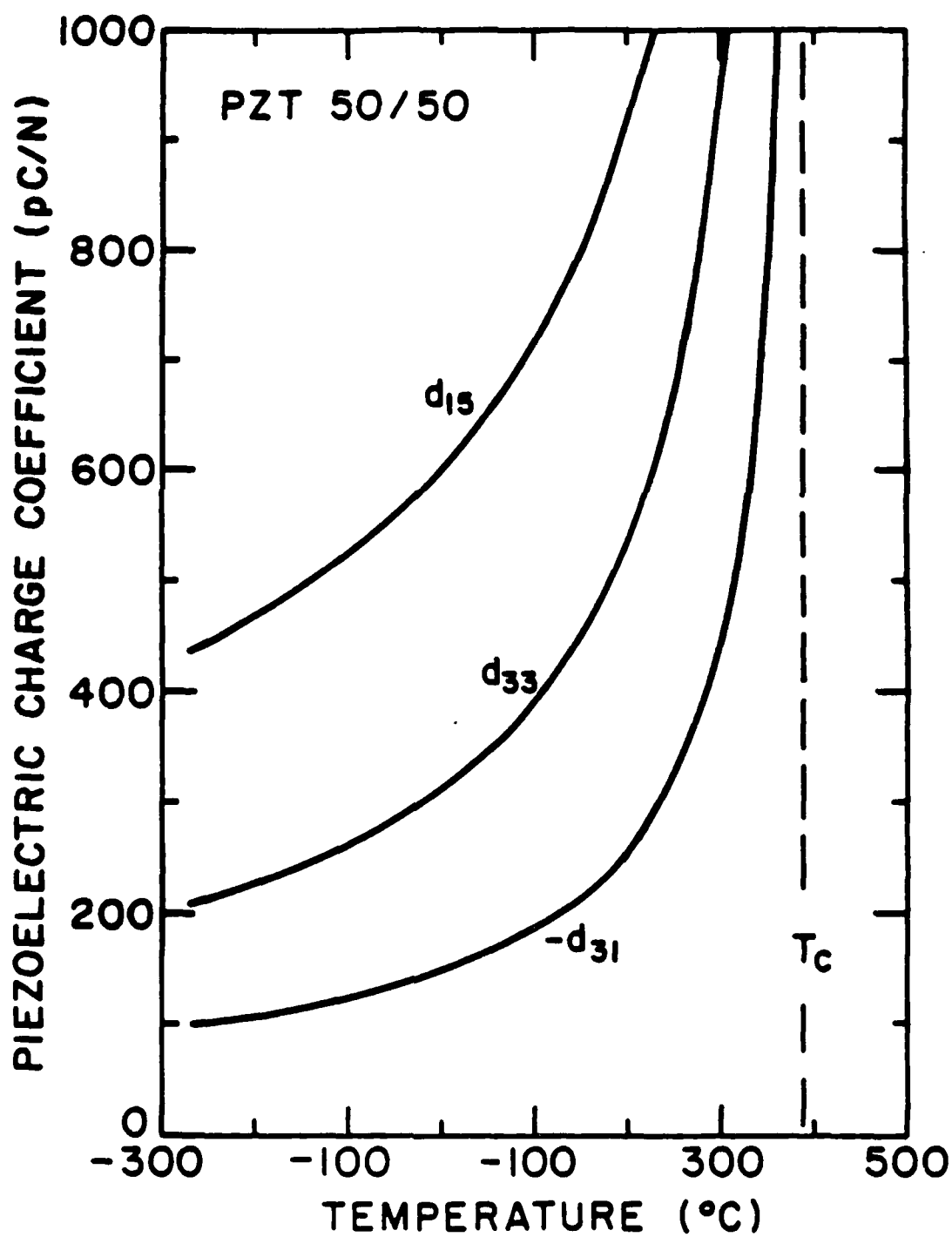
Fig. 16
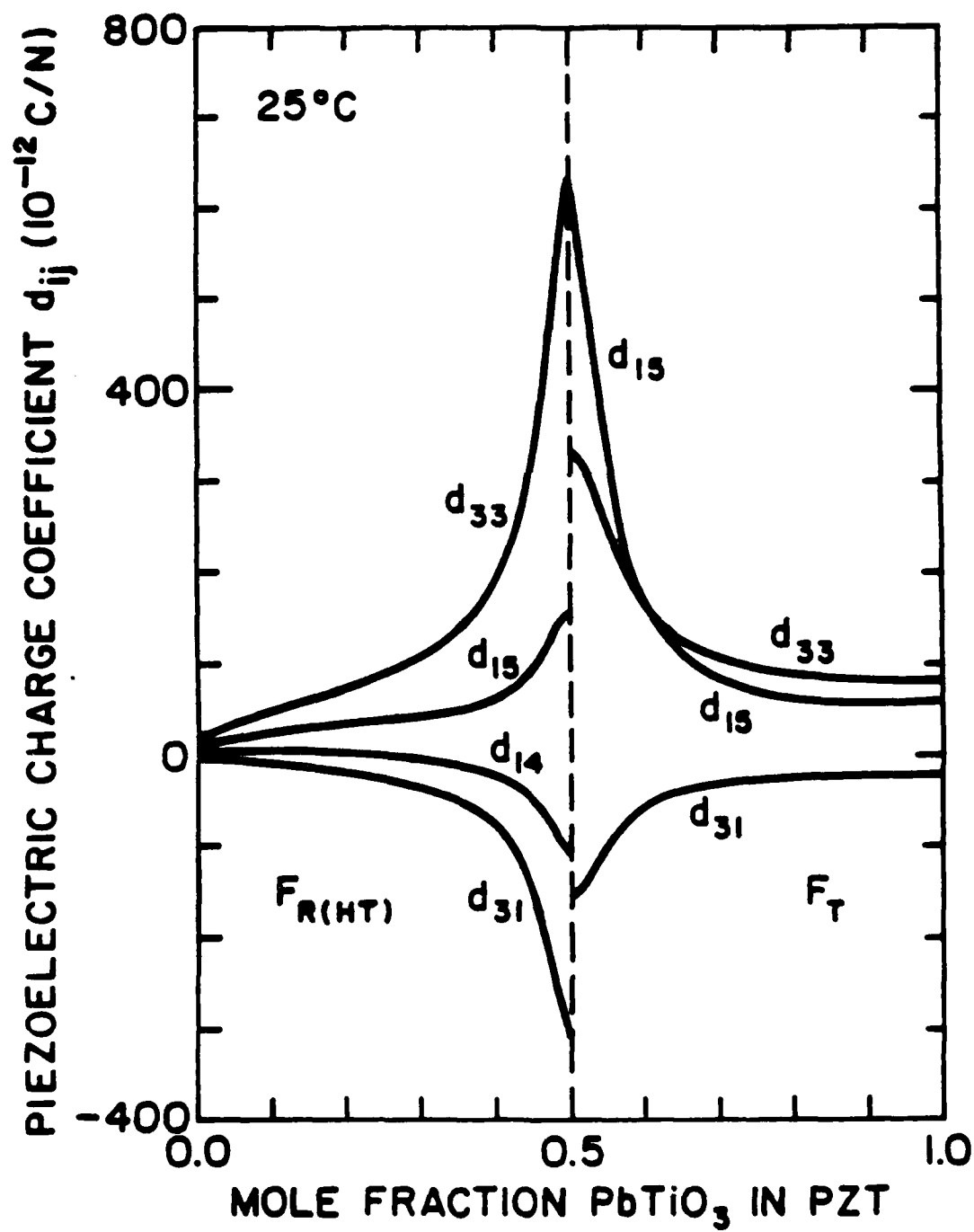
Fig. 17
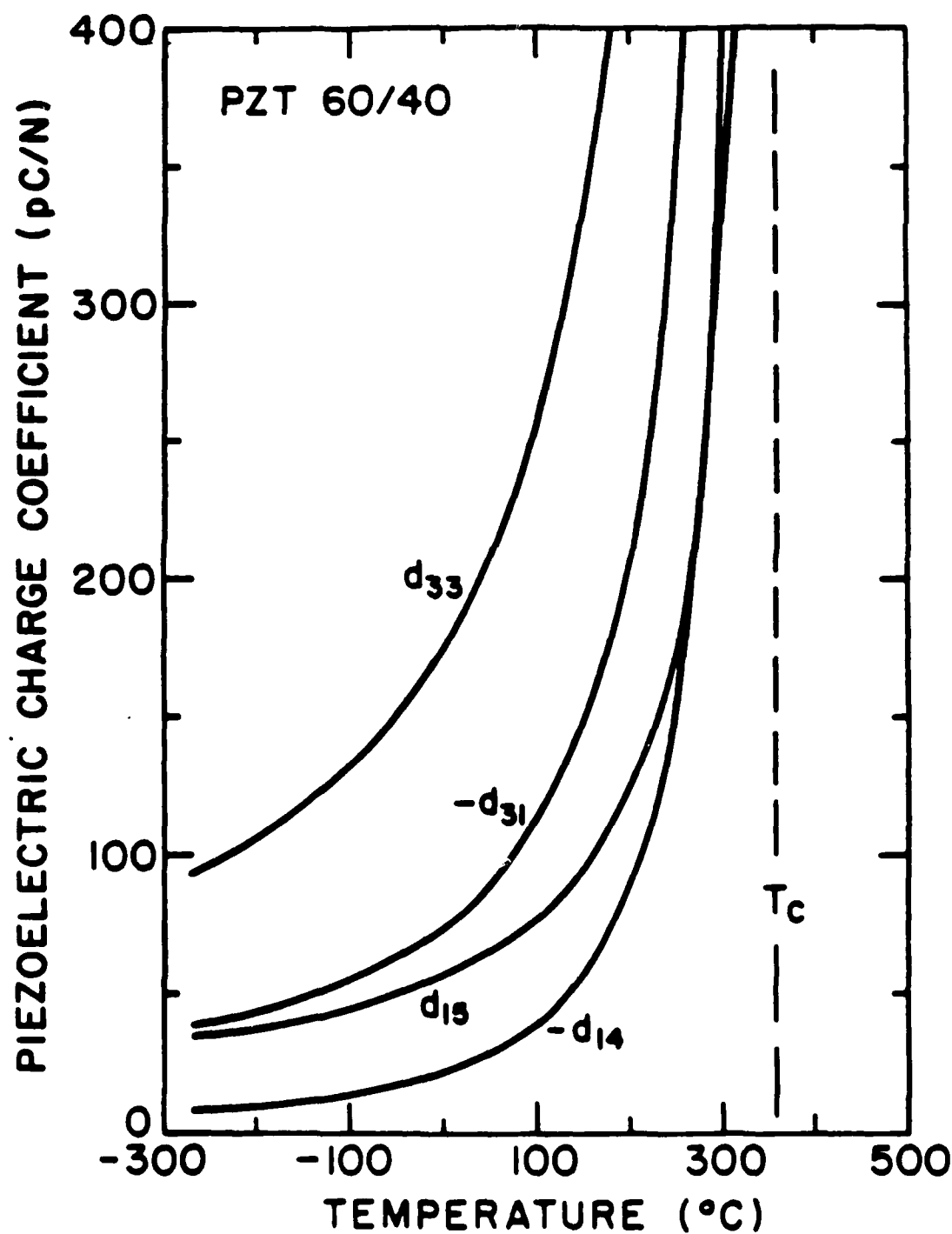
Fig. 18
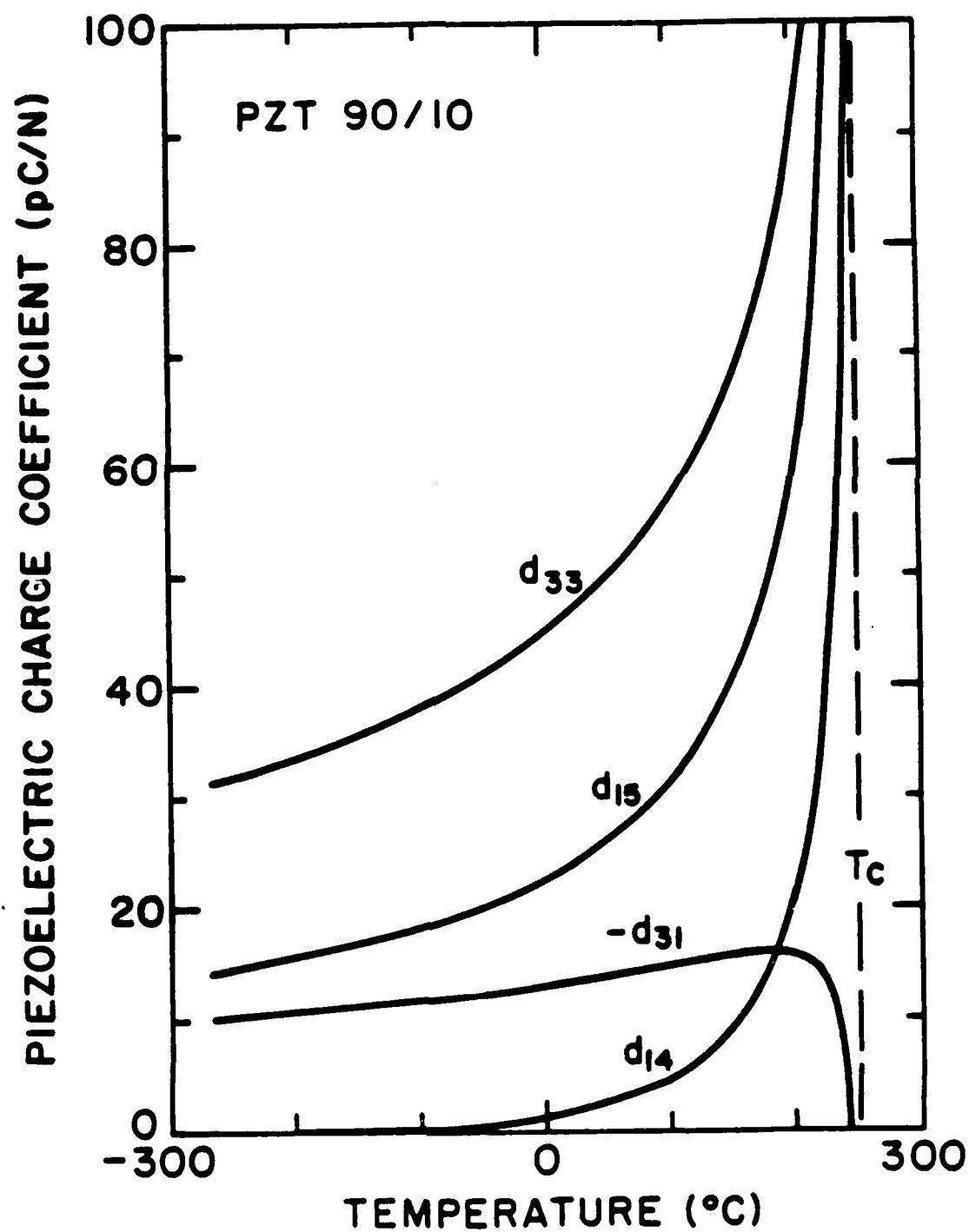
Fig. 19

THERMODYNAMIC THEORY OF PbZrO₃

M.J. Haun,[†] T.J. Harvin, M.T. Lanagan,[††]
Z.Q. Zhuang,[†††] S.J. Jang, and L.E. Cross

Materials Research Laboratory
The Pennsylvania State University
University Park, PA 16802

A thermodynamic theory is presented to model the phase transitions and properties of lead zirconate. A two-sublattice model is used to account for the antiferroelectric and ferroelectric phases.

The free energy ΔG is expressed as a power series in terms of the ferroelectric polarization ($P_i = P_{ai} + P_{bi}$) and antiferroelectric polarization ($p_i = P_{ai} - P_{bi}$) including all possible terms up to sixth power, but only first order cross coupling terms and couplings to elastic stress. Under the assumption that only the lowest order coefficients of P_i and p_i are linearly temperature dependent (Curie Weiss behavior) and all other constants are temperature independent experimental data are used to define the constants and permit calculation of ferroelectric and antiferroelectric free energies as a function of temperature.

Use of the function to define the averaged dielectric permittivity at room temperature in the antiferroelectric phase gives a value of $\epsilon_R = 120$ in good agreement with recent microwave measurements.

A simplified technique for modifying the function to explore solid solution with lead titanate is examined and shown to lead to excellent agreement with the known phase diagram.

[†]Now at DuPont Experimental Station, Electronics Dept. Bldg. 334, Wilmington, DE 19898.
[††]Now at Argonne National Lab., Materials and Components Technology Div., Argonne, IL 60439.
[†††]Visiting Scientist from the Department of Inorganic Materials Science and Engineering, South China Institute of Technology, Guangzhou, The People's Republic of China.

I. INTRODUCTION

Lead zirconate is an end member of the technologically important lead zirconate-titanate (PZT) solid solution system.[1] At room temperature $PbZrO_3$ has an antiferroelectric orthorhombic (A_O) perovskite structure with an antipolar arrangement along the [110] direction. The A_O phase remains stable up to ≈ 220 °C, where a transition occurs to a ferroelectric rhombohedral (F_R) phase with a polarization along the [111] direction.[2] The F_R phase is only stable over a narrow temperature range, and transforms to a paraelectric cubic (P_C) phase at ≈ 232 °C.[3]

Lead zirconate has been recently studied as a possible dielectric material for high frequency applications.[4,5] In this study a dielectric relaxation was found to occur at microwave frequences. To further the understanding of the dielectric properties of lead zirconate, a thermodynamic theory has been developed to calculate the intrinsic dielectric response. The development of a thermodynamic theory of lead zirconate was also needed to complete the theory that was developed for the PZT solid solution system.[6-10]

Whatmore and Glazer[11] used a one-dimensional energy function to model the Pb ion displacement in lead zirconate. Uchino et al.[12] included stress terms in the energy function to determine the hydrostatic electrostrictive coefficient. However, in these papers not enough coefficients were determined to calculate the energies and dielectric properties of the phases.

In this paper a more complete thermodynamic theory of lead zirconate will be developed using a three-dimensional energy function. In the next section the energy function will be presented, along with the solutions and property relations that can be derived from this energy function. Values of the coefficients will be determined from experimental data in Section III, and used to calculate the theoretical properties in Section IV. The calculated dielectric properties will be compared with experimental high-frequency data. In Section V a procedure will be presented to calculate the energy of the antiferroelectric orthorhombic phase into the PZT system. Finally a summary of this paper will be given in Section VI.

II. PHENOMENOLOGICAL THERMODYNAMIC THEORY

The following energy function for lead zirconate was derived from the two-sublattice theory that was previously developed to model antiferroelectric materials.[13-16] The coefficients were limited by the symmetry of the paraelectric phase (m3m). By assuming isothermal conditions, using reduced notation, and expanding the energy function in powers of the ferroelectric (P_i) and antiferroelectric (p_i) polarizations, and including couplings between these order parameters, and between the stress (X_m) and the order parameters the following energy function resulted:

$$
\begin{aligned}
\Delta G = {} & \alpha_1 \, [P_1{}^2 + P_2{}^2 + P_3{}^2] \; + \; \alpha_{11} \, [P_1{}^4 + P_2{}^4 + P_3{}^4] \\
& + \alpha_{12} \, [P_1{}^2 P_2{}^2 + P_2{}^2 P_3{}^2 + P_3{}^2 P_1{}^2] \; + \; \alpha_{111} [P_1{}^6 + P_2{}^6 + P_3{}^6] \\
& + \alpha_{112} \, [P_1{}^4 \, (P_2{}^2 + P_3{}^2) + P_2{}^4 \, (P_1{}^2 + P_3{}^2) + P_3{}^4 \, (P_1{}^2 + P_2{}^2)] \\
& + \alpha_{123} \, P_1{}^2 P_2{}^2 P_3{}^2 \; + \; \sigma_1 \, [p_1{}^2 + p_2{}^2 + p_3{}^2] \; + \; \sigma_{11} \, [p_1{}^4 + p_2{}^4 + p_3{}^4] \\
& + \sigma_{12} \, [p_1{}^2 p_2{}^2 + p_2{}^2 p_3{}^2 + p_3{}^2 p_1{}^2] \; + \; \sigma_{111} \, [p_1{}^6 + p_2{}^6 + p_3{}^6] \\
& + \sigma_{112} \, [p_1{}^4 \, (p_2{}^2 + p_3{}^2) + p_2{}^4 \, (p_1{}^2 + p_3{}^2) + p_3{}^4 \, (p_1{}^2 + p_2{}^2)] \\
& + \sigma_{123} \, p_1{}^2 p_2{}^2 p_3{}^2 \; + \; \mu_{11} \, [P_1{}^2 p_1{}^2 + P_2{}^2 p_2{}^2 + P_3{}^2 p_3{}^2] \\
& + \mu_{12} \, [P_1{}^2 \, (p_2{}^2 + p_3{}^2) + P_2{}^2 \, (p_1{}^2 + p_3{}^2) + P_3{}^2 \, (p_1{}^2 + p_2{}^2)] \\
& + \mu_{44} \, [P_1 P_2 p_1 p_2 + P_2 P_3 p_2 p_3 + P_3 P_1 p_3 p_1] \\
& - 1/2 \, S_{11} [X_1{}^2 + X_2{}^2 + X_3{}^2] - S_{12} \, [X_1 X_2 + X_2 X_3 + X_3 X_1] \\
& - 1/2 \, S_{44} \, [X_4{}^2 + X_6{}^2 + X_6{}^2] - Q_{11} \, [X_1 P_1{}^2 + X_2 P_2{}^2 + X_3 P_3{}^2] \\
& - Q_{12} \, [X_1 \, (P_2{}^2 + P_3{}^2) + X_2 \, (P_1{}^2 + P_3{}^2) + X_3 \, (P_1{}^2 + P_2{}^2)] \\
& - Q_{44} \, [X_4 \, P_2 P_3 + X_5 \, P_1 P_3 + X_6 \, P_1 P_2] - Z_{11} \, [X_1 p_1{}^2 + X_2 p_2{}^2 + X_3 p_3{}^2] \\
& - Z_{12} \, [X_1 \, (p_2{}^2 + p_3{}^2) + X_2 \, (p_1{}^2 + p_3{}^2) + X_3 \, (p_1{}^2 + p_2{}^2)] \\
& - Z_{44} \, [X_4 \, p_2 p_3 + X_5 \, p_1 p_3 + X_6 \, p_1 p_2]
\end{aligned}
\tag{1}
$$

The coefficients of this energy function are defined in Table I. The energy function includes all possible ferroelectric and antiferroelectric polarization terms up to the sixth order, and the

first-order coupling terms.

The following solutions to the energy function (Equation 1) are of interest in the lead zirconate system:

Paraelectric Cubic (P_C) $\qquad$ $P_1 = P_2 = P_3 = 0,$ $\qquad$ $p_1 = p_2 = p_3 = 0,$ $\qquad$ (2)

Ferroelectric Rhombohedral (F_R) $\qquad$ $P_1^2 = P_2^2 = P_3^2 \neq 0,$ $\quad$ $p_1 = p_2 = p_3 = 0,$ $\qquad$ (3)

Antiferroelectric Orthorhombic (A_O) $\quad$ $P_1 = P_2 = P_3 = 0,$ $\qquad$ $p_1 = 0,$ $p_2^2 = p_3^2 \neq 0$ $\quad$ (4)

Applying these solutions to Equation (1) under zero stress conditions results in the following relations for the energies of each solution:

P_C $\qquad$ $\Delta G = 0$ $\hfill$ (5)

F_R $\qquad$ $\Delta G = 3\,\alpha_1 P_3^2 + 3\,(\alpha_{11} + \alpha_{12})\,P_3^4 + (3\,\alpha_{111} + 6\,\alpha_{112} + \alpha_{123})\,P_3^6$ $\hfill$ (6)

A_O $\qquad$ $\Delta G = 2\,\sigma_1 p_3^2 + (2\,\sigma_{11} + \sigma_{12})\,p_3^4 + 2\,(\sigma_{111} + \sigma_{112})\,p_3^6$ $\hfill$ (7)

The spontaneous ferroelectric and antiferroelectric polarizations (P_3 and p_3) in the above equations can be found from the first partial derivative stability conditions ($\partial\Delta G/\partial P_3$ and $\partial\Delta G/\partial p_3$) as shown below:

F_R $\qquad$ $\partial\Delta G/\partial P_3 = 0 = (3\,\alpha_{111} + 6\,\alpha_{112} + \alpha_{123})\,P_3^4 + 2\,(\alpha_{11} + \alpha_{12})\,P_3^2 + \alpha_1$ $\quad$ (8)

A_O $\qquad$ $\partial\Delta G/\partial p_3 = 0 = 3\,(\sigma_{111} + \sigma_{112})\,p_3^4 + (2\,\sigma_{11} + \sigma_{12})\,p_3^2 + \sigma_1$ $\hfill$ (9)

The polarizations can be calculated by solving these quadratic equations. Equations (6) - (9) relate the energies of each solution to the coefficients of the energy function. Thus by determining these coefficients, the energies of each phase can be calculated.

The spontaneous elastic strains x_i $(= \partial \Delta G / \partial X_i)$ under zero stress conditions can be derived from Equation (1) as follows:

$$P_C \quad x_1 = x_2 = x_3 = x_4 = x_5 = x_6 = 0 \tag{10}$$

$$F_R \quad x_1 = x_2 = x_3 = (Q_{11} + 2Q_{12}) P_3^2, \quad x_4 = x_5 = x_6 = Q_{44} P_3^2 \tag{11}$$

$$A_O \quad x_1 = 2Z_{12} P_3^2, \quad x_2 = x_3 = (Z_{11} + Z_{12}) P_3^2, \quad x_4 = Z_{44} P_3^2, \quad x_5 = x_6 = 0 \tag{12}$$

Relations for the relative dielectric stiffnesses χ_{ij} $(= \partial^2 \Delta G / \partial P_i \partial P_j)$ were derived from Equation (1) for the solutions:

$$P_C \quad \chi_{11} = \chi_{22} = \chi_{33} = 2 \varepsilon_0 \alpha_1, \quad \chi_{12} = \chi_{23} = \chi_{31} = 0 \tag{13}$$

$$F_R \quad \chi_{11} = \chi_{22} = \chi_{33} = 2 \varepsilon_0 [\alpha_1 + (6\alpha_{11} + 2\alpha_{12}) P_3^2 + (15\alpha_{111} + 14\alpha_{112} + \alpha_{123}) P_3^4],$$
$$\chi_{12} = \chi_{23} = \chi_{31} = 4 \varepsilon_0 [\alpha_{12} P_3^2 + (4\alpha_{112} + \alpha_{123}) P_3^4] \tag{14}$$

$$A_O \quad \chi_{11} = 2\varepsilon_0 [\alpha_1 + 2\mu_{12} P_3^2], \quad \chi_{22} = \chi_{33} = 2\varepsilon_0 [\alpha_1 + (\mu_{11} + \mu_{12}) P_3^2],$$
$$\chi_{12} = \chi_{31} = 0, \quad \chi_{23} = \varepsilon_0 \mu_{44} P_3^2 \tag{15}$$

The multiplication by the permittivity of free space ε_0 in these equations was required to convert from absolute to relative dielectric stiffnesses. Equations (14) and (15) can be used to calculate the relative dielectric stiffnesses for each phase based on the original cubic axes.

In the orthorhombic state the polarization can be along any of the <110> directions of the original cubic axes. The polarization of the rhombohedral state can be along any of the <111> directions. By rotating these axes so that for both states the new x_3 axis is along the polar directions, diagonalized matrices will result. The new dielectric stiffness coefficients (indicated by a prime) can be related to the old coefficients [defined by Equations (14) and (15)] with the following relations:

$$F_R \quad \chi_{11}' = \chi_{22}' = \chi_{11} - \chi_{12}, \quad \chi_{33}' = \chi_{11} + 2\chi_{12}$$
$$\chi_{12}' = \chi_{23}' = \chi_{31}' = 0 \tag{16}$$

$$A_O \qquad \chi_{11}' = \chi_{11}, \qquad \chi_{22}' = \chi_{33} - \chi_{23}$$
$$\chi_{33}' = \chi_{33} + \chi_{23}, \qquad \chi_{12}' = \chi_{23}' = \chi_{31}' = 0 \qquad (17)$$

These equations can be used to calculate the dielectric stiffnesses of the orthorhombic and rhombohedral phases parallel and perpendicular to the polar axes.

III. EVALUATION OF THE COEFFICIENTS

In this section coefficients of the energy function will be determined from experimental data. All of the coefficients were assumed to be independent of temperature, except the ferroelectric (α_1) and antiferroelectric (σ_1) dielectric stiffness coefficients which were given a linear temperature dependence based on the Curie-Weiss law:

$$\alpha_1 = \frac{T - \theta}{2 \varepsilon_0 C} \qquad (18) \qquad \sigma_1 = \frac{T - \theta_A}{2 \varepsilon_0 C_A} \qquad (19)$$

C is the Curie constant, ε_0 is the permittivity of free space, θ is the Curie-Weiss temperature, and C_A and θ_A are antiferroelectric constants analogous to C and θ.

By combining Equations (13) and (18), C and θ can be determined from a linear fit of experimental dielectric stiffness data in the paraelectric cubic state (the Curie-Weiss law). The dielectric stiffness is the inverse of the dielectric susceptibility η_{ij}, which will be assumed to be equal to the relative dielectric permittivity ε_{ij} (actually $\varepsilon_{ij} = \eta_{ij} + 1$). Values of C and θ for lead zirconate were previously found to be equal to 1.5×10^5 °C and 190 °C by fitting the Curie-Weiss law to single-crystal dielectric data.[2,3] These constants will be used to calculate the α_1 coefficient versus temperature. A different procedure was used to determine the antiferroelectric C_A and θ_A constants as will be described later in this section.

The ferroelectric rhombohedral spontaneous polarization (P_3) can be related to the coefficients of the energy function by solving the quadratic relation formed from the first

partial derivative stability condition [Equation (8)]:

$$P_3^2 = \frac{-\zeta + [\zeta^2 - 9\,\alpha_1\,\xi]^{1/2}}{3\,\xi} \, , \tag{20}$$

where $\zeta = 3\,(\alpha_{11} + \alpha_{12})$, and $\xi = 3\,\alpha_{111} + 6\,\alpha_{112} + \alpha_{123}$ (21)

At T_C, the transition temperature between the ferroelectric rhombohedral and paraelectric cubic phases, two relations must be satisfied:

$$0 = 3\,\alpha_{1C} + \zeta\,P_{3C}^2 + \xi\,P_{3C}^4 \, , \text{ and} \tag{22}$$
$$0 = \alpha_{1C} + 2/3\,\zeta\,P_{3C}^2 + \xi\,P_{3C}^4 \, , \tag{23}$$

where α_{1C} and P_{3C} are α_1 and P_3 at T_C. Equation (22) was derived from the requirement that the ΔG's of the cubic and rhombohedral phases [Equations (5) and (6)] must be equal at T_C. Equation (23) is the first partial derivative stability condition [Equation (8)], which must be satisfied so that the stable state corresponds to the minima of the energy function.

When the transition at T_C is first order the spontaneous polarization in the ferroelectric state will develop discontinuously at the transition, and thus P_{3C} will be nonzero. In this case Equation (18) can be substituted into Equations (22) and (23) to obtain relations for the ζ and ξ coefficients:

$$\zeta = \frac{-3\,(T_C - \theta)}{\varepsilon_0\,C\,P_{3C}^2} \, , \qquad\qquad \xi = \frac{3\,(T_C - \theta)}{2\,\varepsilon_0\,C\,P_{3C}^4} \tag{24}$$

By assuming that the ζ and ξ coefficients are independent of temperature, and then substituting Equations (24) and (18) into Equation (20), the following relation results for the spontaneous polarization of the ferroelectric rhombohedral phase:

$$P_3^2 = \psi\,P_{3C}^2 \, , \qquad \text{where} \quad \psi = \frac{2}{3}\left\{ 1 + \left[1 - \frac{3\,(T - \theta)}{4\,(T_C - \theta)} \right]^{1/2} \right\} \tag{25}$$

Now if P_{3C}, T_C, and θ can be determined, the spontaneous polarization of the ferroelectric

rhombohedral phase can be calculated versus temperature. Note that P_3 is the x_3 component of the resultant spontaneous polarization (P_S) along the [111] direction, and thus

$$P_S = 3^{1/2} P_3.$$

Using the value of θ given above, with T_C equal to 232 °C,[3] a value of P_{3C} was found from the best least-squares fit of Equation (25) to experimental spontaneous polarization data (from Curve 2 in Figure 3 of Reference 17), as shown in the insert of Figure 1. The resulting P_{3C} value is listed in Table II with the values of the other constants that were used in the calculations. These values were used to calculate the ferroelectric rhombohedral spontaneous polarization versus temperature down to - 273 °C as shown in Figure 1. However, over most of this temperature region the rhombohedral phase is metastable to the stable antiferroelectric orthorhombic phase.

A similar relation to Equation (25) can be derived for the spontaneous strain x_4 by substituting Equation (25) into Equation (11):

$$x_4 = \psi\, x_{4C}, \qquad \text{where} \quad x_{4C} = Q_{44}\, P_{3C}^{2} \tag{26}$$

This equation was used with the values of the constants listed in Table II to determine a value of x_{4C} (x_4 at T_C) that gave the best least-squares fit of experimental x_4 data, as shown in the insert of Figure 2. The experimental x_4 data was calculated from rhombohedral angle α_R data from Reference 11 using the relation: $x_4 = (90 - \alpha_R)/90$. A value of the electrostrictive Q_{44} constant was calculated from x_{4C} and P_{3C} using Equation (26). This value is listed in Table II. The ferroelectric rhombohedral spontaneous strain x_4 was calculated versus temperature into the antiferroelectric region as shown in Figure 2 using Equation (26) and the constants listed in Table II.

The constants determined above will be used to calculate the ΔG of the ferroelectric rhombohedral phase in the next section. The procedure used to determine values of the antiferroelectric constants, which are needed to calculate the ΔG of the antiferroelectric orthorhombic phase, will now be presented.

The antiferroelectric measure of the polarization p_3 for the orthorhombic solution can be related to the antiferroelectric σ coefficients by solving the quadratic relation formed from the first partial derivative stability condition [Equation (9)]:

$$p_3{}^2 = \frac{-\delta + [\delta^2 - 6\,\sigma_1\,\gamma]^{1/2}}{3\,\gamma} \tag{27}$$

$$\text{where} \quad \delta = 2\,\sigma_{11} + \sigma_{12}, \qquad \text{and} \quad \gamma = 2\,(\sigma_{111} + \sigma_{112}) \tag{28}$$

The Neel temperature (T_N) is the transition temperature from an antiferroelectric phase to a paraelectric phase. In lead zirconate this is a metastable phase transition, because it occurs in the ferroelectric rhombohedral stability region. As in the rhombohedral case at T_C, two equations must be satisfied at T_N:

$$0 = 2\,\sigma_{1N} + \delta\,p_{3N}{}^2 + \gamma\,p_{3N}{}^4 \tag{29}$$

$$0 = \sigma_{1N} + \delta\,p_{3N}{}^2 + 3/2\,\gamma\,p_{3N}{}^4 \tag{30}$$

σ_{1N} and p_{3N} are σ_1 and p_3 at T_N. Equation (29) was derived from the requirement that the ΔG's of the two phases [Equations (5) and (7)] must be equal at T_N. Equation (30) is the first partial derivative stability condition [Equation (9)].

Substituting Equation (19) into Equations (29) and (30), and solving for the δ and γ coefficients results in:

$$\delta \approx \frac{-2\,(T_N - \theta_A)}{\varepsilon_0\,C_A\,p_{3N}{}^2}, \qquad\qquad \gamma = \frac{T_N - \theta_A}{\varepsilon_0\,C_A\,p_{3N}{}^4} \tag{31}$$

where p_{3N} is p_3 at T_N.

By assuming that the δ and γ coefficients are independent of temperature, and then substituting Equations (19) and (31) into Equation (27) yields:

$$p_3{}^2 = \psi\, p_{3N}{}^2 , \qquad \text{where} \quad \psi = \frac{2}{3}\left\{\, 1 + \left[\, 1 - \frac{3\,(T - \theta_A)}{4\,(T_N - \theta_A)} \right]^{1/2} \right\} \qquad (32)$$

Unfortunately, there is not any experimental antiferroelectric polarization p_3 data available, and thus p_{3N} will not be determined in this paper.

However, antiferroelectric spontaneous strain data can be calculated from cell constant data, and used to determine two of the antiferroelectric constants. By substituting Equation (32) into Equation (12) the following relation results for the antiferroelectric spontaneous strain x_4:

$$x_4 = \psi\, x_{4N} , \qquad \text{where} \quad x_{4N} = Z_{44}\, p_{3N}{}^2 \qquad (33)$$

x_{4N} is x_4 at T_N. Values of T_N, θ_A, and x_{4N} are needed to calculate x_4 using Equations (32) and (33).

Spontaneous strain x_4 data was calculated from cell constant data from Reference 11 [interaxial γ_p data from Figure 5 in Reference 11 was related to x_4 with the relation: $x_4 = (90 - \gamma_p)/90$]. By fitting this data with all three constants (T_N, θ_A, and x_{4N}) as unknowns many combinations of the values of these constants gave similar fits of the data. For this reason the value of one of these constants had to be determined from additional data. Without additional data, it was necessary to make an assumption.

T_N must occur between the antiferroelectric-ferroelectric transition temperature (T_{AF}) and the ferroelectric-paraelectric transition temperature (T_C). T_{AF} occurs at $\approx 220\ ^\circ\mathrm{C}$ (average of the heating and cooling DTA data in Reference 2), and T_C at $\approx 232\ ^\circ\mathrm{C}$. Thus since T_N must occur between 220 and 232 $^\circ\mathrm{C}$, it was assumed to be equal to 226$^\circ\mathrm{C}$, the average of the two extremes. This was a good assumption, because the constants were not significantly affected even if T_N was varied a few degrees. With T_N fixed at 226 $^\circ\mathrm{C}$ values

of θ_A and x_{4N} were found that gave the best least-squares fit of the x_4 data as shown in Figure 3. These values are listed in Table II.

Substituting Equations (19), (28), (31), (32) and (33) into Equation (7) results in the following relation for the ΔG of the antiferroelectric orthorhombic phase:

$$\Delta G = \psi \, x_{4N}/(\varepsilon_0 \, Z_{44} \, C_A) \, [T - T_A - 2 \, \psi \, (T_N - T_A) \, (1 - 1/2 \, \psi)] \qquad (34)$$

All of the constants needed to calculate the ΔG of the antiferroelectric orthorhombic phase using this equation have been determined, except for the Z_{44} and C_A constants. At this point there is not enough experimental data available to determine values of both of these constants. However, the product of these constants can be determined by equating the ΔG's of the A_O and F_R phases at the transition between these phases:

$$\text{At } T_{AF}: \qquad \Delta G_{F_R} = \Delta G_{A_O} \qquad (35)$$

The rhombohedral ΔG at T_{AF} can be calculated from Equations (6), (19), (21), (24), and (25) using the constants listed in Table II. This value can then be used with Equations (34) and (35) and the constants from Table II to calculate a value of the $Z_{44} \, C_A$ product. This value is listed in Table II. By assuming that $Z_{44} \, C_A$ is independent of temperature, all of the constants necessary to calculate the ΔG of the antiferroelectric orthorhombic phase versus temperature have been determined. Calculations of the ΔG's of the ferroelectric and antiferroelectric phases will be presented in the next section.

All of the α coefficients must be determined to calculate the dielectric stiffness χ_{ij} coefficients of the ferroelectric rhombohedral phase [see Equation (14)]. The constants determined earlier in this section can be used in Equation (24) to calculate the ζ [$= 3 \, (\alpha_{11} + \alpha_{12})$] and ξ [$= 3 \, \alpha_{111} + 6 \, \alpha_{112} + \alpha_{123}$] coefficients, which can be used to calculate the spontaneous polarization, strain, and ΔG of the F_R phase. At this time there are not enough lead zirconate data present to determine values of α_{11}, α_{12}, α_{111}, α_{112}, and α_{123}. However, these coefficients were determined in the PZT system, and extrapolated to

lead zirconate.[6-10]

To calculate the dielectric stiffness χ_{ij} coefficients of the antiferroelectric orthorhombic phase. the μ_{ij} antiferroelectric-ferroelectric coupling coefficients must be determined. Unfortunately the data necessary to determine these coefficients has not been measured. One goal of this project was to compare calculations from this theory with polycrystalline high-frequency dielectric data. To accomplish this a procedure was used to combine the unknown constants in the dielectric relations into one constant that could be determined from low-temperature polycrystalline dielectric data. This procedure will be described below.

By combining Equations (15) and (17) dielectric stiffness relations based on the normal orthorhombic axes result:

$$\chi_{11}' = 2\,\varepsilon_0\,[\alpha_1 + 2\,\mu_{12}\,p_3{}^2]\,,$$
$$\chi_{22}' = 2\,\varepsilon_0\,[\alpha_1 + (\mu_{11} + \mu_{12} - 1/2\,\mu_{44})\,p_3{}^2]\,,$$
$$\chi_{33}' = 2\,\varepsilon_0\,[\alpha_1 + (\mu_{11} + \mu_{12} + 1/2\,\mu_{44})\,p_3{}^2] \tag{36}$$

These single-crystal coefficients were related to the polycrystalline dielectric stiffness χ (a bold-faced italic symbol will be used to refer to polycrystalline constants) using the following parallel averaging relation:

$$\chi = 1/3\,(\chi_{11}' + \chi_{22}' + \chi_{33}') \tag{37}$$

By substituting Equation (36) into Equation (37) the following relation results:

$$\chi = 2\,\varepsilon_0\,[\alpha_1 + 2/3\,(\mu_{11} + 2\,\mu_{12})\,p_3{}^2] \tag{38}$$

Not enough experimental data was available to determine the constants necessary to calculate p_3. However, the constants needed calculate the antiferroelectric spontaneous strain x_4 were

determined. By substituting Equation (12) into Equation (38) p_3 can be replaced by x_4:

$$1/\varepsilon \approx \chi = 2\,\varepsilon_0\,(\alpha_1 + \lambda\,x_4)\,, \quad \text{where} \quad \lambda = \frac{2\,(\mu_{11} + 2\,\mu_{12})}{3\,Z_{44}} \tag{39}$$

Since α_1 and x_4 can be determined from Equations (18) and (33) using the constants listed in Table II, the new constant λ can be calculated from an experimental polycrystalline dielectric constant (ε) measurement ($\varepsilon \approx 1/\chi$).

To provide experimental data to evaluate the λ constant the dielectric constant was measured at 1KHz from - 268.8 °C to room temperature on polycrystalline lead zirconate. The procedure used to fabricate the lead zirconate samples was described in References 4 and 5. The low-temperature measurement apparatus and technique that was used was described in Reference 18. At low-temperatures (- 268.8 °C) the extrinsic contributions to the polycrystalline dielectric properties, such as domain wall motion or thermally activated defect motions, were assumed to "freeze out". The remaining dielectric properties would then represent the intrinsic contribution, or averaging of the single-domain properties.

A dielectric constant of 95 was measured at - 268.8 °C, and used to calculate the value of the λ constant listed in Table II. By assuming that this constant is independent of temperature the intrinsic polycrystalline dielectric constant could be calculated versus temperature using Equation (39) and the constants listed in Table II. These calculations will be compared with experimental high-frequency dielectric measurements in the next section.

IV. THEORETICAL CALCULATIONS

In this section theoretical calculations will be made using the equations from Section II, and the constants that were determined in the Section III. Figure 4 shows the energies ΔG of the antiferroelectric orthorhombic and ferroelectric high-temperature rhombohedral phases plotted versus temperature for lead zirconate. Above T_C (232 °C) the energy of the ferroelectric rhombohedral phase is positive, and thus the cubic state with the reference

energy set to zero is stable. At T_C the energy of the F_R phase decreases to zero, and then becomes negative below T_C causing the tetragonal phase to become stable. At T_N the energy of the antiferroelectric orthorhombic phase is zero, and a metastable transition occurs with the cubic phase. As the temperature decreases the the larger temperature dependence of the ΔG of the A_O phase compared to the F_R phase causes the energies of these phases to become equal at the transition T_{AF}. Below T_{AF} the A_O phase becomes stable, and remains stable down to - 273 °C.

The polycrystalline dielectric constant (ε) of the antiferroelectric orthorhombic phase was calculated from Equation (39) using the constants listed in Table II, and plotted in Figure 5 versus temperature up to T_{AF}. The dielectric constant of the paraelectric cubic phase was also calculated using Equation (13), and plotted in this figure above T_C. The ferroelectric rhombohedral dielectric properties were not investigated in this paper, but could be calculated from the values of the coefficients that were recently determined in References 6 - 10.

The experimental data, that was measured at 1KHz from - 268.8 °C to room temperature, is plotted in the insert in Figure 5. The data point at - 268.8 °C was used to calculate the λ constant, as described in Section III. By assuming that the theory is predicting the intrinsic response of the material, the difference that develops between the theoretical calculations and experimental data as the temperature is increased is due to the thermally activated (extrinsic) contributions to the polycrystalline dielectric constant. At room temperature the theoretical dielectric constant has a value of 120, compared to the experimental value of 167. This indicates that 72% of the experimentally measured polycrystalline dielectric constant is due to the intrinsic averaging of the single-domain constants, while 28% is from extrinsic contributions.

Lanagan et al.[4,5] measured the dielectric constant of polycrystalline lead zirconate from 100 Hz to 26 GHz. Their data are plotted versus the log of the frequency in Figure 6. As can be seen by these data a relaxation occurred at microwave frequences. Above this relaxation the dielectric constant agrees remarkably well with the calculation from the theory

presented in this paper, indicating that the extrinsic contributions to the dielectric properties have "relaxed out" above ≈ 10 GHz.

The data in Figures 5 and 6 indicate that the extrinsic contributions to the polycrystalline dielectric constant of lead zirconate will "freeze out" at low temperatures and "relax out" at high frequences, and that the remaining intrinsic contributions can be thermodynamically modeled. The theory provides a method of connecting the low-temperature data to the high-frequency data. It would now be useful to measure the high-frequency dielectric properties down to low temperatures.

The dielectric constant at 10 GHz was measured as a function of temperature as shown in Figure 7. The 1 KHz data from Figure 5 is also plotted in this figure along with the theoretical calculations. Unfortunately at this time the 10 GHz data was only measured down to -100 °C, and thus it is still not clear how the data would compare at lower temperatures. There is a slight difference between the temperature dependences of the 10 GHz data and the theoretical calculations. This may indicate that at 10 GHz all of the extrinsic contributions had not completely "relaxed out", or that the actual temperature dependence was not completely accounted for in the theory (most of the coefficients of the energy function were assumed to be independent of temperature). In addition there is some experimental error in the measurements. The calibration for these measurements was only made at room temperature, and thus an error of ± 10% has been estimated for the 10 GHz data.

V. EXTENSION OF THE THEORY INTO THE PZT SYSTEM

In this section a procedure will be presented that can be used to calculate the compositional dependence of the ΔG of the antiferroelectric orthorhombic phase into the PZT system. This procedure was needed to complete the development of a thermodynamic theory to model all of the phase transitions of the PZT system.[6-10]

The ΔG of the antiferroelectric orthorhombic phase for lead zirconate was calculated in Section IV using Equation (34). The constants needed for these calculations were determined from the available experimental data, as described in Section III. Unfortunately, similar experimental data is not available for PZT compositions in the antiferroelectric region, and thus the compositional dependence of each of the constants necessary to calculate the ΔG of the A_O phase could not be determined. However, the following method was used to calculate the ΔG of the A_O phase into the PZT system from the compositional dependence of a single constant, which was determined by equating the ΔG's of the A_O and F_R phases at the transition between these phases.

The ΔG of the antiferroelectric orthorhombic phase was determined from the following relation by multiplying the ΔG of lead zirconate (PZ) by a factor Ξ:

$$\Delta G_{A_O} = \Xi \, \Delta G_{A_O}(PZ) \tag{40}$$

The compositional dependence of Ξ was then determined by combining this relation with Equation (35):

$$\Xi = \Delta G_{F_R}(At \, T_{AF}) / \Delta G_{A_O}(PZ) \tag{41}$$

To calculate Ξ using this equation, ΔG of the F_R phase (high-temperature rhombohedral phase in PZT) at T_{AF} was calculated from the PZT theory developed in References 6-10. The antiferroelectric-ferroelectric transition temperature T_{AF} was determined by fitting the following polynomial equation to the experimental phase diagram:[1]

$$T_{AF} = 220.84 - 706.15 \, x - 26778. \, x^2 \tag{42}$$

where x is the mole fraction $PbTiO_3$ in PZT.

ΔG of the A_O phase for lead zirconate was calculated from the equations and data presented in this paper, except that the value of the Curie constant was changed. The

compositional dependence of the Curie constant that was used in the PZT theory[8] resulted in a value of 2.0×10^5 °C, instead of the value of 1.5×10^5 °C that was used in the previous calculations in this paper. To be consistent with the PZT calculations the value of the Curie constant was changed, which also caused the value of the $Q_{44} C_A$ constant to change to 889.27 m^4 °C/C^2, instead of the value listed in Table II.

Using the calculations described above in Equation (41), the Ξ constant was calculated versus composition, as plotted in Figure 8. By then assuming the Ξ constant to be independent of temperature, the ΔG of the antiferroelectric phase was calculated versus composition into the PZT system, as shown in Reference 10. This method resulted in excellent agreement between the experimental and theoretical phase diagrams.[10]

IV. SUMMARY

A two-sublattice theory was used to derive an energy function to account for the ferroelectric and antiferroelectric behavior of lead zirconate. Solutions and property relations were derived from this energy function corresponding to the stable solid phases of lead zirconate. The coefficients necessary to calculate the ferroelectric rhombohedral ΔG, and spontaneous polarization and strain; and antiferroelectric ΔG and spontaneous strain were determined from the available experimental data in the literature.

Additional data were needed to model the intrinsic polycrystalline dielectric properties of lead zirconate. To provide these data the dielectric properties were measured down to low temperatures (- 268.8 °C), where extrinsic contributions to the properties "freeze out". These data were then used to determine the value of a combination of constants, which could be used to calculate the intrinsic polycrystalline dielectric constant versus temperature. The calculations indicate that at room temperature 72% of the experimentally measured polycrystalline dielectric constant (measured at 1 KHz) is due to the intrinsic averaging of the single-domain constants, while 28% is from extrinsic

contributions. The calculations were found to be in good agreement with experimental data at high-frequencies (> 10 GHz), indicating that the extrinsic contributions had "relaxed out".

A simple method was presented to calculate the ΔG of the antiferroelectric orthorhombic phase into the PZT system. This method was used to complete the development of a thermodynamic theory, which quantitatively accounts for all of the known phase transitions in the PZT system. [6-10]

Additional data is still needed to determine values of the coefficients of the energy function that were not determined in this paper. The effects of the application of electric field[19] or mechanical stress[20] may provide some of this data.

REFERENCES

[1] B. Jaffe, W. J. Cook, and H. Jaffe, *Piezoelectric Ceramics* (Academic, London, 1971).

[2] Z. Ujma and J. Handerek, Phys. Stat. Sol. (a) **28**, 489 (1975).

[3] B. A. Scott and G. Burns, J. Am. Ceram. Soc. **55**, 331 (1972).

[4] M. T. Lanagan, *Microwave Dielectric Properties of Antiferroelectric Lead Zirconate*, Ph.D. Thesis in Ceramic Science, The Pennsylvania State University (1987).

[5] M. T. Lanagan, J. H. Kim, S. J. Jang, and R. E. Newnham, Am. Ceram. Soc. (to be published).

[6] M. J. Haun, E. Furman, S. J. Jang, and L. E. Cross, "Thermodynamic Theory of the Lead Zirconate-Titanate Solid Solution System, Part I: Phenomenology," J. Appl. Phys. (submitted).

[7] M. J. Haun, E. Furman, H. A. McKinstry, and L. E. Cross, "Thermodynamic Theory of the Lead Zirconate-Titanate Solid Solution System, Part II: Tricritical Behavior," J. Appl. Phys. (submitted).

[8] M. J. Haun, Z. Q. Zhuang, E. Furman, S. J. Jang, and L. E. Cross, "Thermodynamic Theory of the Lead Zirconate-Titanate Solid Solution System, Part III: Curie Constant and Sixth-order Polarization Interaction Dielectric Stiffness Coefficients," J. Appl. Phys. (submitted).

[9] M. J. Haun, E. Furman, T. R. Halemane, and L. E. Cross, "Thermodynamic Theory of the Lead Zirconate-Titanate Solid Solution System, Part IV: Tilting of the Oxygen Octahedra," J. Appl. Phys. (submitted).

[10] M. J. Haun, E. Furman, S. J. Jang, and L. E. Cross, "Thermodynamic Theory of the Lead Zirconate-Titanate Solid Solution System, Part V: Theoretical Calculations," J. Appl. Phys. (submitted).

[11] R. W. Whatmore and A. M. Glazer, J. Phys. C: Solid State Phys. **12**, 1505 (1979).

[12] K. Uchino, L. E. Cross, R. E. Newnham, and S. Nomura, J. Appl. Phys. **52**, 1455 (1981).

[13] C. Kittel, Phys. Rev. **82**, 729 (1951).

[14] A. F. Devonshire, Phil. Mag. **3**, 85 (1954).

[15] L. E. Cross, Phil. Mag. **1**, 76 (1956).

[16] C. N. W. Darlington, J. Appl. Phys. **43**, 4951 (1972).

[17] Z. Ujma and J. Handerek, Acta Physica Polonica **A53**, 665 (1978).

[18] Z. Q. Zhuang, M. J. Haun, S. J. Jang, and L. E. Cross, *Proceedings of the 6th IEEE International Symposium on the Applications of Ferroelectrics*, Lehigh, PA, edited by Van Wood (IEEE, New York, 1986) pp. 394-397.

[19] O. E. Fesenko, V. G. Smotrakov, and N. G. Leontiev, Ferroelectrics Letters **2**, 33 (1984).

[20] G. A. Samara, Phys. Rev. B **1**, 3777 (1970).

END

DATE

FILMED

9-88

DTIC